Investigating the pathophysiological mechanisms linked to 2 membrane proteins: the choline transporter 1 and the kidney anion exchanger 1

by

Midhat Ali Rizvi

A thesis submitted in partial fulfillment of the requirements for the degree of

Master of Science

Department of Physiology
University of Alberta

Abstract

Many diseases are caused by inherited mutations. Using molecular genetics and other laboratory techniques, they can be studied *in vitro* and *in vivo*. Congenital myasthenic syndromes is one example, for which I created an *in-vitro* model of the heterozygous mutations in the choline transporter (CHT1), I294T and D349N, that result in a severe form of the disease in a patient. Congenital myasthenic syndrome is rare neuromuscular disorder and the phenotypes range from muscle weaknesses to lethality, therefore it is necessary to study them to understand this heterogeneity. I generated the two mutations via site-directed mutagenesis, introduced them into human embryonic kidney cells via lentiviral transfection and characterized each mutant. I hypothesized that the CHT1 mutations found in the patient cause a partial loss of choline transport. We found that CHT1-I294T is less abundant than WT-CHT1, has appropriate localization, a shorter half-life, and some residual activity at low concentration of choline. Because there was residual activity, we incubated cells with MKC-231, STS, and CFTR rescue molecules to assess their effect on CHT1 expression. None of the treatments were effective at increasing CHT1-I294T mutant expression. In contrast, D349N-CHT1 is more abundant than WT, has appropriate localization but is a complete loss of function mutation. Based on the residual activity of I294T mutant, the treatment for the patient was altered and his condition improved.

Another example of diseases that can be caused by inherited mutations is distal renal tubular acidosis, (dRTA), which is characterized by metabolic acidosis, the inability to acidify the urine, hypokalemia, decreased bone density, difficulty to thrive and eventually chronic kidney disease. One of the key proteins involved in acid base balance in the collecting duct is the kidney anion exchanger 1 (kAE1) which, when mutated, can result in dRTA. Recently, a mouse

model of dRTA that carry the kAe1 R607H knock-in mutation (R589H human equivalent), displayed a decrease in alpha intercalated cells and abnormal localization of the v-H^+-ATPase. In the remainder of the A-ICs, there was accumulation of p62 and ubiquitin, both markers of autophagy. This motivated us to look further into autophagic cell death as a potential factor in the progression of dRTA. Using both *in vitro* and *in vivo* models, we uncovered some mechanisms that may explain the molecular events occurring in dRTA. In this study, we used mIMCD cells expressing kAE1 WT, R295H, S525F (both are unpublished dRTA causing mutations) and previously reported R589H, as well as R607H mice. The lab previously found that mutant mIMCD cells were unable to acidify intracellularly to the same extent as WT mIMCD cells. As cytosolic pH has an effect on autophagy by regulating the mammalian target of rapamycin (mTOR), we hypothesized that this may be the mechanism underlying altered autophagy in dRTA. Using immunoblot, we observed a decrease in autophagy in R295H and S525F mutant cells that was not appropriately upregulated when autophagy was induced via starvation. Using lysosomal staining, we identified that the S525F mutant cells also have an increase in the number of lysosomes. In the R589H mutant cells we observed an increase in autophagy flux that could not be appropriately suppressed. This mutant also displayed enlarged lysosomes, also supporting abnormal autophagy. Unfortunately, some of these methods were unreliable in the mouse model but initial findings indicate that autophagy is altered in the R607H knock-in mice as well.

Preface

Unless stated otherwise, all work in this thesis is the original work of Midhat Rizvi.

Ethics

Research done in chapter 2 was approved by the NYU Grossman School of Medicine Institutional Review Board (Protocol s18-01743) and by the University of Alberta Health Research Ethics Board (Pro00121079). Informed consent was obtained from the parents and conduct of the study followed all regulatory and ethical guidelines per the approved study protocol and US Federal regulations for the protection of human subjects.

Research done in chapter 3 was approved and the animal protocol number is AUP1277.

Chapter 2

Chapter 2 was a collaborative work is submitted for publication as the following manuscript: "Biochemical characterization of two novel mutations in the human high-affinity choline transporter 1 identified in a patient with congenital myasthenic syndrome." Clinical work was completed by the Pediatric Undiagnosed Diseases Program under the supervision of Dr. Gilad Evrony. Tina Truong is responsible for **Figure 2.1A** and **Figure 2.5.** The cell surface biotinylation experiments were completed by Dr. Janet Zhou corresponding to **Figure 2.2.** **Figure 2.6** was created by Dr. Emmanuelle Cordat.

Chapter 3

Work was completed with the help of Jared Bouchard, an undergraduate student at the time, who I directly supervised for the 2019-2020 academic year. I did the experimental treatments and Jared Bouchard helped lyse the cells for half of the experiments. He ran about half of the blots of the dRTA mutant cell lines. Jared Bouchard and Grace Essuman (graduate student) counted and measured the lysosomes. Experiments from **Figure 3.2** were done by Dr. Rawad Lashhab.

Dedication

I dedicate this thesis to Zainab bint Ali (as), my role model who stood up against injustice 1400 years ago. I thank Allah (swt) for giving me the strength to complete this endeavor.

I would also like to dedicate this to my supervisor Dr. Emmanuelle Cordat, who supported me since I was an undergraduate summer student. She helped me not only academically, but also through mentorship and guidance. I would also like to dedicate this to my fellow graduate students especially Forough, Grace, and Priyanka, with whom I have become very close friends with.

I dedicate this thesis to my grandmothers who believed in me and supported me, I love you two. I also dedicate this thesis to my mother, father, sister and two brothers who knew I could do it, even when I thought I could not. Finally, I dedicate this to my husband, Raza, who supported me throughout, shared my stress, and made sure I did the best I could, I love you!

Acknowledgements

I would like to thank the funding agencies that supported my work. Thank you to the Women and Children Health Research Institute for supporting my first project titled "Biochemical Characterization of two novel mutations in the human high-affinity choline transporter 1 identified in a patient with congenital myasthenic syndrome". Thank you to the Kidney Foundation of Canada for funding and supporting the second project titled "The link between mutant kAE1 and autophagic cell death in distal renal tubular acidosis". I'd also like to thank The Canadian Institute of Health Research and the University of Alberta for funding my work.

Table of Contents

List of Figures

List of Tables

Glossary of Terms

ACh	Acetylcholine
AChE	Acetylcholinesterase
AChR	Acetylcholine receptors
AD	Autosomal dominant
ADHD	Attention deficit hyperactivity disorder
AE1	Anion exchanger 1
4E-BP1	Eukaryotic translation initiation factor 4E-binding protein 1
ANS	Autonomic nervous system
AQP 2	Aquaporin 2
AR	Autosomal recessive
ATG	Autophagy related genes
B-ICs	Beta intercalated cells
BL	Basal lamina
CAII	Carbonic anhydrase II
CCD	Cortical collecting duct
Ch	Choline
CHT1	Choline transporter 1
CKD	Chronic kidney disease
CMS	Congenital myasthenic syndrome
CNS	Central nervous system
CO_2	Carbon dioxide

dRTA	Distal renal tubular acidosis
eIF4E	Elongation initiation factor
ENaC	Epithelial sodium channel
ER	Endoplasmic reticulum
EV	Empty vector
HACU	High affinity choline uptake
HC-3	Hemicholinium
HA	Hemagglutinin
IBS	Irritable bowel syndrome
ICs	Intercalated cells
ICT	Initial collecting tubule
iMCD	Inner medullary collecting duct
kAE1	Kidney anion exchanger 1
kDa	Kilodalton
LACU	Low affinity choline uptake
LC3BI	Microtubule-associated proteins 1A/1B light chain 3B
MDCK	Madin Darby canine kidney
mIMCD	Mouse inner medullary collecting duct cells
mTOR	Mammalian target of rapamycin
NDCBE	Na^+ driven Cl^-/HCO_3^- exchanger
NKCC1	Na^+-K^+-$2Cl^-$ cotransporter
NMJ	Neuromuscular junction
oMCD	Outer medullary collecting duct

p53	Tumor protein p53
p62	Sequestosome 1
PC	Principal cells
PCT	Proximal convoluted tubule
PE	Phosphatidylethanolamine
PNS	Peripheral nervous system
PST	Proximal straight tubule
PT	Proximal tubule
ROMK	Renal outer medullary potassium transporter
SDS-PAGE	Sodium dodecyl sulfate polyacrylamide gel electrophoresis
TMD	Transmembrane domain
VAChT	Vesicular acetylcholine transporter
v-H^+ ATPase	Vacuolar-type H^+ ATPase
WT	Wildtype

Chapter 1 General Introduction

Thesis overview

During my masters, I investigated the pathophysiology associated with two mutated membrane proteins causing genetically inherited diseases in two different yet slightly overlapping fields in physiology – neural and renal physiology.

For the former, which is described in Chapter 2, I characterized two new mutations in the high affinity sodium/choline transporter 1 (CHT1) that cause congenital myasthenic syndrome (CMS), in collaboration with New York University's Pediatric Undiagnosed Diseases Program. As a result of this work, clinicians were able to modify the patient's treatment regimen which translated in improved quality of life.

For the latter project, described in Chapter 3, I was able to uncover some of the underlying cell death mechanisms that lead to the phenotype seen in patients with distal renal tubular acidosis (dRTA). Although these areas of research are different, there are many common aspects in these two projects: both CMS and dRTA are the result of genetic mutations, both CMS and dRTA research used a bench-to-bedside approach, and the techniques used, and the *in vitro* approaches were similar. The knowledge acquired during this Master's work ameliorated the quality of life of a previously mis-diagnosed CMS patient and significantly improved our understanding of dRTA.

Chapter 4 summarizes findings from the previous 2 chapters, discusses the limitations of these studies and proposes leads for future studies.

Introduction of Project 1: Congenital Myasthenic Syndrome

The neuromuscular junction (NMJ) is the area between a muscle and a motor neuron end plate, which through acetylcholine (ACh) release, allows for transfer of nerve impulses to muscles, eventually leading to a contraction. Mutations of genes encoding NMJ proteins lead to the development of congenital myasthenic syndromes (CMS). Currently, we know of 34 genes that may be affected in CMS (Pardal-Fernández, et al., 2018) resulting in a spectrum of phenotypes. CMS in its extremist form is fetal akinesia, which is characterized by reduced prenatal movements, generalized weakness after birth, inability to respirate independently and increased mortality. The majority of the fetal akinesia syndromes are caused by mutations to the acetylcholine receptor (Engel, 2018), however some can result from mutations to the choline transporter (CHT1). After ACh is broken down by acetylcholinesterase in the synapse, its rapid uptake is enabled by CHT1. This rapid uptake is also known as the high affinity sodium dependent choline reuptake via CHT1(Ferguson et al., 2004; Haga, 2014). Both knockout of *SLC5A7* gene, that encodes CHT1, (Ferguson, et al., 2004) and CHT1 inactivating mutations lead to the development of fetal akinesia syndromes and are lethal (Bauche et al., 2016; Pardal-Fernandez, et al., 2018; Wang et al., 2017).

The Nervous System

The nervous system is organized into the central nervous system (CNS) and peripheral nervous system. The CNS is comprised of the brain and spinal cord and the peripheral nervous system is subdivided into the sensory and motor systems. The motor system is further divided into the somatic and autonomic nervous systems, where the somatic nervous system is responsible for voluntary skeletal muscle contractions and the ANS is responsible for involuntary muscular process such as innervations to cardiac muscles, smooth muscles, and glands. The

peripheral nervus system is further divided into the sympathetic and parasympathetic nervous systems.

The somatic nervous system is made up of motor neurons originating from the spinal cord that innervate skeletal muscles, therefore impulses generated in the neurons have a large distance to travel before innervating the muscles. Known as the neuromuscular junction (NMJ), the connection is comprised of spinal motor neurons that make a synapse with muscle fibres. Acetylcholine (ACh) is the main neurotransmitter that results in excitatory neurotransmission. The NMJ occurs at invagination known as synaptic gutters and can be observed on muscles using scanning electron microscopy (Nishimune & Shigemoto, 2018). One motor neuron nerve terminal innervates one muscle fibre and therefore there is a one-to-one relationship between a terminal and muscle fibre. A mature muscle fibre has only one NMJ. However, one motor neuron can synapse with multiple muscle fibres through several motor neuron terminals and a motor neuron along with all the fibres it innervates is known as a motor unit.

There is no physical contact between the nerve terminal and muscle fibres and the area between is known as the synaptic cleft. The synaptic cleft contains a high concentration of acetylcholinesterase (AChE) which readily hydrolyses ACh and ensures termination of synaptic transmission. The synaptic cleft is also made up of an extracellular matrix called the basal lamina (BL) consisting of agrin (post-synaptic differentiation), collagens IV (stabilization), laminins (BL assembly), entactin/nidogen (link between laminin and collagen IV), perlecan (stability), neuregulins (growth factors), and glycoconjugates (glycosylation regulation) (Patton, 2003). The sarcolemma of the muscle fibre has an internal BL and external reticular lamina together known as the basement membrane (Gillies & Lieber, 2011; Sanes, 2003).

Muscle contractions occur via propagation of action potentials. It initiates at the presynaptic membrane on the motor neuron nerve terminal where the action potential travels down the terminal. Membrane depolarization causes an influx of Ca^{2+} ions which causes synaptic vesicles containing ACh to fuse to the membrane and release their contents into the synaptic cleft. ACh binds to ACh receptors (AChRs) on the post synaptic membrane on the muscle fibre, resulting in their opening and an influx of Na^{+} ions. This eventually leads to a muscle contraction. ACh dissociates from its receptor and is broken down by AChE in the synaptic cleft. Choline is reuptaken by the choline transporter back into the presynaptic membrane through CHT1 (Ferguson et al., 2004b; Lockman & Allen, 2002; Rylett & Schmidt, 1993). The processes occurring at the NMJ are summarized in **Figure 1.1**(Ojiakor & Rylett, 2020)**.**

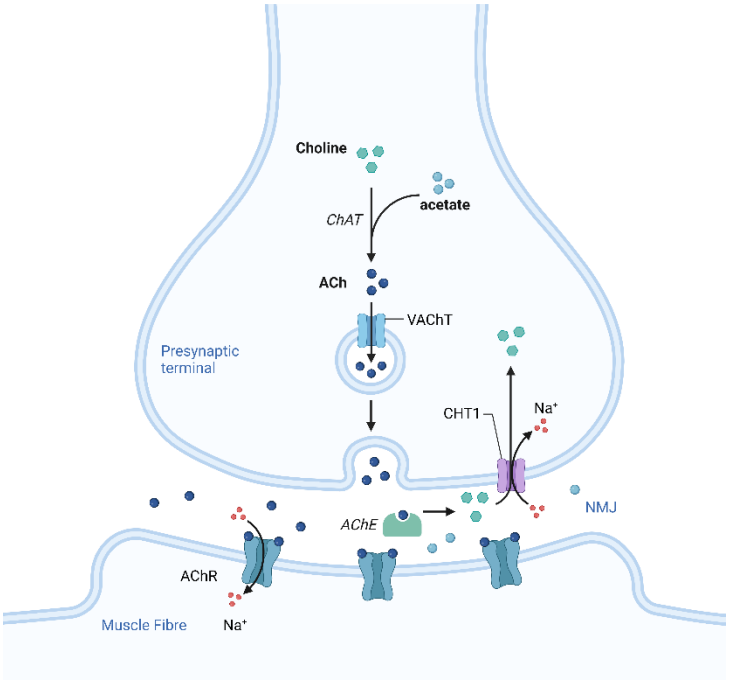

Figure 1.1 Cholinergic synapse. In the axoplasm, choline acetyltransferase (ChAT) catalyzes the reaction between acetate and choline to synthesize Ach. ACh is transported into vesicles via vesicular acetylcholine transporters (VAChT). Vesicles are released when the presynaptic membrane is depolarized via Ca^{2+} influx. ACh binds to muscarinic and nicotinic receptors (mAChR and nAChR) leading to an influx of Na^{+} ions into the post-synaptic membrane. ACh dissociates from the receptor and is enzymatically broken down into choline and acetate via acetylcholinesterase (AChE) into choline and acetate. Choline is then transported back into the presynaptic membrane via the choline transporter (CHT). Image created with BioRender.com.

Choline Transport and the Choline Transporter

In the NMJ, ACh binding to AChR allows for the influx of Na^+ ions and propagation of the action potential which eventually results in a muscle contraction. Unlike other neurotransmitters, ACh is enzymatically broken down into choline (Ch) and acetate via acetylcholinesterase. The Na^+-dependent, hemicholinium-3 (HC-3) sensitive, high affinity choline uptake transport (HACU, K_m = 1-5 μM) and a HC-3-insensitive, Na^+-independent low affinity choline transport (LACU, K_m = 100 μM) allows for Ch reuptake and recycling (Lockman & Allen, 2002; Ribeiro et al., 2006; Rylett & Schmidt, 1993). Most importantly, HACU is mediated by the choline transporter (CHT1) (Okuda et al., 2000; Okuda & Haga, 2003). CHT1 mutations impair Ch reuptake and recycling to ACh via choline acetyltransferase in the presynaptic membrane.

Dietary choline (Ch) is essential and Ch synthesis does not occur in cholinergic neurons and thus HACU via CHT1 is required for normal neurotransmission (Haga & Noda, 1973; Scremin & Jenden, 1991). HACU is limited to cholinergic neurons where the concentration of Ch is low and the ubiquitous Na^+-independent transport occurs where the Ch concentration is high (Haga & Noda, 1973; Okuda et al., 2000). About 60% of the Ch taken up by the cell via HACU is converted to ACh and only a minute amount of Ch is used to synthesize ACh in the Na^+-independent pathway (Haga & Noda, 1973; Okuda et al., 2000). Therefore, HACU is necessary for ACh synthesis as demonstrated by the death of CHT1 knockout mouse model shortly after birth (Bazalakova & Blakely, 2006; English et al., 2010; Ferguson et al., 2004b; Matthies et al., 2006).

CHT1 is found mainly in cholinergic neurons colocalizing with the vesicular ACh transporter (VAChT) (Ferguson et al., 2003; Okuda et al., 2000). The VAChT transports ACh into vesicles thus allowing its subsequent release. CHT1 is non homologous to other neurotransmitter transporters such as the dopamine transporter, but, is homologous to the Na^+-dependent glucose transporter family (Okuda et al., 2000). CHT1 is comprised of 580 amino acids, contains 13

transmembrane domains with an extracellular amino terminus and an intracellular carboxyl terminus and forms homo oligomers on the plasma membrane (Okuda et al., 2012). CHT1 has a molecular weight of 65-70 kDa and can be *N*-glycosylated (Bazalakova & Blakely, 2006; Okuda et al., 2012). Additionally, the role of CHT1 phosphorylation remains largely unknown but it is regulatory (Ferguson et al., 2004b; Lockman & Allen, 2002; Rylett & Schmidt, 1993). As mentioned previously, CHT1 KO and loss of function mutations are lethal. Mutations in *SLC5A7* result in congenital myasthenic syndromes in humans.

Congenital Myasthenic Syndromes

Congenital Myasthenic Syndromes are caused by mutations in the synaptic machinery. Of the 34 known genes that can be affected in CMS, 8% affect proteins of the presynaptic membrane (Pardal-Fernández et al., 2018). Some of the presynaptic proteins that may be affected include SNAP25B, synaptotagmin 2, Munc13-1, synaptobrevin-1, GFPT1, DPAGT1, ALG2, ALG14, Agrin, GMPPB, LRP4, myosin 9A, collagen 13A1, the mitochondrial citrate carrier, PREPL, LAMA5, the vesicular ACh transporter, and the most relevant to this work, CHT1 (Engel, 2018; Engel et al., 2015). The clinical phenotype of CMS includes fatigable weakness especially altering cranial muscle function, aberrant electromyographic response, abnormal single fiber electromyographic response, autophagic myopathy, hypotonia, respiration abnormalities along with a clinical history of CMS (Engel et al., 2015). Mutations in *SLC5A7* that result in aberrant CHT1 function result in CMS type 20.

CHT1 mutations resulting in CMS Type 20

Five studies to date have correlated *SLC5A7* mutations with neuromuscular junction defects. Wang and colleagues described three homozygous *SLC5A7* mutations in three families. They

include p.Ser94Arg, p.Val112Glu, and p.Pro210Leu. Ser94 and Val112 are highly conserved across species while Pro210 is not conserved to the same extent. The phenotypes varied from the classical presentation of CMS (Pro210Leu), to generalized neurodevelopmental delay coupled with brain atrophy (Ser94Arg) and infantile lethality (Val112Glu) (Wang et al., 2017). Wang and colleagues hypothesized that aberrant protein trafficking and localization lead to these phenotypes using *in vitro* studies. In the second study, Pardal-Fernández and colleagues described an infant who had acute respiratory failure, generalized weakness, and severe hypotonia. As a compound heterozygous mutation in the *SLC5A7* was found in the patient, it was proposed that the phenotype was due to low levels of ACh released into the synapse leading to aberrant muscle fibre potentials (Pardal-Fernández et al., 2018). AChE inhibitors improved the patient's condition but only for a short period of time because the impaired presynaptic CHT1 is not dependent on the gradient of Ch (Pardal-Fernández et al., 2018). In 2016, Bauche and colleagues described 11 recessive *SLC5A7* mutations in 6 unrelated families with clinical symptoms ranging from CMS with episodic apnea to a lethal antenatal type of arthrogryposis (Bauché et al., 2016). These mutations are inactivating and traditional treatments for autonomic myasthenias were ineffective (Bauché et al., 2016). Fourth, Banerjee and colleagues have identified the p.Ser263Phe mutation in SLC5A7 that results in the lethal form of CMS and fetal akinesia (Banerjee et al., 2019). More recently, 3 novel mutations found by Rodriguez Cruz and colleagues resulted in presynaptic CMS with varying weaknesses including fatality (Rodríguez Cruz et al., 2021). Taken together, mutations affecting CHT1 have detrimental outcomes (summarized in Table 1) ranging from the classical form of the disease to lethality. Positions and effect of CHT1 mutations are summarized in **Table 1.1** and **Figure 1.2**.

Table 1.1. Categories of CMS Type 20 phenotypes.

Type	Characteristics
Neonatal Phenotype	• Apnoeic episodes from birth • Generalised hypotonia • Bulbar weakness & oculofacial symptoms • Cognitive and behavioural symptoms later in life • Good response to cholinesterase inhibitors & β2-adrenergic agonists
Generalized/Severe Phenotype	• Hypotonia • Lack of respiration and spontaneous movement • Severe bulbar weakness • Central deficits & lack of response to external stimuli
Antenatal Phenotype	• Lethal • Hydroamnios • Generalized hypotonia • Severe respiratory distress • Arthrogryposis • Brain atrophy & other malformations

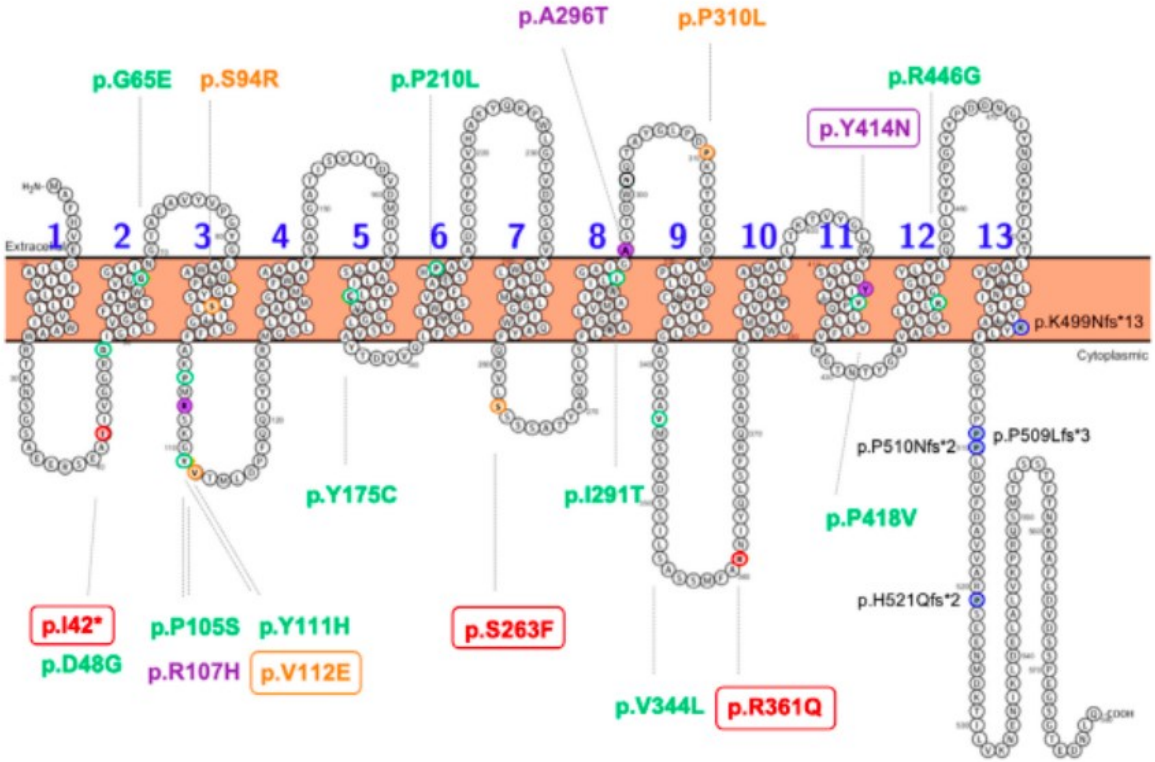

Figure 1.2 Positions of mutations in CHT1**.** Green represents CMS with episodic apnea (neonatal phenotype), orange is the generalized phenotype, and red is the antenatal phenotype. Blue represents mutations in CHT1 that result in distal hereditary motor neuronopathy VII. Boxes denote lethality. Figure modified from (Rodríguez Cruz et al., 2021) with permission.

CHT1 mutations in the context of other disease

There are several other diseases associated with cholinergic dysfunction. Truncating mutations at the C-terminus of CHT1 cause distal hereditary motor neuropathy type VIIa with muscle wasting and vocal cord paresis (Barwick et al., 2012; Salter et al., 2018). Additionally, *SLC5A7* single nucleotide polymorphisms are associated with higher rates of attention deficit hyperactivity disorder (ADHD)(English et al., 2009). Alterations in CHT1 HACU is also associated with neurodegenerative disorders such as early onset familiar Alzheimer's disease, and mutations in presenilin-1, such as p.M146V, result in a decrease of choline uptake via CHT1 through reduced affinity without altering CHT1 abundance (Payette et al., 2007). CHT1 function is also implicated in irritable bowel syndrome (IBS) and upregulation of HACU via MKC-231 provided relief to rats with IBS accompanied by hyperalgesia (M. J. Lin & Yu, 2018). CHT1 is also implicated in the pain that arises from chronic pancreatitis and increased CHT1 activity or expression may be used to alleviate the pain associated with this condition (Luo et al., 2017). Polymorphic variations in CHT1 are also associated with carotid atherosclerosis in humans (Neumann et al., 2012).

Introduction of Project 2: dRTA

Distal renal tubular acidosis (dRTA) is characterized by metabolic acidosis, hypercalciuria, nephrocalcinosis, hypokalemia, hyperchloremia, decreased bone density, difficulty thriving and eventually chronic kidney disease (CKD) if untreated. Inherited forms of dRTA are autosomal dominant or autosomal recessive and are caused by mutations in the kidney anion exchanger 1 or the v-H^+-ATPase among other genes. The mechanisms by which this occurs is not fully understood. Acid-base homeostasis is important for survival and thus understanding the mechanisms underlying dRTA is of utmost importance. Recently, Mumtaz et al have shown the loss of alpha intercalated cells in the kidneys of dRTA mice(Mumtaz et al., 2017). Of the cells that remained, they found an accumulation of p62 and ubiquitin, 2 markers of autophagy, as well as inappropriate cytosolic localization of the v-H^+-ATPase. This prompted us to understand autophagic processes *in vitro* as well as *in vivo.* The focus of this section of the thesis is on deciphering the cellular processes that lead to dRTA. Our lab previously found that *in vitro,* mouse inner medullary collecting duct (mIMCD) cells that carry mutated kAE1 do not acidify their cytosol to the same extent as WT mIMCD cells. Differences in cytosolic pH can alter autophagic processes(Balgi et al., 2011; Kazyken et al., 2021). As such, we hypothesized that the change in basal cytosolic pH can alter autophagy and result in autophagic death. We used mIMCD cells and transgenic mice to study autophagy and uncover whether it is altered. Overall, we found that autophagic processes are altered in mutant cells and in dRTA mice. Although there is more research to be done, we are one step closer to understanding what is occurring in dRTA.

Urinary system

The human urinary system is composed of two kidneys, two ureters, a bladder and the urethra, and is connected to the body via the cardio-vascular system. It also receives innervations through

the peripheral nervous system. The kidney is a vital organ, but we can survive on one kidney. Known as the nephron, the smallest functional unit of the kidney, spans both the medulla and the cortex. Filtration, reabsorption, secretion and excretion of numerous ions, toxins, amino acids and other molecules occur in the nephron. The kidney also plays an important role in acid base homeostasis, mostly in the proximal convoluted tubule. However, there are some processes involved in acid-base homeostasis occurring in the connecting tubules and the collecting duct.

The urinary system begins to form as early as week 4 of gestation and it arises from the mesoderm, known as the urogenital apparatus (Dressler, 2006). The urogenital apparatus is divided into the excretory system and the reproductive system. Three distinct excretory structures develop in the embryo: pronephros, mesonephros and metanephros. The metanephros turns into the kidney while the other two structures disappear (Chertow et al., 2019; Costantini & Kopan, 2010; Dressler, 2006). The non-functional pronephros is the first to develop and is a part of the Wolffian duct system which ultimately turns into the gonads. Mesonephros is the second one and it is briefly functional as it dumps into the cloaca until the permanent kidneys appear. It also turns into the Wolffian body and eventually the ureteric bud (Zweyer, 2014). The kidneys form from the metanephros and the reciprocal inductive interactions between the metanephric mesenchyme and the ureteric bud (Chertow et al., 2019; Zweyer, 2014).

Kidneys

Galen is thought to be the founding father of experimental renal physiology as he showed that urine is formed in the kidney as opposed to the bladder, an Aristotelian view (Eknoyan, 1989). Galen was correct and kidneys are also necessary to sustain life. Kidneys are bean shaped organs found on either side of the retroperitoneal space of vertebrates. Kidneys consist of three main

sections: the renal capsule, cortex, and medulla. The renal capsule consists of fibrous connective tissue and serves as a protective barrier for the kidney. The cortex is the outer part of the kidney, and it consists mainly of nephrons which also extend down towards the medulla. The Medulla is the inner most part of the kidney and consists mainly of the collecting ducts of the nephrons which converge, and form papillae surrounded by the minor calyces. This gives rise to an inverted pyramidal shape, known as the renal pyramids and the base is found at the corticomedullary junction and the tips are the papillae. Minor calyces further converge and form a major calyx, which are two-three minor calyces. The major calyces converge to form the renal pelvis, and this exits the kidney through the hilum along with blood vessels and nerves. The nephrons are complex units of the kidney where each section contributes to different aspects of the excretory/reabsorption system.

Nephrons

The nephrons have a unique structure that starts with the renal corpuscle comprised of the glomerulus and the Bowman's capsule. The glomerulus filters large volumes of plasma to form primary urine. The glomerulus is composed of endothelial cells, mesangial cells, and podocytes. The Bowman's capsule surrounds the glomerulus. An afferent arteriole enters the glomerulus, and an efferent arteriole exits the glomerulus. The plasma that enters the glomerular capillaries through the afferent arteriole is filtered and the filtrate is called pro-urine. The small fenestrations (70-100 nm) formed by the endothelial cells of the glomerular capillaries permit the filtration of the plasma. The second layer of the filter is a basement membrane composed of extracellular proteins including collagen (IV), laminins, fibronectins and proteoglycans (Pollak et al., 2014). The outer part of the filter unit is made of podocytes, which are epithelial cells with finger like projections, that make up the filtration slit diaphragm and are important for supporting

the capillary loops. The sophisticated filtration system does not normally allow for the passage of large protein molecules such as albumin or RBCs and the filtrate fill the space between the capillaries and capsule, known as Bowman's space, before entering the proximal convoluted tubule (PCT). The transition to the PCT starts with parietal epithelial cells lining the inner part of Bowman's capsule which then switch to the characteristic cuboidal cells of the PCT at the urinary pole (Chertow et al., 2019).

The proximal tubule (PT) consists of cuboidal epithelial cells divided in the pars convoluta (proximal convoluted tubule, PCT) and pars recta (proximal straight tubule, PST). The PT can also be divided into the three segments, S1, S2 and S3, all having different cellular features. S1 and S2 are a part of the PCT and a small portion of S2 and all of S3 is a part of the PST (Chertow et al., 2019). This section of the PT is where most reabsorptions of ions (Na^+, HCO_3^-, Cl^-, K^+, Ca^{2+}, PO_4^{3-}), glucose, vitamins, amino acids and water occur. Secretion of organic anions, ammonia and protons occur in that segment as well. The epithelial cells have microvilli on the luminal/apical side visible under a scanning electron microscope, which greatly increase the surface area for reabsorption(Andrews & Porter, 1974). The basal side of the cells have a high concentration of mitochondria which are necessary to create the driving force for ions such as Na^+ through active transport. These cells also form lateral connections with neighboring cells to only allow selective paracellular and transcellular transport.

The next segment of the nephron, called the Loop of Henle consists of the thin descending limb, the thin ascending limb, and the thick ascending limb. The main function of the Loop of Henle is to reabsorb water, Na^+, Cl^-, K^+ resulting in a concentrated urine. This loop is followed by the distal convoluted tubule, connecting tubule, and finally the collecting duct. Cells from the collecting duct are the focus of this thesis.

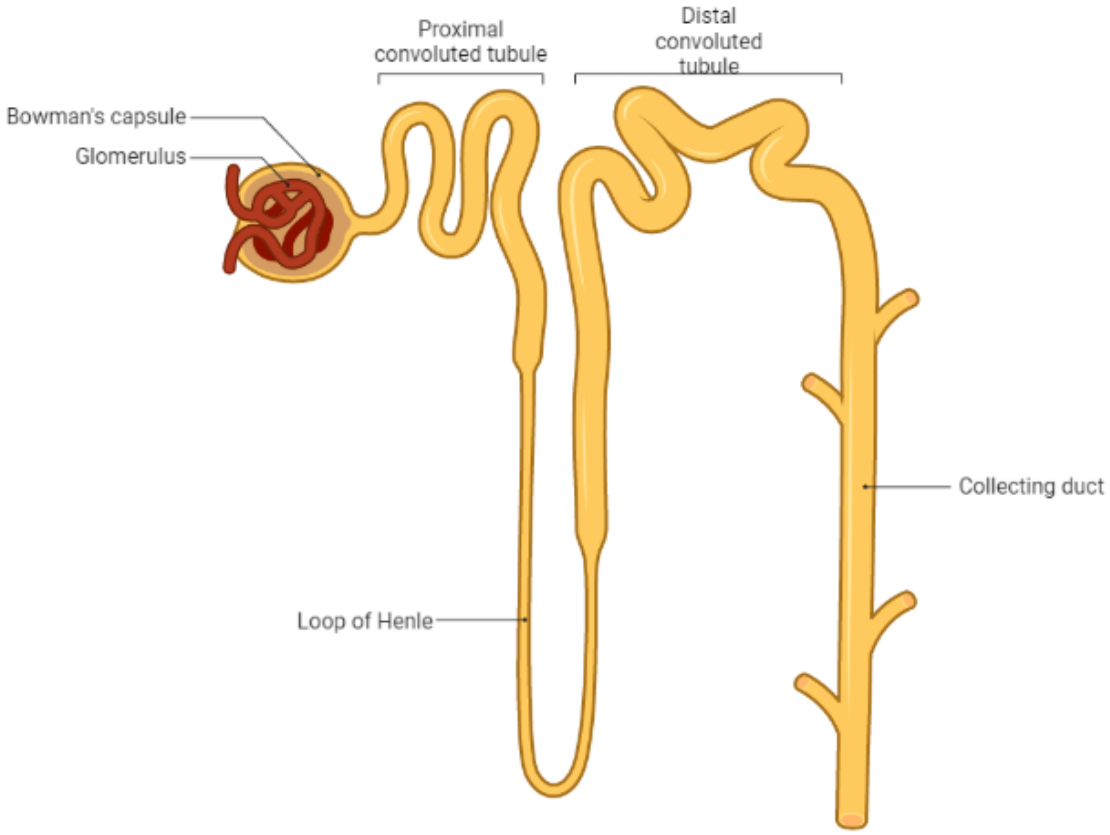

Figure 1.3. Anatomy of a nephron. Adapted from "Selective Reabsorption in the Nephron", by BioRender.com (2022). Retrieved from https://app.biorender.com/biorender-templates

Collecting duct

The collecting duct consists of many segments, and it begins at the distal part of the connecting tubule in the cortex and ends at the papillae. Segments are determined by their location in the kidney, and they include the initial collecting tubule (ICT), cortical collecting duct (CCD), outer medullary collecting duct (oMCD) and the inner medullary collecting duct (iMCD). There are two main cell types in the collecting duct: the principal cells (PC) and the intercalated cells (ICs). They appear as light cells (PC) and dark cells (ICs) under scanning electron microscope (Andrews & Porter, 1974). The dark cells have more intracellular organelles and are electron dense in comparison to the light cells and the pioneering study by Schachowa showed that the dark cells stained darker with hematoxilin and eosin (Andrews & Porter, 1974; Ordonez & Spargo, 1976). Dark cells also appear to have more supranuclear mitochondria. There are fewer intercalated cells than principal cells and intercalated cells decrease as the nephron moves towards the cortex and disappear entirely near the papillae (Nicholson, 1982; Ordonez & Spargo, 1976). Intercalated cells are covered with microplicae / folds or a dense pedicel like projections and the principal cells are covered with a few short microvilli with one or two central cilia (Andrews & Porter, 1974; Madsen et al., 1988; Ordonez & Spargo, 1976). Interestingly, there is a transitory cell between the light and dark cells that may represent different forms of the same cells and they are more apparent when animals such as rats are stressed with potassium depletion (Ordonez & Spargo, 1976). The intercalated cells can be further categorized into alpha (A-ICs), beta (B-ICs) or non-alpha non beta intercalated cells (non-A non-B ICs) and are summarized in **Figure 1.4**.

Required for water and salt homeostasis, PC are defined by its major transporters including the epithelial sodium channel (ENaC) and aquaporin 2 (AQP2), a water channel

(Pearce et al., 2015). ENaC is regulated by aldosterone and AQP2 is regulated by arginine vasopressin. Both work in concert to regulate Na^+ and K^+ concentrations, blood pressure as well as extracellular fluid volume (Pearce et al., 2015).

B-ICs have a dense cytoplasm, an abundance of mitochondria, a smoother apical membrane, and more intracellular vesicles, which is visible under transmission electron microscopy (Madsen et al., 1988). B-ICs contain apical pendrin, a bicarbonate and chloride exchanger and a basolateral H^+-ATPase. This is mirror to what is seen in A-ICs. These cells also contain the anion exchanger 4 which exchanges chloride for bicarbonate and a Na^+ driven Cl^-/HCO_3^- exchanger (NDCBE) on their apical side (Roy et al., 2015). B-ICs also play a role in acid-base homeostasis, as these cells reabsorb protons through the basolateral H^+-ATPase in case of alkalosis. (Roy et al., 2015)

A-ICs contain carbonic anhydrase II (CAII) which catalyzes the hydration of CO_2 to bicarbonate and protons, and apical H^+-ATPase which pumps protons across the plasma membrane into the extracellular space (Roy et al., 2015). They also characteristically express kidney anion the exchanger 1 (kAE1, encoded by *SLC4A1*) on the basolateral side which exchanges bicarbonate for chloride. Additionally, A-ICs express H^+/K^+-ATPase on the apical membrane which exchanges a H^+ for K^+ via active transport. Ammonia is also secreted through apical ammonia transporters known as the Rh C Glycoprotein ammonia transporter (RhCG). A basolateral ammonia transporter known as Rh B glycoprotein (RhBG) is also present. A-IC also contain AE11, an electrogenic Cl^- transporter and Cl^-/HCO_3^- exchanger as well as NKCC1 which is a Na^+-K^+-$2Cl^-$ cotransporter and a big potassium channel that secretes K^+(Rieg et al., 2007). A-ICs also lack some proteins found on B-ICs, such as pendrin. A-ICs are also morphologically different than B-ICs as they have larger luminal microprojections and a well-developed

tubulovesicular membrane (Madsen et al., 1988). A-ICs play an important role in acid base homeostasis, for instance, in the case of acidosis, these cells reabsorb bicarbonate to buffer the acidic plasma pH via kAE1. The key proteins and processes of A-ICs, B-ICs and PCs are summarized in **Figure 1.4**(Roy et al., 2015)**.**

Non-A, non-B ICs represent a third type of IC. They contain proteins that are found in A-ICs and B-ICs: CAII, apical/diffuse H^+-ATPase, apical pendrin (characteristic of B-ICs), RhBG and RhCG. Evidence suggests that these cells represent different states of differentiation (Al-Awqati, 1996) and that the number of intercalated cells does not change in response to acidosis, rather the proportion of A-ICs/B-ICs increases and vice versa in the case of alkalosis (Purkerson et al., 2010; Sabolić et al., 1997). This conversion has been shown to be mediated by an extracellular matrix protein called hensin, whose loss results in a lack of A-ICs completely (Al-Awqati, 1996; Gao et al., 2010).

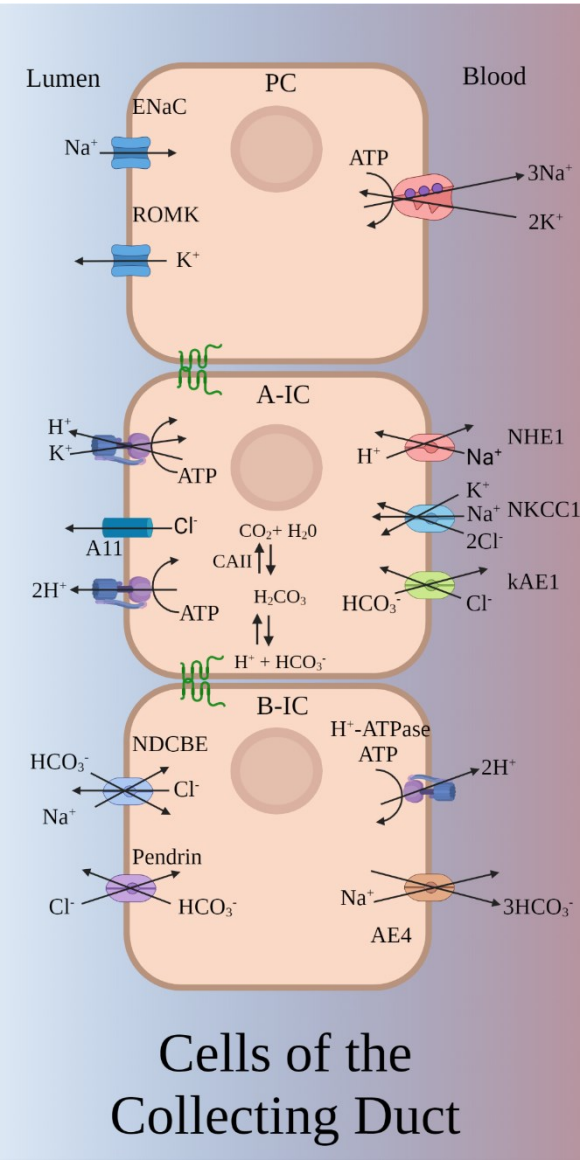

Figure 1.4: Three cell types in the collecting duct. ENaC: epithelial sodium channel, ROMK: renal outer medullary potassium channel, NHE1: sodium/hydrogen exchanger 1, NKCC: sodium/potassium/chloride cotransporter 1, AE1: anion exchanger 1, NDCBE: sodium driven chloride/bicarbonate exchanger, AE4: anion exchanger 4, A-IC: alpha intercalated cells, and B-IC: beta intercalated cells. Image created with BioRender.com.

kAE1 Structure and Function

kAE1 is a truncated form of the anion exchanger 1 (AE1), also known as Band 3, found in the plasma membrane of red blood cells (Brosius et al., 1989). kAE1 is missing the first 65 residues on the N-terminal cytoplasmic domain of AE1. This 846 amino acid protein has 14 transmembrane domains (TMD) with both intracellular N- and C –termini (Arakawa et al., 2015). It also carries one N-glycosylation site at asparagine 642. The structure of AE1 is summarized in **Figure 1.5.** kAE1 is expressed on the basolateral membrane of A-ICs in the distal nephron as detailed below (Alper et al., 1989) .

The most abundant plasma membrane glycoprotein of the RBCs, AE1 carries out Cl^- /HCO_3^- exchange, which is necessary for respiration(Cabantchik & Rothstein, 1974). CO_2 diffuses into the cell, is converted into carbonic acid, which is then broken down by CAII to produce protons and bicarbonate. Bicarbonate is carried out by AE1 in exchange for one Cl^-. In the lungs, the equilibrium is shifted: due to a lower partial pressure of CO_2, bicarbonate enters RBCs through band 3 and is converted back into CO_2 via CAII. CO_2 then diffuses out of the cell and is eventually expired through the lungs. Several morphological and anemic disorders are associated with mutations in AE1, for example the Southeast Asian Ovalocytosis(Wrong et al., 2002). In the kidney, kAE1 is responsible for acid-base homeostasis.

In a similar process to red blood cells, when CO_2 enters the A-ICs, it is broken down into bicarbonate and a proton. The proton is secreted into the lumen via the H^+-ATPase and the H^+/K^+-ATPase through primary active transport. The bicarbonate is transported by kAE1 into the blood where it can act as a buffer for maintaining a neutral blood pH. Cl^- is transported into the A-ICs through kAE1.

A B

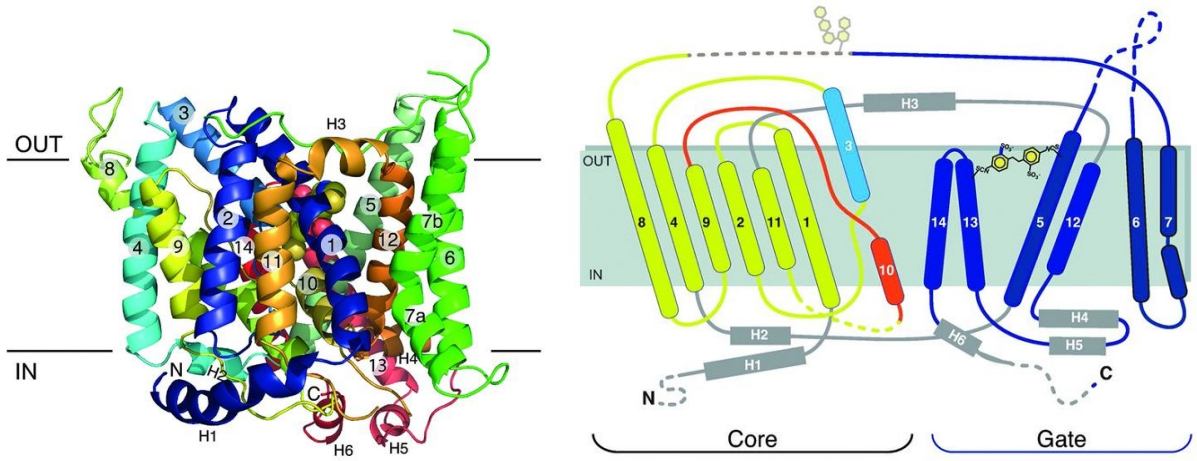

Figure 1.5. 3D and topological model of AE1. **(A)** 3D structure of AE1 with blue N-terminus and C-terminus in red. **(B)** topological model of AE1. Recall that kAE1 lacks 65 residues at the N-terminus. Image reproduced from (Arakawa et al., 2015) with permission.

Distal Renal Tubular Acidosis and kAE1

Distal renal tubular acidosis (dRTA) is characterized by metabolic acidosis, hypercalciuria, nephrocalcinosis, hypokalemia, hyperchloremia, decreased bone density, difficulty thriving and eventually chronic kidney disease (CKD) (Karet et al., 1998; Norgett et al., 2012; Stover et al., 2002; Yaxley & Pirrone, 2016). Inherited forms of dRTA in humans is caused by mutations in *SLC4A1* which encodes kAE1, and *ATP6V1B1*, *ATP6V0A4, ATP6V1C2* which encode for three subunits of the H^+-ATPase. dRTA is specific to the connecting tubule and collecting duct where A-IC cells are located. (Finberg et al., 2005; Karet et al., 1998; Mumtaz et al., 2017; Norgett et al., 2012; Sly et al., 1983; Stover et al., 2002; Yaxley & Pirrone, 2016). Several mutations are reported to cause dRTA.

Both autosomal dominant (AD) and autosomal recessive (AR) forms of dRTA are reported and several molecular mechanisms are hypothesized. For instance, dominant mutants such as kAE1- R589H, and S613F display normal anion function but do not have appropriate localization on the plasma membrane and are retained intracellularly, colocalizing with the endoplasmic reticulum (ER) (Yenchitsomanus et al., 2005). Other dominant mutants such as kAE1 R901X and S613F display mistargeting to the apical membrane in addition to normal trafficking to the basolateral membrane in polarized Madin Darby canine kidney (MDCK) cells(Yenchitsomanus et al., 2005). The autosomal recessive mutant kAE1 G701D is retained in the Golgi apparatus, while the recessive kAE1 S773P mutant is not sufficiently abundant at the basolateral membrane in MDCK cells (Cordat et al., 2006). In a *SLC4A1* knockout mouse model, these mice exhibited dRTA characterized by metabolic acidosis, nephrocalcinosis, a severe urinary concentration defect. These mice had decreased basolateral bicarbonate and chloride

exchange in their A-ICs but other bicarbonate exchange pathways were increased (Stehberger et al., 2007). The Ae1-R607H knockin mice display a decrease in A-ICs, a cytoplasmic retention of the H^+-ATPase in the remainder of A-ICs along with an accumulation of p62 and ubiquitin (Mumtaz et al., 2017). It was proposed that the murine R607H variant, equivalent to the human dominant R589H mutant may disrupt the normal trafficking of the H^+-ATPase and alter lysosome function resulting defective autophagy and cell death.

During my MSc work, I used both *in vitro* and *in vivo* methods to study dRTA cellular mechanisms. Mouse inner medullary collecting duct (mIMCD) cells expressing WT, R295H, S525F and R589H kAE1 carrying a hemagglutinin (HA) epitope were used throughout my masters to delineate cellular defects in dRTA as these mutations were identified in patients with recessive (p.R295H) and dominant (p.S525F) dRTA (unpublished data, personal communication from Dr. Rosa Varga-Poussou). Preliminary work performed prior to my arrival in the laboratory showed R295H mutant is functionally active while S525F is functionally defective. Dominant p.R589H has been previously described and is functionally active (Jarolim et al., 1998). I also used $Ae1^{+/+}$, homozygous $Ae1^{R607H/R607H}$ (human equivalent of R589H), and heterozygous $Ae1^{+/R607H}$ mice in my studies.

If untreated, dRTA eventually leads to chronic kidney disease (Reithmeier et al., 2016). This indicates that harmful molecular activities are taking place that affect the kidney. Mumtaz et al. demonstrated a loss of A-ICs and a decreased apical translocation of the H^+ -ATPase in the remaining A-ICs in a dRTA mouse model with the Ae1 R607H mutation (similar to the R589H dominant mutation in humans) (Mumtaz et al., 2017). Interestingly, they also discovered p62 and ubiquitin positive material accumulating in the remaining A-ICs. They postulated that the R607H variation could interfere with the normal trafficking of the H^+-ATPase, affecting the lysosome's

functionality, impairing autophagy, and causing cell death. These findings encouraged us to learn more about autophagy as a result.

Autophagy

A cellular process called macroautophagy, later referred to as autophagy, recycles protein and organelles while cells are under stress (Mizushima & Komatsu, 2011). It is controlled by the nutrition sensor known as the mammalian target of rapamycin (mTOR), which also tightly regulates autophagy. mTOR which is made up of two complexes (mTORC1 and mTORC2), can recognize nutrient level, and is located on the lysosomal membrane. When it is active, it phosphorylates several downstream effectors, including the inhibitory 4E-BP1 and the activating p70S6K, which ultimately causes autophagy to be suppressed. Autophagy depends on mTORC1 regulation, and pH can affect mTORC1 regulation (Balgi et al., 2011; Kazyken et al., 2021).

It was initially thought that acidic pH activates mTORC1, which in turn would inhibit autophagy(Balgi et al., 2011). However, it was recently discovered that alkaline pH activates mTORC2 and causes an additive effect on mTORC1 activation, indicating additional mechanism in mTOR regulation(Kazyken et al., 2021). mTORC2 activation inhibits apoptosis in the absence of growth factors(Kazyken et al., 2021). This means that alkaline pH increases mTOR activity which in turn would result in decreased autophagy and promote cell survival. However, uncontrolled autophagy can also lead to death in normal cells (Kang & Avery, 2008).

The development of the autophagosome, is another factor essential for autophagy besides mTORC1 regulation. Autophagosomes are double-membrane structures that contain cytoplasmic material to be recycled, which ultimately fuses with the lysosome (Yu et al., 2018) as shown in **Figure 1.6.** Microtubule-associated proteins 1A/1B light chain 3B (LC3BI) is present in the pre-autophagosomal membrane and undergoes conjugation with phosphatidylethanolamine to generate LC3BII.

LC3B on immunoblot is comprised of two bands, LC3BI and LC3BII, which is LC3BI conjugated to phosphatidylethanolamine (PE). LC3BI is cytosolic while LC3BII is found on autophagosomes, the early isolation membranes and sparsely on autolysosomes (Kabeya et al., 2000). Short starvation, less than 1 hr, increases LC3BII but longer starvation decreases both LC3BI and LC3BII (Mizushima & Yoshimori, 2007). Therefore, starvation can have a dual effect. If starvation for an extended period is causing autophagy to increase, then there will be an increase in LC3BI and LC3BII degradation. Short term starvation increases LC3BII levels and leaves LCBI levels unchanged. In contrast, under normal autophagic flux, treating cells with the vacuolar-ATPase inhibitor bafilomycin A1 (bafA1), which blocks the fusion between lysosomes and autophagosomes, increases the amount of LC3BII due to reduced degradation (Yamamoto1 et al., 1998).

Eukaryotic translation initiation factor 4E-binding protein 1 (4E-BP1) inhibits elongation initiation factor 4E (eIF4E). Phosphorylation of 4E-BP1 at S65 is a marker of decreased autophagy as the activation of mTORC1 results in the downstream inhibitory phosphorylation of 4E-BP1 (Gingras et al., 1998). An increase in phosphorylation indicates a decreased autophagy. Similarly, phosphorylation of mTORC1 S2448 indicates a decrease in autophagy as endogenous phosphorylation at S2448 binds to raptor and rictor which prevents autophagy from taking place(Rosner et al., 2010).

Accumulation of sequestosome 1 also known as p62 indicates autophagy suppression as p62 binds LC3BI and is a selective substrate of autophagy (Kuma et al., 2004). Treatment with bafA1increases p62 accumulation (Yamamoto1 et al., 1998). Also, starvation decreases p62 as it increases autophagy(Kuma et al., 2004).

Lysosomes size and number also regulate autophagy. These acidic circular organelles contain 60 types of hydrolases(Xu & Ren, 2015) including cathepsin B, an endopeptidase and dipeptidylpeptidase that is activated by an acidic pH(Mort & Buttle, 1997). Lysosomes degrade intracellular proteins via autophagy and external materials via endocytosis. The have up to 50 different types of membrane proteins which have the machinery to sense nutrient availability(Xu & Ren, 2015). These membrane proteins help determine the localization, number, size, and activity of the lysosomes which control the specificity of degradation. Upon starvation, lysosomal number is greatly reduced, and the size is increased(Xu & Ren, 2015). An increase in number of larger lysosomes indicates defective autophagy as is what happens in lysosomal storage diseases (de Araujo et al., 2020). Blocking autophagy decreases the number of lysosomes.

Using *C. elegans*, Kang and Avery found that basal level of autophagy is necessary for survival of *C. elegans* during starvation, however, both excessive or insufficient levels of autophagy result in starvation-hypersensitivity(Kang & Avery, 2008). As such, both extremes of autophagy result in an increase in cell death. This is important because this may be the cause for the loss of A-ICs in mice with the R607H Ae1 mutation that results in the loss of A-ICs(Mumtaz et al., 2017).

The macroautophagy pathway is summarized in **Figure 1.6** (Medicine, 2017).

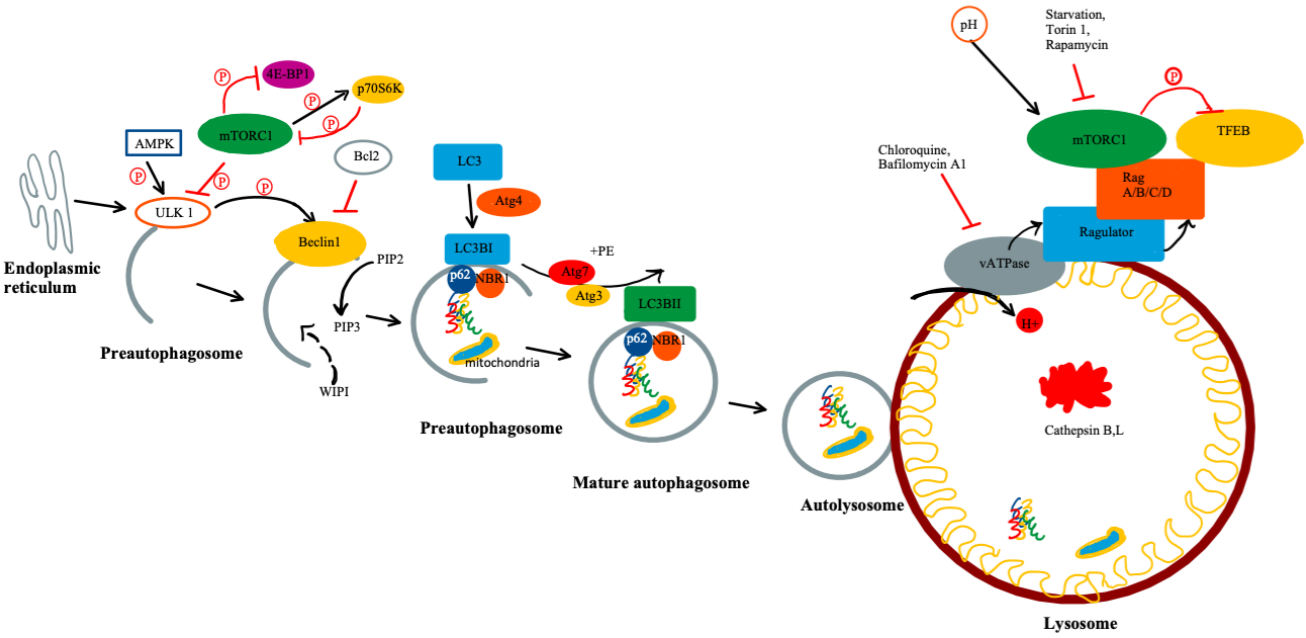

Figure 1.6 The autophagy pathway indicating key effectors such as mTORC1, LC3BI, LC3BII, the autophagosome and the lysosome.

Evidence of Autophagy in the kidney

The literature reports strong evidence of autophagy in the kidney. Podocytes have been shown to display a large flux of autophagy and it is necessary for their homeostasis (Hartleben et al., 2010). Additionally, when the gene for autophagy related 5 (ATG5) protein, *Atg5, is* knocked out both in distal and proximal tubules, an increase in misfolded proteins and deformed organelles is observed but this is not the case in distal tubule specific knockout of *Atg5* (T. A. Lin et al., 2019). However, when Ae1 is mutated in a mouse model of dRTA, an accumulation of p62 and ubiquitin is observed, indicating that Ae1 mutations may disrupt normal autophagic processes (Mumtaz et al., 2017) possibly through abnormal intracellular pH.

Research Hypotheses

In light of the findings and remaining questions highlighted above, in Chapter 2, we hypothesized that the 2 newly identified CHT1 mutations cause congenital myasthenic syndrome.

In Chapter 3, we hypothesized that dRTA mutants cause an abnormal cytosolic pH, leading to altered autophagy and autophagic death.

Chapter 2 : Biochemical Characterization of two novel Mutations in the Human High-Affinity Choline Transporter 1 identified in a patient with Congenital Myasthenic Syndrome

Introduction

The neuromuscular junction (NMJ), situated at the interface between the motor neuron end plate and the muscle, mediates acetylcholine (ACh) signaling from the neuron that stimulates muscle contraction. Pathogenic variants of NMJ proteins lead to congenital myasthenic syndromes (CMS) ranging in severity from fetal akinesia (reduced prenatal movements) and neonatal lethality to non-lethal fatigable weakness (especially of cranial muscles), hypotonia, and respiratory and feeding difficulties (Engel et al., 2015). Clinical evaluations may also reveal aberrant electromyography. Currently, mutations in 34 different genes are associated with CMS (Pardal-Fernández et al., 2018). These include genes coding for proteins involved in every step of ACh signaling: its synthesis, its receptor subunits, presynaptic reuptake of its metabolite choline, and uptake of ACh into presynaptic vesicles (Engel, 2017; Engel et al., 2015). While most cases of CMS are caused by mutations in genes responsible for post-synaptic ACh signaling (Engel, 2017), rare forms of CMS are caused by mutations affecting presynaptic processes (Pardal-Fernández et al., 2018).

In the synapse, ACh is rapidly broken down by acetylcholinesterase into choline, which is then transported back into the presynaptic motor neuron by CHT1, a Na^+-dependent and hemicholinium-3 (HC-3) sensitive (K_i 1-3 μM) choline transporter (choline K_m = 0.5-3 μM) encoded by the *SLC5A7* gene. Additional neuronal choline transport is mediated by Na^+-independent, less HC-3 sensitive (K_i 20-200 μM) lower affinity (choline K_m = 20-200 μM) choline transporters including SLC44A1 (originally termed the choline transporter-like protein 1, CTL1) (Ferguson et al., 2004a; Lockman & Allen, 2002; Rylett & Schmidt, 1993). CHT1 forms homo-oligomers at the plasma membrane and is proposed to contain 13 transmembrane domains, with an extracellular amino terminus along with an intracellular carboxyl terminus (Okuda et al., 2012). The 63 kDa molecular weight protein is also *N*-glycosylated (Bazalakova & Blakely, 2006; Okuda

et al., 2012). Additionally, evidence suggests that CHT1 function is regulated via phosphorylation (Black et al., 2010; Cooke & Rylett, 1997; Gates et al., 2004; Issa et al., 1996). Importantly, biallelic mutations in *SLC5A7* that code for CHT1 cause a presynaptic CMS syndrome with a spectrum of severity, though often the course is severe with a high rate of neonatal lethality (Bauché et al., 2016; Pardal-Fernández et al., 2018; Wang et al., 2017). Consistent with the severe form of the human *SLC5A7* CMS phenotype, homozygous *Slc5a7* knockout mice die from apnea within an hour of birth.

Given the role of CHT1 in choline reuptake that is required for resynthesis of ACh, patients with CMS due to *SLC5A7* mutations may be amenable to treatment with acetylcholinesterase inhibitors (AChEIs). AChEIs were first described as a treatment for myasthenia gravis in 1934 (*Walker MB (1934) - The James Lind Library The James Lind Library*, n.d.), and by preventing degradation of ACh, they increase its availability in the NMJ. AChEIs, including pyridostigmine, are given as first line therapy for presynaptic CMS (Engel, 2017), and they have been shown to improve muscle strength, including resolution of episodic apnea, in patients with *SLC5A7* mutations. Therefore, identification and characterization of genetic mutations in patients with CMS can have invaluable clinical impact. Early initiation of therapy is especially critical for those with impaired respiratory function, which is a common presentation of *SLC5A7*-related CMS.

Here, we report a patient with moderately severe CMS symptoms (hypotonia, developmental delay, and a history of significant neonatal respiratory difficulties) in whom we identified two novel, compound heterozygous CHT1 mutations: p.I294T and p.D349N. Through extensive biochemical studies, we show that each mutation leads to loss of CHT1 function in a different manner: premature protein degradation with some residual transporter function

(p.I294T), and transporter inactivation (p.D349N). Subsequent treatment of the patient with AChEI led to a significant improvement of symptoms and quality of life.

Materials and Methods

Ethical compliance and subject enrollment

The proband, parents, and unaffected siblings were enrolled into the Pediatric Undiagnosed Diseases Program at the NYU Grossman School of Medicine. The study was approved by the NYU Grossman School of Medicine Institutional Review Board (Protocol s18-01743) and by the University of Alberta Health Research Ethics Board (Pro00121079). Informed consent was obtained from the parents and conduct of the study followed all regulatory and ethical guidelines per the approved study protocol and US Federal regulations for the protection of human subjects.

Review of medical records

To obtain a complete view of the proband's medical history, medical records were gathered from all prior treating physicians. A complete review of the medical records was performed, including prenatal, birth, medical, and family histories along with physical exams, imaging, and laboratory tests. To help guide the research strategy given the prior non-diagnostic clinical evaluations, the summarized medical history was also reviewed by the Pediatric Undiagnosed Diseases Program study committee, consisting of a clinical geneticist, a pediatric neurogeneticist, two research geneticists, and three genetic counselors.

Research sample collection

Genetic research studies utilized saliva collected from the proband and mother using the Oragene OGR-600 collection kit. The father was unavailable for sample collection. Blood was collected from three unaffected siblings for segregation analysis. For Clinical Laboratory Improvement

Amendments (CLIA)-grade validation of research results, to enable reporting of the diagnosis to the family, new blood samples were collected from the proband and mother.

Genomic data analysis

Raw whole-exome sequencing data from prior non-diagnostic clinical testing (Roch VCRome 2.1 exome panel) were obtained and aligned to the human reference genome (hg38) with Burrows-Wheeler Alignment Tool (BWA) (Li & Durbin, 2009). Single-nucleotide and indel variants were called using the Genome Analysis Toolkit Best Practices pipeline (Van der Auwera et al., 2013) run via the Terra platform on Google Cloud. Aligned reads produced a mean target exome coverage of 154x, with 96% of the exome at ≥ 30x. Single-nucleotide and indel variants were filtered and analyzed using Ingenuity Variant Analysis (Qiagen). Variants were filtered for genotype quality (> 30), population frequency (< 1% in the gnomAD database) (Karczewski et al., 2020), missense or loss-of-function variants, and variants compatible with autosomal recessive, compound heterozygous, and X-linked modes of inheritance. Additional analyses were conducted to examine: a) all rare variants in genes associated with muscle weakness syndromes, b) all rare variants with Combined Annotation Dependent Depletion (CADD) score > 25 (Rentzsch et al., 2019), and, c) all rare variants in candidate genes from differential diagnoses suggested by the medical records review. All resulting variants were examined for consistency with the proband phenotype, inheritance pattern, predicted pathogenicity, and classification criteria of the American College of Medical Genetics (Richards et al., 2015).

Sanger sequencing validation of genetic variants

Genomic DNA was extracted from saliva (mother and proband) using prepIT-L2P reagent (DNA Genotek) and from blood (unaffected siblings) using the MagAttract HMW DNA kit (Qiagen).

The inheritance pattern of the two *SLC5A7* variants was initially evaluated on a research basis by amplifying with the GoTaq G2 Flexi PCR kit (Promega) using primers spanning the two SLC5A7 variants (chr2:108006188 T>C: TCTTCCTCAGCCACCTATGC and CCCACCATTCCCCAGATGAT; chr2:108008614 G>A: GGCTTCCAGATCCCAAGACT and CCACCAAGATTTTCCAGTGTCA; hg38 coordinates). PCR products were purified using AMPure magnetic beads, followed by Sanger sequencing (Genewiz). CLIA-grade validation of variants and the inheritance pattern for the mother, proband, and an unaffected sibling was performed on blood samples by the Precision Genomics Laboratory at Columbia University.

Reporting of diagnosis and clinical outcomes

The diagnosis was reported to the mother and the treating physician by the Pediatric Undiagnosed Diseases Program. The family was provided a diagnostic report and counseling and was referred to a neurologist and clinical geneticist for clinical follow-up. Clinical outcomes of the proband were obtained from the subsequent medical records and via post-diagnosis interviews and survey of the mother. Quantitative physical performance data was obtained from physical therapy medical records, including two-minute walk test distances, treadmill time, speed, and incline. Physical performance was plotted relative to days after initiation of treatment with pyridostigmine.

Site-directed mutagenesis

The human CHT1-WT cDNA was a gift from Randy Blakely (Addgene, plasmid # 15766) (Apparsundaram et al., 2000) and was cloned into the pLVX-IRES-Hygromycin B (Hyg) vector (Clontech) as described previously (Banerjee et al., 2019). The point mutations 881T>C (I294T) and 1045G>A (D349N) were introduced using the Q5 site-directed mutagenesis kit [New England Biolabs (NEB)]. The mutagenic primers were designed with the NEB Q5 software and

the forward primers are as follows I294T: chr2:108006188 T>C (hg38) c.881T>C (NM_021815.5) 5'–CATTGGGGCCactGGAGCATCAA– 3'. D349N: chr2:108008614 G>A (hg38) c.1045G>A (NM_021815.5) forward primer: 5' –GTCATCAGCAaatTCTTCCATCTTG– 3'. The resulting cDNA was sequenced to confirm the presence of the variant (The Applied Genomics Core, University of Alberta, Edmonton, Canada).

Cell Culture

Human embryonic kidney (HEK) 293 cells (Clontech) were used for a lentiviral production procedure (Clontech). Cells were grown in complete medium [Dulbecco's modified Eagle's Medium (DMEM) (Gibco) supplemented with 10% fetal bovine serum (FBS) (Sigma - Aldrich), 100 units/mL of penicillin and 100 µg/mL of streptomycin (ThermoFisher Scientific)] in 5% CO_2 at 37°C in a humidified incubator until 80% confluency. Next, the cells were transfected with the pLVX-IRES-Hyg plasmid bearing human WT or mutant CHT1 cDNA using a Single Shot packaging kit (Clontech). After 48 hrs, the viral supernatant was collected and passed through a 0.45 µm filter, then supplemented with 8 µg/mL of polybrene (Sigma) and used to infect fresh HEK 293 cells at 90% confluency. Selection of cells stably expressing WT or mutant CHT1 was performed by replacing the viral supernatant after 3 days with complete growth medium containing 0.2 mg/mL hygromycin B (Gibco).

Immunoblot

Confluent HEK 293 cell lines stably expressing mutant CHT1, wild-type CHT1 (positive control line), or empty expression vector (negative control line) were lysed with RIPA lysis buffer (0.3 M NaCl, 20 mM Tris/HCl pH 7.5, 2 mM EDTA, 2% Deoxycholate, 2% Triton X-100, 0.2% SDS, pH 7.4) with protease inhibitors [Complete Mini EDTA-free (Roche)] and phosphatase inhibitors

(PhosSTOP, Roche). A bicinchoninic acid (BCA, Thermo Scientific) assay was performed to determine the total protein concentration in the cell lysates. Twenty μg of lysates were loaded onto 7.5% SDS-PAGE gels and proteins then transferred onto a PVDF membrane (Millipore). The membrane was blocked for 1 hour with skim milk (3% w/v) (BioBasic) in Tris-buffered saline with 0.1% Tween 20 (TBST). Next, it was incubated with anti-CHT1 rabbit polyclonal antibody (1 : 5000 overnight) (Millipore) in TBST containing 1% skim milk, followed by anti-rabbit HRP-conjugated secondary antibody (1 : 10 000 for 1 hour) (GE Healthcare) incubation. Clarity Western chemiluminescent detection reagent (Bio-Rad) was used for detection and visualization performed with the ChemiDoc MP Imaging system (Bio-Rad). Quantification of relative band intensity was performed using the ImageLab software (Bio-Rad). The membrane was then subjected to anti-β–actin HRP antibody (1:10,000) (Biolegend) in TBST containing 1% skim milk, and the bands were visualized as described above.

Cycloheximide chase Experiment

HEK 293 cell lines stably expressing mutant CHT1, wild-type CHT1 (positive control line), or empty expression vector (negative control line) were grown to 90% confluency on poly-L-lysine treated 6-well plates and subsequently treated with 0.3 mg/mL of cycloheximide (Fluka) for 0, 2, 4, 6, 9, and 24 hr. The cells were lysed the following day with RIPA lysis buffer containing protease inhibitors [Complete Mini EDTA-free (Roche)] and phosphatase inhibitors (PhosSTOP Roche**).** A BCA assay was performed, and CHT1 levels were detected via immunoblot as described above.

Rescue Treatments

HEK 293 cell lines stably expressing mutant CHT1, wild-type CHT1 (positive control), or empty expression vector (negative control) were grown to 90% confluency and on poly-L-lysine treated 6-well plates and subsequently treated with Corrector quinazolinone C3 (gift from the Cystic Fibrosis Foundation Therapeutics (Bethesda, MD), VX 908 (SELLECK Chemicals), volume matched DMSO controls for both or 1% DMSO treatment with a volume matched water control for 24 hr. The cells were also treated with MKC231 (MedChemExpress LLC**)** or staurosporine (FroggaBio Inc.**)** and volume-matched DMSO control and a negative control for 23 hrs. The cells were then lysed in RIPA lysis buffer containing protease inhibitors [Complete Mini EDTA-free (Roche)] and phosphatase inhibitors (PhosSTOP, Roche). BCA assay was performed and CHT1 level was detected by immunoblot as described above.

Choline Uptake Assay

HEK 293 cells stably expressing WT-CHT1, mutant CHT1 lines, or empty vector were grown on poly-L-Lysine coated coverslips in 6 well plates until greater than 90% confluency. The cells were washed twice with warm (37°C) Krebs-Ringer-HEPES (KRH) buffer (130 mM NaCl, 1.3 mM KCl, 2.2 mM $CaCl_2.2H_2O$, 1.2 mM $MgSO_4.7H_2O$, 1.2 mM KH_2PO_4, 10 mM HEPES, 10 mM glucose, pH 7.40), then incubated with warm KRH for 10 mins at 37°C. The cells were then incubated with warm KRH containing [^{3}H]-choline (0.1 µM, 100 nCi/ml) at 37°C for 5 min. After 3 washes with cold KRH, they were subsequently lysed using 750 µl of 0.5% Triton. The transport activity was measured using liquid scintillation (Beckman model LS6000IC) and activity was normalized to total protein after by measuring the total protein concentration in each well. Untreated cells from the same seeding date were subject to immunoblot as described above to assess CHT1 expression.

Cell Surface biotinylation

HEK 293 cells stably expressing WT-, CHT1 mutants, or empty vector were seeded on 6 well plates coated with Poly-L-lysine. The cells were subsequently subjected to cell surface biotinylation, as described previously (Banerjee et al., 2016), with minor modifications. Following incubation with membrane impermeant EZ-Link biotinylation reagent (Thermo Scientific, Rockforl, IL) and lysis as described previously, total protein levels were measured. An aliquot of the lysate was saved (total fraction) and 450 µg of each lysate was subsequently incubated with 140 µL streptavidin slurry beads for 1 hour on a rocker at 4°C. Following centrifugation, the supernatant was collected, and an aliquot kept as the unbiotinylated fraction. After washing, the beads were resuspended in 50 µL of 2X Laemmli buffer and incubated at room temperature for 30 min. The eluted biotinylated proteins were subsequently collected by centrifugation (biotinylated fraction). The biotinylated fraction (25 µl) was loaded on SDS-PAGE gel for immunoblot analysis along with 2.5 µg of the total fraction and a matched volume of unbound fraction per well. In addition to CHT1, the blots were probed for cytosolic GAPDH to ensure cell membrane integrity was intact during the biotinylation procedure [mouse monoclonal anti-GAPDH 6C5 (1:10,000); Santa Cruz Biotechnology, Dallas, TX], and for Na^+/K^+-ATPase as loading control [mouse monoclonal anti Na^+/K^+-ATPase H-3 (1:10,000); Santa Cruz Biotechnology, Dallas, TX]. Since the Na^+/K^+-ATPase is present in both the unbound and biotinylated fractions, each fraction was normalized for loading only within that particular fraction.

Statistical Analysis

A one-way ANOVA with Tukey's multiple comparison post hoc test was used to analyze the results of the immunoblots. The half-life experiment was analyzed using a two tailed unpaired t-test. A one-way ANOVA with Dunnett's multiple comparison post hoc test was used to analyze

surface level CHT1 abundance. A one-way ANOVA and Tukey's post hoc test was used to analyze the transport assay results. A 2-way ANOVA was done using Tukey's multiple comparisons test to analyze the rescue experiments and comparisons done within group using 2-way ANOVA and Šídák's multiple comparisons test. GraphPad Prism software was used to represent the data. Statistical significance was attributed to a p value ≤ 0.05.

Results

Clinical Description of the Proband

The proband is an 11-year-old male with hypotonia and global developmental delay. His prenatal and birth history were unremarkable, and he was discharged home on the second day of life. He was admitted to the pediatric intensive care unit (PICU) at 1 week of age for lethargy, poor feeding, decreased weight, and hypothermia, and was discharged home after treatment for presumed sepsis, dehydration, hypernatremia, and hyperbilirubinemia. He was admitted again at 3 weeks of age for respiratory distress, bradycardia and desaturations requiring chest compressions and positive pressure ventilation. He was intubated and transferred to another hospital where he received feeds through a nasogastric tube. Barium esophagram showed severe oral stage dysphagia and delayed swallow. During this hospital course, he failed three extubation attempts. He was transferred to a third hospital at 7-weeks old where he received a tracheostomy, gastrostomy tube for supplemental feeding, and Nissen fundoplication. Physical exam was notable for hypotonia and muscle biopsy showed nonspecific findings of some peri-fascicular atrophy with mild variation in fiber size and hypercontracted fibers. At age 4 months, he was discharged to a pediatric rehabilitation center and then home at age 7 months on continuous positive airway pressure (CPAP) support with tracheostomy collar during sleep.

The proband had several subsequent admissions to the PICU between ages 9 and 24 months due to respiratory deterioration from infections and hypopharyngeal hypotonia. Global

developmental delay was noted during these hospitalizations. He first rolled over at 12 months old. At 13 months old, he was noted to have ophthalmoplegia and decreased muscle bulk and tone. He first socially smiled at 18 months old. At 24 months old, he sat unsupported and spoke his first word. He was weaned off ventilatory support by age 2.5 years, followed by closure of his tracheostomy. At 3 years old, he was able to follow simple commands and use two-word phrases. He continued to receive supplemental feeds via gastrostomy tube until age 3.5 years, when the gastrostomy was closed due to leakage, and he subsequently underwent percutaneous endoscopic gastrostomy (PEG) placement. At 5 years old, he was able to walk and received lower extremity bracing to prevent equinus contracture. He also underwent orchiopexy for bilateral undescended testes. At 6 years old, he discontinued bracing after improvement.

Prior to enrollment into our research program, clinical genetic testing of the proband was nondiagnostic, including karyotype, microarray, *PHOX2B* gene sequence analysis, mitochondrial sequencing, trio whole-exome sequencing, and clinical reanalysis of trio whole-exome sequencing. At 10 years of age, the proband was enrolled into our Pediatric Undiagnosed Diseases Program at the New York University Grossman School of Medicine. At this time, he was able to ambulate independently with bilateral foot pronation and external rotation with tight heel cords. He was able to walk about 80 meters, but tired easily, and he required a wheelchair for longer ambulation with worsening weakness throughout the day. Cognitively, per the mother, he was approximately like a 4-year-old and had some regression of prior skills such as recognizing numbers, letters, and colors. He was not toilet-trained, and he wore diapers. He was in special education with physical, speech, and occupational therapy. His parents are non-consanguineous and family history is non-contributory.

Research genomics analysis identifies p.I294T and p.D349N variants in SLC5A7.

A complete medical history review of the patient suggested that his presentation was consistent with a congenital neuromuscular disease that warranted further genomic analyses. Reanalysis of whole-exome sequencing has a well-documented increase in diagnostic yield (Tan et al., 2020). Therefore, as our initial strategy for identifying a genetic diagnosis, prior clinical whole-exome sequencing data was obtained and reanalyzed.

Research reanalysis of whole-exome sequencing identified compound heterozygous variants in the proband in *SLC5A7***:** Variant **(**1) chr2:108008614G>A (hg38), c.1045G>A (NM_021815.5), p.D349N (NP_068587.1); and Variant (2) chr2:108006188T>C (hg38), c.881T>C (NM_021815.5), p.I294T (NP_068587.1) (**Figure 2.1A**). The father was not available for genotyping. Sanger sequencing confirmed variant 1 was absent in the mother but present in a heterozygous state in a healthy brother, while variant 2 was present in a heterozygous state in the mother but absent in the healthy brother, thereby confirming that the proband was compound heterozygous for the two variants. Variant 1 has a CADD score of 29.6 and is absolutely conserved across vertebrates (Rentzsch et al., 2019). Variant 2 has a CADD score of 22.5 and is conserved across vertebrates with the exception of a few species. Both variants are absent in gnomAD (Karczewski et al., 2020).

Heterologous p.D349N CHT1 is more abundant than WT CHT1 while p.I294T CHT1 is significantly less abundant than WT CHT1 protein in HEK 293 cells.

Although the proband is a compound heterozygote, each mutant was characterized separately to determine the mechanism by which each mutant may lead to alteration of function. HEK 293 cells (that do not express detectable CHT1 endogenously) stably expressing p.I294T, p.D349N or WT CHT1 proteins were generated, and cell lysates prepared to assess protein abundance in this cell

model. As shown in **Figures 2.1 B & C**, in comparison to WT CHT1, p.I294T mutant abundance was reduced to 36.1 ± 1.5% of WT CHT1 (n = 4, ± SEM), while p.D349N abundance was 135.5 ± 1.5% (n = 4, ± SEM) of WT CHT1 protein level. The migration profile of WT CHT1 shows an abundant upper band corresponding to complex glycosylated protein (~60 kDa) and a lower broad band (~48 kDa) corresponding to core glycosylated and non-glycosylated protein, as previously described (Banerjee et al., 2019). The reduced abundance of p.I294T CHT1 mutant could originate from increased protein degradation, or reduced protein synthesis so we next assessed p.I294T CHT1 mutant degradation rate.

p.I294T has a shorter half-life compared to WT.

To address whether p.I294T CHT1 mutant has a shorter half-life, we incubated HEK 293 cells stably expressing this mutant with cycloheximide for 0, 2, 4, 6, 9 or 24 hours and lysates were subsequently subject to immunoblot using rabbit polyclonal CHT1 antibody. As shown in **Figures 2.1 D & E**, p.I294T CHT1 mutant had a significantly reduced half-life compared with WT CHT1. While WT CHT1 had a half-life of 23 hours, the p.I294T CHT1 mutant had a half-life of 7 hours. Immunofluorescence analysis showed a uniform layer of low fluorescent cells rather than a few high expressing cells, supporting that the viral infection was successful and uniform but resulted in low CHT1-expressing cells (**Figure 5.1, Appendix A**). Although we did not assess the rate of protein synthesis, this result indicates that the decreased abundance of p.I294T CHT1 mutant is at least in part due to rapid degradation compared to WT CHT1 protein. Given the high abundance of p.D349N CHT1 mutant, its half-life was not examined.

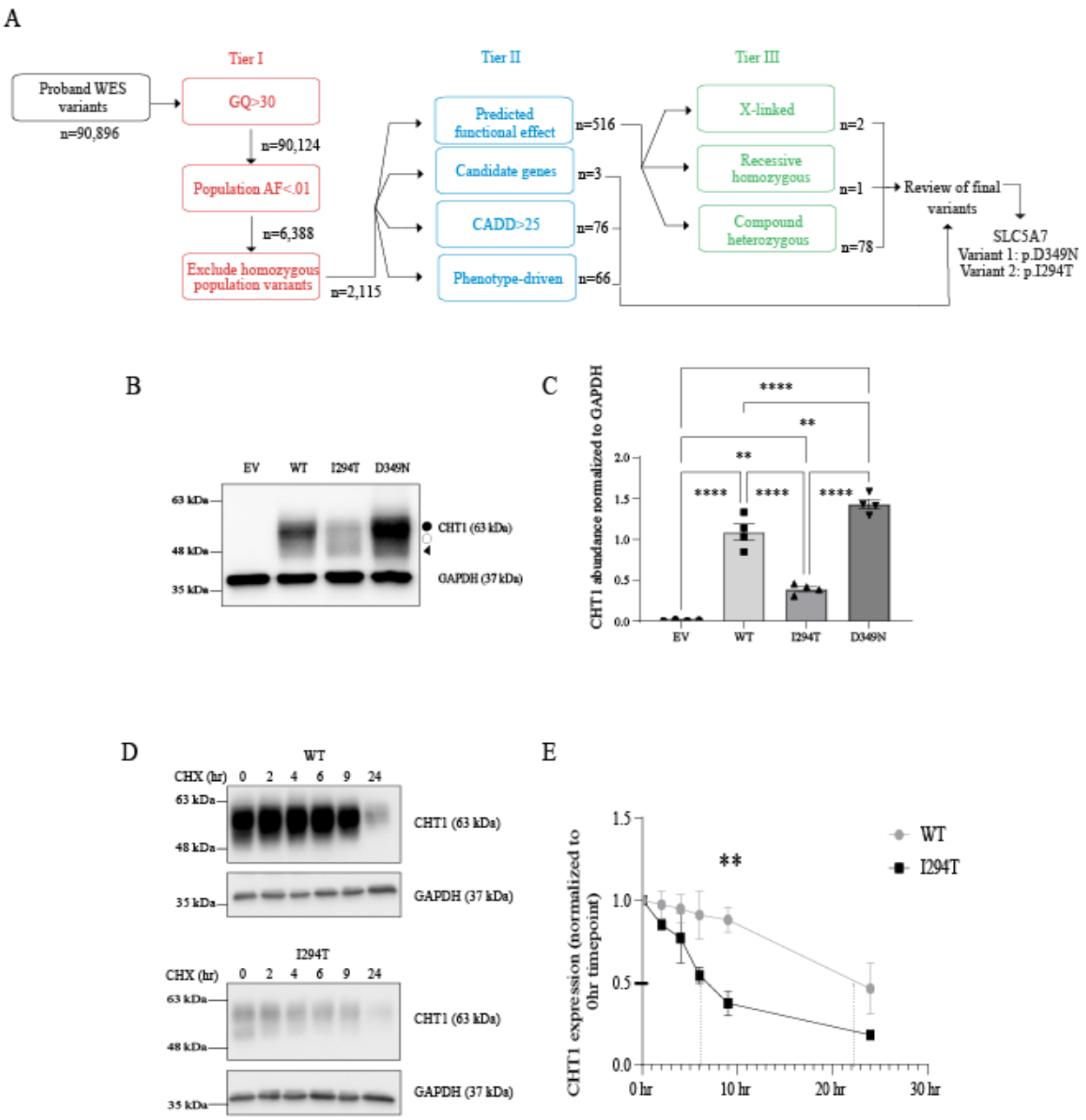

Figure 2.1. Identification of CHT1 mutations, and WT and mutant CHT1 abundance and half-life**. (A)** Proband whole-exome sequencing (WES) variants were analyzed with three tiers of filters: Tier I (genotype quality and population frequency), Tier II (predicted pathogenicity and phenotype-driven filtering), and Tier III (inheritance mode). Phenotype-driven filtering was performed using Qiagen's biological context algorithm which ranked correlation of genes to human phenotype ontology (HPO) terms derived from medical chart review. This approach

produced a set of candidate variants, of which only the compound heterozygous *SLC5A7* variants matched the patient's phenotype. Additional exploratory analyses with less stringent filters did not identify additional candidate variants. n=number of variants after each filtration step; GQ=genotype quality; AF=allele frequency. **(B)** Representatives immunoblot from HEK 293 cells stably expressing WT, p.I294T or p.D349N CHT1 mutants or empty vector (EV). Black circles indicate CHT1 carrying complex oligosaccharides, white circle shows core glycosylated CHT1 and triangles show unglycosylated CHT1. **(C)** Quantification of CHT1 abundance in EV, WT, p.I294T or p.D349N CHT1 mutants. Error bars correspond to mean ± SEM, n=4. **P < 0.01, ****P < 0.0001 using one-way ANOVA with Tukey's multiple comparison post hoc test. **(D)** Representative immunoblot of WT and p.I294T CHT1 expressing cells treated with cycloheximide. Error bars correspond to mean ± SEM, n=3. **P < 0.01 using two tailed unpaired t-test ANOVA. CHX, cycloheximide. (E) Quantification of WT and p.I294T CHT1 abundance after treatment with cycloheximide. Error bars correspond to mean ± SEM, n=4. **P < 0.01 using one-way ANOVA with Tukey's multiple comparison post hoc test.

The proportion of p.I294T and p.D349N mutants reaching the plasma membrane is similar to WT CHT1

The reduced half-life of p.I294T CHT1 mutant may translate into a decreased abundance of the protein at the cell surface. To assess this, we conducted cell surface biotinylation assays in cells expressing WT CHT1, p.I294T CHT1 or p.D349N CHT1. As shown in **Figure 2.2**, despite reduced overall abundance, the proportion of cell surface p.I294T CHT1 mutant is similar to WT CHT1, when normalized to total protein abundance (86.3 ± 40.6% for p.I294T CHT1 and 126.1 ± 40.1% for p.D349N CHT1 (n=4, mean ± SEM). This result demonstrates that although less total protein is present in these cells, the remaining protein is translocated to the plasma membrane in the same proportion as WT CHT1, indicating normal processing to its final destination in the cell membrane. Furthermore, the fraction of unbiotinylated CHT1 is comparable between WT, p.I294T and p.D349N. Thus, the p.D349N CHT1 mutant reached the cell surface in a similar proportion to WT CHT1 when normalized to total CHT1 protein abundance. These results suggest mistrafficking of either mutant is not a likely cause of the disease.

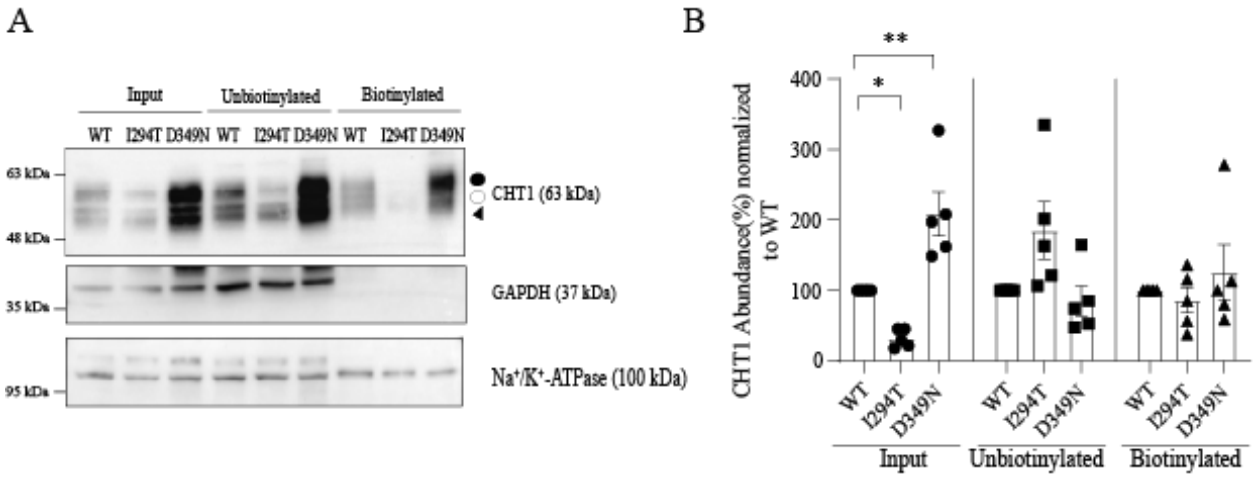

Figure 2.2. Cell surface abundance of WT, p.I294T, or p.D349N CHT1 in HEK 293 stable cell lines. Cell surface biotinylation was performed as described in Methods. **(A)** Representatives immunoblot of total (input), unbiotinylated and biotinylated fractions isolated from HEK 293 cells stably expressing WT, p.I294T, or p.D349N CHT1. Black circle indicates CHT1 carrying complex oligosaccharides, the white circle shows core glycosylated CHT1, arrowhead indicates unglycosylated CHT1. **(B)** Quantification of the total (input), unbiotinylated or biotinylated fraction of WT or p.I294T CHT1. Error bars correspond to mean ± SEM, n=5. *P < 0.05, **P < 0.01 using one-way ANOVA with Dunnett's multiple comparison post hoc test.

p.D349N CHT1 transport is inactive while p.I294T CHT1 transport is partially active

Given that both p.I294T CHT1 and p.D349N CHT1 mutants reach the cell surface at similar proportions to WT CHT1, we next assessed their transport activity. We measured the transport rate of 0.1, 2.5 and 10 μM tritiated choline over 5 minutes in HEK 293 cells expressing empty vector, WT or mutant CHT1 proteins. **Figure 2.3 A** shows that compared to WT CHT1, the transport activity of the highly abundant p.D349N CHT1 mutant is comparable to HEK 293 cells expressing the empty vector, which is significantly lower than WT CHT1. This result indicates that the p.D349N substitution results in a non-functional protein, potentially through interference with binding or release of choline, protein misfolding (without triggering premature protein degradation) or blocking the transporter in an inactive state. Interestingly, the p.I294T CHT1 mutant shows 49.5 ± 1.7% (n = 3, mean ± SEM) residual transport function compared to WT CHT1 when cells are incubated with 0.1 μM tritiated choline. However, the significant difference compared to empty vector expressing cells is abolished with 2.5 and 10 μM tritiated choline. Correction for CHT1 abundance makes I294T function similar to WT (**Figure 2.3B**). This suggests that I294T, while lower in total abundance, retains some activity. Notably, this residual activity may explain the less severe phenotype observed in the patient and raises the possibility that this mutant may support more choline transport activity if rescued from premature degradation.

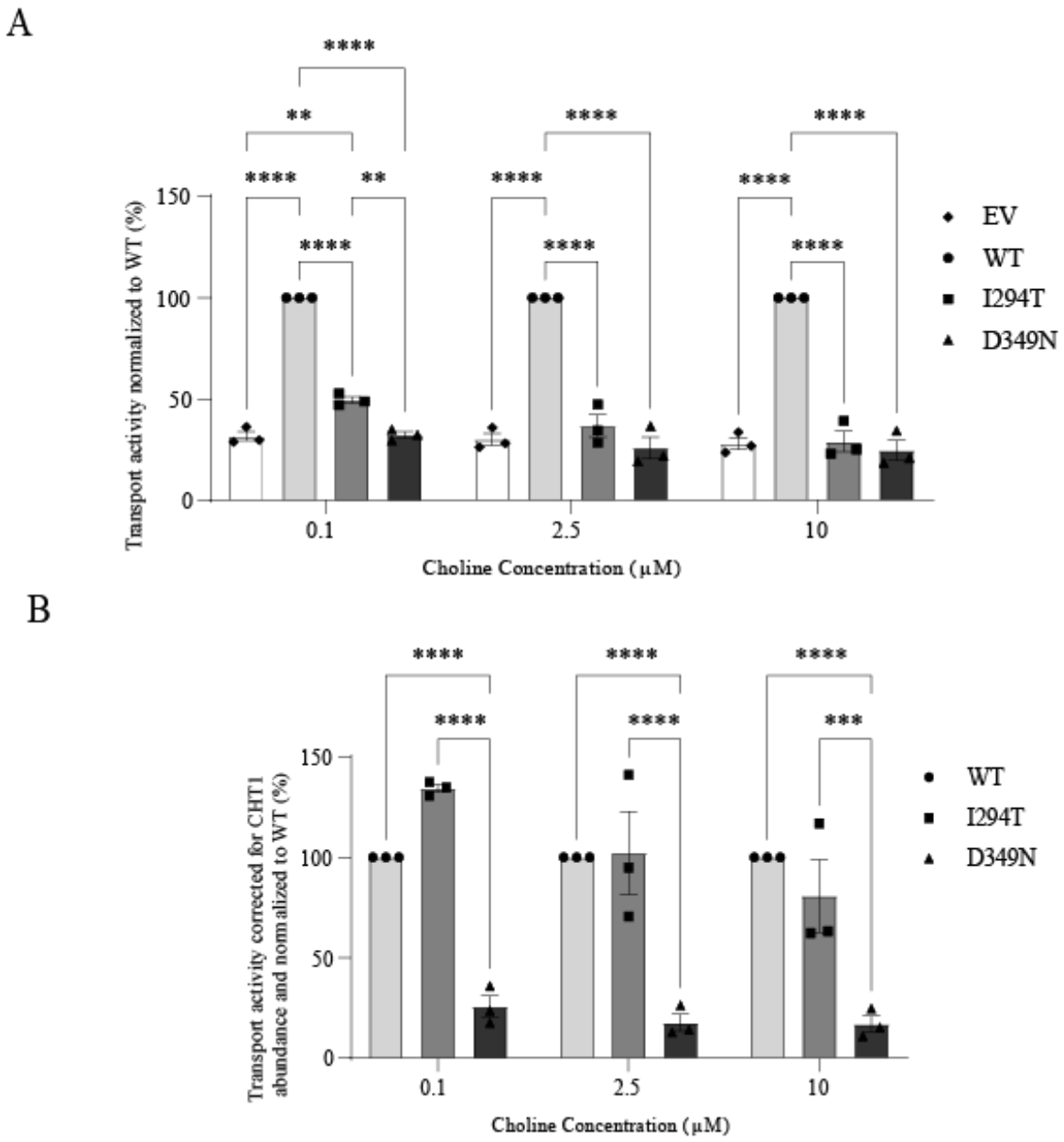

Figure 2.3. Transport of [^{3}H]-choline by HEK 293 cells stably expressing WT, p.I294T or p.D349N CHT1 or empty vector (EV) at a single time point of 5 mins at multiple choline concentrations (0.1, 2.5 and 10 µM), either (A) uncorrected or (B) corrected for CHT1 protein level. Values are shown as percentage of WT transport activity. Error bars correspond to mean ± SEM, n=4. **P < 0.01, ****P < 0.0001 using one-way ANOVA with Tukey's multiple comparison post hoc test.

Staurosporine partially rescues p.I294T CHT1 mutant processing

Given the partial transport activity observed for the p.I294T CHT1 mutant, we wondered whether chemical chaperones that rescue cystic fibrosis transmembrane conductance regulator (CFTR) mutant proteins (VX 809 (Van Goor et al., 2011) and C3 (Peters et al., 1996; Van Goor et al., 2006)) or that activate CHT1 (MKC 231 (Takashina et al., 2008) and staurosporine (Choudhary et al., 2017)) would rescue p.I294T CHT1 mutant abundance and activity. HEK 293 cells stably expressing WT or p.I294T CHT1 mutants were incubated with VX 809 (2 or 5 μM), 1% DMSO, C3 (5 or 10 μM), MKC231 (1 or 10 μM) or 5 μM staurosporine for 24 hours prior to immunoblotting. None of the treatments improved p.I294T CHT1 mutant abundance except for the staurosporine treatment that significantly increased the glycosylated/total CHT1 ratio of the mutant from 0.51 ± 0.07 to 0.88 ± 0.08 (n =3, mean ± SEM) (**Figure 2.4**). An increased glycosylation ratio may correlate with increased trafficking to the cell surface and rescue transport activity, motivating future development of drugs that increase proper cellular processing of CHT1 mutants with residual transporter function.

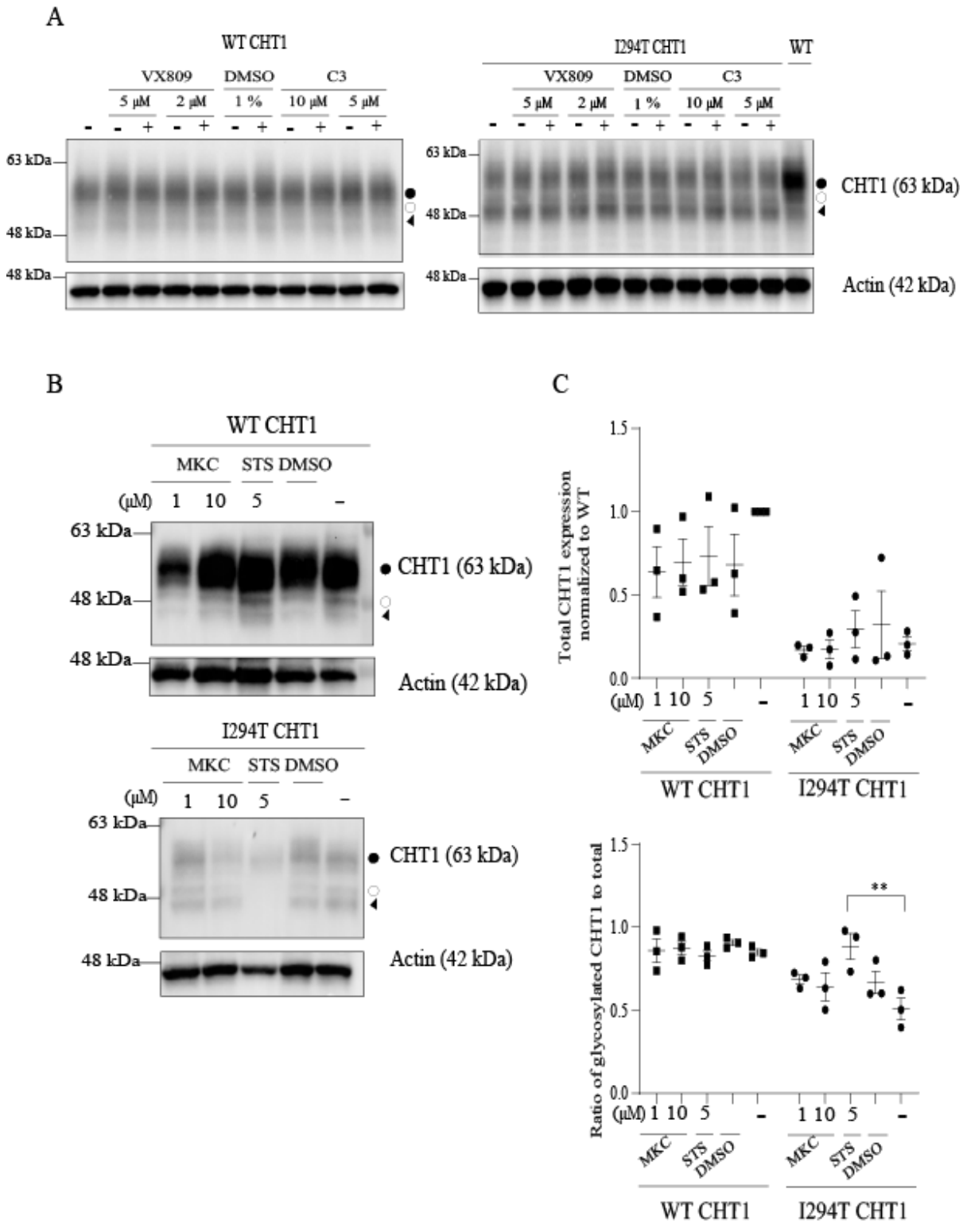
A
WT CHT1
VX809
DMSO
C3
5 μM
2 μM
1 %
10 μM
5 μM
63 kDa
48 kDa
48 kDa
I294T CHT1
WT
CHT1 (63 kDa)
Actin (42 kDa)
B
WT CHT1
MKC
STS
DMSO
(μM) 1 10 5 –
63 kDa
48 kDa
48 kDa
CHT1 (63 kDa)
Actin (42 kDa)
I294T CHT1
C
Total CHT1 expression normalized to WT
1.5
1.0
0.5
0.0
WT CHT1
I294T CHT1
Ratio of glycosylated CHT1 to total
**

Figure 2.4. Chemical chaperone treatments of WT or p.I294T CHT1 stably expressing cells. **(A)** HEK 293 cells stably expressing WT (left panel) or p.I294T (right panel) CHT1 were treated with VX809 (vehicle DMSO or 5 μM), DMSO (none or 1%), or C3 (vehicle DMSO or 5 μM) for 24 hours prior to lysis and immunoblotting. Black circles indicate CHT1 carrying complex oligosaccharides, the white circles indicate core glycosylated CHT1, arrowhead indicates unglycosylated CHT1. **(B)** HEK 293 cells stably expressing WT (left panel) or p.I294T (right panel) CHT1 mutant were untreated ("-"), treated with MKC231 (MKC, 1 or 10 μM), staurosporine (STS, 5 μM), or volume matched DMSO control for 24 hours prior to lysis and immunoblotting. "-" indicates volume matched vehicle control (water for DMSO treatment), n=4. Black circle indicates CHT1 carrying complex oligosaccharides, the white circle shows core glycosylated CHT1, arrowhead indicates unglycosylated CHT1. **(C)** *(top panel)* Quantification of total CHT1 abundance for WT and p.I294T under the indicated treatment conditions. *(bottom panel)* Quantification of the ratio of glycosylated to total CHT1 protein for WT and p.I294T CHT1 expressing cells under the indicated treatment conditions. Error bars correspond to mean ± SEM, n=3. **$P < 0.01$ using a two-way ANOVA with Tukey's multiple comparison post hoc (top panel) or Sidak's multiple comparison post hoc (bottom panel) test.

Treatment with acetylcholinesterase inhibitor and physical and occupational therapy significantly improved the proband's symptoms and quality of life

The diagnosis of *SLC5A7*-related CMS was reported to the family, referring neurologist, and geneticist. Given the diagnosis of *SLC5A7*-related CMS, the proband was prescribed the acetylcholinesterase inhibitor Pyridostigmine (30 mg, 3 times daily) and additional physical and occupational therapies. Treatment resulted in improved locomotion, strength, and endurance as shown by increasingly achieved distances in standardized two-minute walk tests, and total time, speed, and incline on a treadmill (**Figure 2.5**). Subjective reports from his mother also stated that he was able to walk longer distances in single excursions (from 80 to 250 meters), and to run and eat dry food, which he was unable to previously perform.

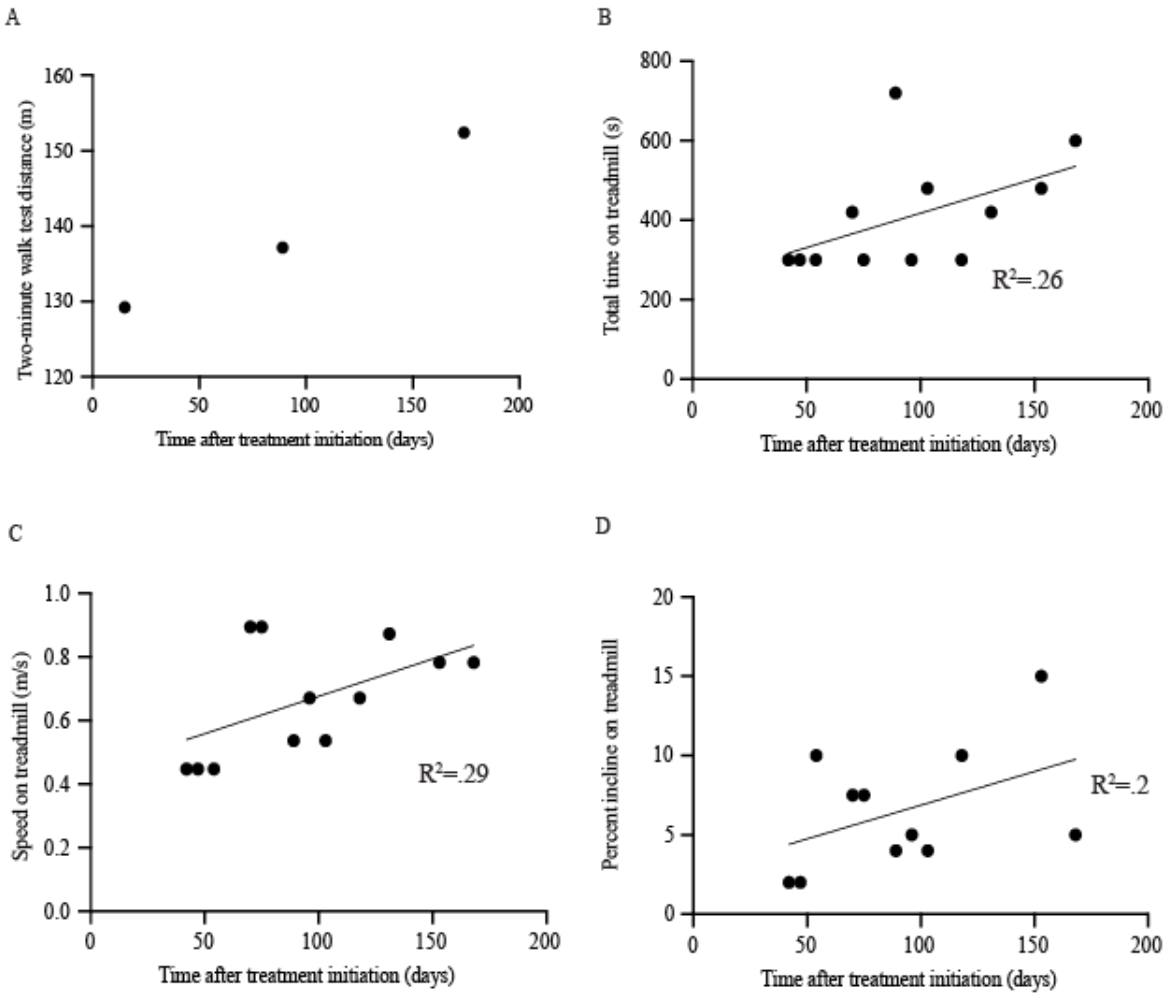

Figure 2.5. Physical therapy endurance measurements after initiation of treatment**.** After diagnosis, the proband was initiated on pyridostigimine (30 mg, three times per day) and additional physical therapy sessions (once per week). (A) Two-minute walk test distances. The two-minute walk test is a standardized assessment of endurance that measures total distance after two minutes of walking through a 15.2 m out-and-back course. Distances were recorded over three sessions. (B-D) The proband performed an endurance exercise by walking on a treadmill over the course of 12 physical therapy sessions. (B) Total time on treadmill. (C) Speed on treadmill. (D) Percent incline on treadmill. Percent incline is calculated from the ratio of vertical to horizontal distance on the treadmill. Linear regressions with R^2 values (square of Pearson

correlation coefficient) are shown, except for two-minute walk test distance (panel A) for which there are too few measurements.

Discussion

Here, we report a proband with novel compound heterozygous mutations in CHT1, p.I294T and p.D349N, that result in a non-lethal CMS. Using biochemical assays, we show that in HEK 293 cells, the p.I294T CHT1 mutant is less abundant than CHT1 WT but retains some cell surface localization and transport function at low choline concentrations. On the other hand, the p.D349N CHT1 mutant is more abundant than WT CHT1 and retains cell surface localization but is inactive at any concentration of choline tested. Only staurosporine improved p.I294T CHT1 processing, resulting in an increased fraction of CHT1 carrying complex glycosylation. However, this treatment caused cell death and could not be tested on mutant transport function. As a result of this genetic diagnosis and biochemical characterization, the proband was treated with an acetylcholinesterase inhibitor, and his symptoms improved.

Five studies to date have correlated *SLC5A7* mutations with neuromuscular junction defects. Wang and colleagues described three homozygous mutations in *SLC5A7* in three families, including highly conserved p.S94R and p.V112E, and p.P210L mutations (Wang et al., 2017). The phenotypes varied from the classical presentation of CMS (P210L) who responded to AChEIs, to generalized neurodevelopmental delay coupled with brain atrophy (S94R) and infantile lethality (V112E), who did not respond to an AChEI. Wang and colleagues hypothesized that aberrant protein trafficking and localization lead to these phenotypes by *in vitro* studies. Pardal-Fernández and colleagues next described a compound heterozygous infant with acute respiratory failure, generalized weakness and severe hypotonia who carried compound heterozygous mutations in *SLC5A7*, and they proposed that the phenotype was due to low levels of ACh released into the synapse leading to aberrant muscle fibre potentials (Pardal-Fernández et al., 2018). In that case, AChEIs improved the patient's condition but only for a short period of time because the impaired

presynaptic CHT1 is not dependent on the choline gradient (Pardal-Fernández et al., 2018; Wang et al., 2017). Additionally, Bauche and colleagues described 11 recessive *SLC5A7* mutations in 6 unrelated families clinically ranging from CMS with episodic apnea to a lethal prenatal type of arthrogryposis (Bauché et al., 2016). Finally, three novel homozygous mutations (p.R107H, p.A296T, and p.Y414N) resulted in presynaptic CMS and in varying degrees of weakness, including fatality, and varying responses to AChEIs ranging from improvements in gross motor development and dysphagia (R107H and A296T) to no response (Y414N) (Rodríguez Cruz et al., 2021). Rodriguez Cruz et al. proposed that response to treatment corresponds to presenting phenotypes and residual activity of CHT1. Notably, our patient has had sustained improvement in motor strength at least over a 6-month follow-up period, consistent with residual function of the I294T mutant in our biochemical assay. Therefore, genotype-phenotype correlations and biochemical characterization of CHT1 mutations may help guide treatment management in CHT1-related CMS.

Our group previously identified a recessive p.S263F mutation in *SLC5A7* in two siblings of El Salvadoran descent (Banerjee et al., 2019). This amino acid substitution manifested with electromyography suggestive of CMS, arthrogryposis, and reduced prenatal movements. Both siblings were withdrawn from intensive care a few months after birth. Characterization of the mutation *in vitro* showed that the substitution resulted in a complete loss of function, explaining the severe phenotype of the homozygous patient.

A structure for human CHT1 has not been published yet. According to the predicted structure of human CHT1 with Alphafold (https://alphafold.ebi.ac.uk/entry/Q9GZV3) (Jumper et al., 2021; Varadi et al., 2022), D349 is buried within transmembrane helix 9 at the center of the transmembrane helices bundle (**Figure 2.6 A & B**), and its carboxyl group interacts with S350 and

Y175. Substituting D349 to N would likely impair one of these interactions and may explain the lack of activity in the CHT1 D349N variant, which was not rescued by increasing the choline concentration. Furthermore, D349 is highly conserved across vertebrates, highlighting the likely importance of this specific residue.

The I294T mutant results in the introduction of a polar uncharged group. According to the Alphafold predicted structure of human CHT1, this highly conserved residue is located at the extracellular end of transmembrane domain 8 in proximity to A206, L207, and V212 (**Figure 2.6 C & D**). Substitution to a polar uncharged residue may disrupt these interactions and cause inappropriate recognition by the protein quality-control machinery, leading to premature degradation of the protein. Surprisingly, in HEK cells stably expressing CHT1 I294T, at 0.1 μM choline, residual transport function was observed, but at higher choline concentrations, no function was detected. Although it is unclear why transport activity was abolished at high choline concentrations, this finding suggests that this substitution does not cause a dramatic misfolding with complete loss of function, in line with the milder phenotype of this patient compared to lethal CMS conditions caused by transport dead mutants.

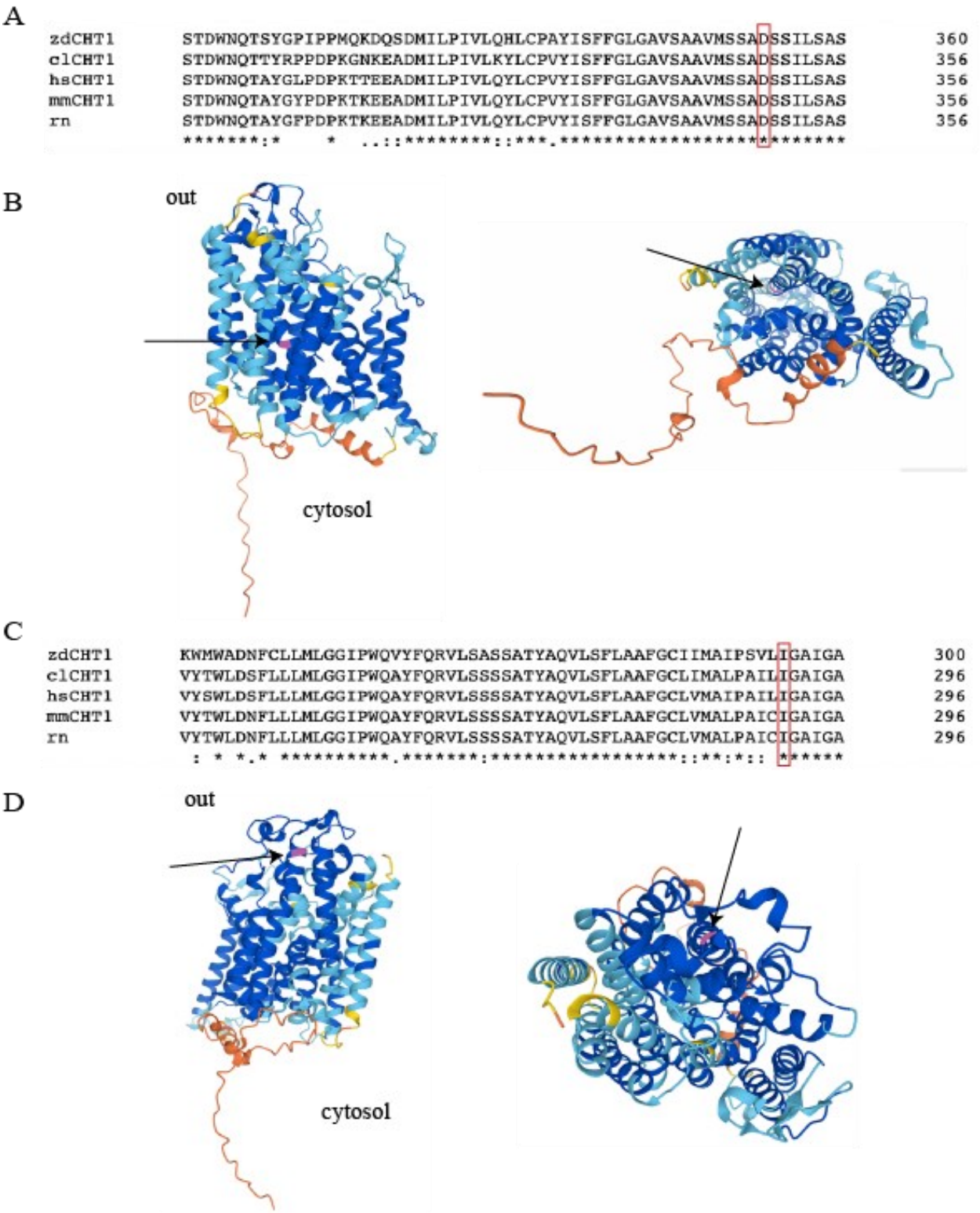

Figure 2.6: Alignment and location of D349 or I294 on CHT1 structure predicted by AlphaFold**.**

(A) Alignment of the choline transporter primary sequence from various species, highlighting the

location of D349 (red rectangle). **(B)** Predicted human CHT1 structure using AlphaFold highlighting the position of D349 (pink) (arrow) buried at the center of the transmembrane domain. Left panel shows the sideview and right panel shows the cytosolic view of the protein with D349 shown in pink (arrow). **(C)** Alignment of the choline transporter primary sequence from various species, highlighting the location of I294 (red rectangle). **(D)** Predicted human CHT1 structure using AlphaFold highlighting the position of I294 (pink) at the extracellular side of transmembrane helix 8 (arrow). Left panel shows a side view and right panel shows the extracellular view of the protein with I294 shown in pink (arrow).

Dietary choline is essential, and choline synthesis does not occur in cholinergic neurons, which is why high affinity choline uptake (HACU) via CHT1 is required for most cholinergic neurotransmission. HACU is limited to cholinergic nerve terminals where the choline concentration is low because it is converted to ACh (Haga & Noda, 1973; Kuhar et al., 1973), whereas the ubiquitous CHT1/Na^+-independent transport occurs where the choline concentration is high. Approximately 60% of the choline that is taken up by the cell via HACU is converted to ACh (Haga & Noda, 1973), whereas only a small amount of choline transported by the Na^+-independent pathway is used to synthesize ACh (Lockman & Allen, 2002). Therefore, HACU is necessary for ACh synthesis, and this is evident in mouse CHT1 knockout models that have a lethal phenotype (Bazalakova & Blakely, 2006; English et al., 2010; Ferguson et al., 2004a; Matthies et al., 2006). Since the proband has a reduced but residual capacity for choline uptake, increasing the concentration of ACh in the synapse via a cholinesterase inhibitor seems to be an appropriate intervention to help improve symptoms, which was subsequently demonstrated clinically.

In summary, we report here a child with CMS carrying newly identified compound heterozygous p.I294T and p.D349N CHT1 mutations. *In vitro* characterizations suggest two mechanisms by which these mutations lead to loss of CHT1 function. Based on these findings, the child was treated with an acetylcholinesterase inhibitor that significantly improved the patient's condition. This study highlights the benefits of bedside to bench to bedside approaches for rare diseases, and the clinical applicability of genotype-phenotype correlations.

Chapter 3 : The link between Mutant kAE1 and Autophagic cell death in Distal Renal Tubular Acidosis

Introduction

Distal renal tubular acidosis (dRTA) is characterized by metabolic acidosis, hypercalciuria, nephrocalcinosis, hypokalemia, hyperchloremia, decreased bone density, difficulty thriving and eventually chronic kidney disease (CKD)(Karet et al., 1998b; Norgett et al., 2012b; Stover et al., 2002b; Yaxley & Pirrone, 2016a). Inherited forms of dRTA in humans are either caused by mutations in *SLC4A1* which encodes kAE1 (band 3), or *ATP6V1B1*, *ATP6V0A4, ATP6V1C2* which encode for three subunits of the vacuolar H^+-ATPase (v-H^+-ATPase). dRTA is specific to the connecting tubule and collecting duct (CD) where A-IC cells are located(Finberg et al., 2005; Karet et al., 1998a; Mumtaz et al., 2017; Norgett et al., 2012a; Stover et al., 2002a; Yaxley & Pirrone, 2016b). The CD is composed of at least 3 cell types including principal cells (PC), and type A and type B intercalated cells (A-IC and B-IC) which are important for acid-base homeostasis. PC contributes to sodium and water reabsorption, A-ICs acidify the urine using the basolateral kAE1 and the v-H^+-ATPase on the apical membrane. B-IC reabsorb protons and salts and secrete HCO_3^-(Roy et al., 2015).

The Ae1 R607H mouse model of dRTA (equivalent to the R589H dominant mutation in humans) have fewer A-ICs and in the remaining A-ICs, the v-H^+-ATPase is less abundant at the apical membrane compared to WT mice (Mumtaz et al., 2017). Interestingly, an accumulation of p62 and ubiquitin positive material in the remaining A-ICs was also observed. It was hypothesized that the Ae1 R607H variant may disrupt the normal trafficking of the v-H^+-ATPase and alter lysosomal function, resulting in defective autophagy and cell death (Mumtaz et al., 2017).

Macroautophagy which will be hereafter referred to as autophagy, is a cellular process which recycles proteins and organelles in times of stress(Mizushima & Komatsu, 2011). It is inhibited by the nutrient sensor called mammalian target of rapamycin 1 complex (mTORC1) which is found on the lysosomal membrane. When active, mTORC1 phosphorylates several downstream effectors

including 4E-BP1 (inhibitory) and p70S6K (stimulatory) which eventually leads to the suppression of autophagy(Medicine, 2017). mTORC1 regulation is key to autophagy and pH can also regulate mTORC1 (Balgi et al., 2011; Kazyken et al., 2021).

Balgi et al., found that acidic pH activates mTORC1(Balgi et al., 2011). Whereas alkaline pH activates mTORC2 in addition to mTORC1, which displays an additive effect in the presence of alkaline pH(Kazyken et al., 2021). This means that alkaline pH increases mTOR activity which in turn would result in decreased autophagy and promote cell survival, which is what occurs in cancer cells(Reshkin et al., 2000; White et al., 2017). However, uncontrolled autophagy can also lead to death in normal cells (Kang & Avery, 2008) which is what might be happening in DRTA cells.

Besides mTORC1 regulation, the formation and maturation of the autophagosome is another key process to autophagy. Upon autophagy activation, cytosolic LC3BI undergoes conjugation with phosphatidylethanolamine to form LC3BII, which results in autophagosome maturation(Kabeya et al., 2000). Additionally, p62 links ubiquitinated proteins to the autophagosome which results in their degradation(Liu et al., 2016). Furthermore, activation of mTORC1 results in the downstream inhibitory phosphorylation of 4E-BP1 at S65, which is a marker of decreased autophagy (Gingras et al., 1998). Thus, an increase in phosphorylation of 4E-BP1 indicates a decrease in autophagy. 4E-BP1 inhibits elongation initiation factor 4E (eIF4E) by binding to it(Pause et al., 1994).

As the expression of the chloride/bicarbonate exchanger kAE1 alters cytosolic pH and since mTORC1 activity is sensitive to cytosolic pH, we hypothesized that dRTA mutant expression triggers a change in cytoplasmic pH, resulting in uncontrolled autophagy possibly leading to A-IC loss by premature cell death.

Materials and Methods

Constructs and Cell culture

Human kAE1 WT-HA cDNA construct (carrying a hemagglutinin HA epitope in position 557) was generated and characterized previously (Lashhab, 2021). p.R295H, p.S525F mutations were identified in patients with recessive (p.R295H) and dominant (p.S525F) dRTA (Unpublished data, personal communication from Dr. Rosa Vargas-Poussou, Georges Pompidou Hospital, Paris). The autosomal dominant p.R589H mutation has been described previously (Jarolim P, JBC, 1998). The corresponding mutations were generated by site directed mutagenesis (Q5 site directed mutagenesis kit, NEB) into inducible pLVX-TRE3G lentiviral expression vector and the construct introduced into mouse inner medullary collecting duct (mIMCD3) cells (ATCC, CRL-2123). mIMCD3 cells carrying kAE1 WT-HA, kAE1 R295H-HA, kAE1 S525F-HA and kAE1 R589H-HA Lenti-X 293T cells (Clontech) were transfected with 7 μg of pLVX-Tet3G regulator plasmid, and either pLVX-TRE3G kAE1 WT-HA (kAE1), pLVX-TRE3G kAE1 R295H-HA, pLVX-TRE3G kAE1 S525F-HA, or pLVX-TRE3G kAE1 R589H-HA expression plasmids using Xfect Transfection Reagent and Lenti-X HTX Packaging mix (Clontech). Cells were incubated in serum-free OptiMEM medium (Gibco) for 48 hours at 37ºC and then the supernatants containing the lentivirus were filtered through 0.45 μm filters. 70% confluent mIMCD3 were then co-infected with lentiviruses from the filtered supernatants, in presence of 8 μg/ml of polybrene (Sigma-Aldrich, USA) for 48 hours. Cells were cultured in complete Dulbecco's Modified Eagle's Medium-F12 (DMEM-F12) (Gibco), 10% Fetal Bovine Serum (FBS) (Gibco) and 1% penicillin-streptomycin (HyClone) supplemented with 4 μg/ml Puromycin (Gibco) and 2 mg/ml G418 (FroggaBio) for selection. All culture was done at 37ºC in 5% CO_2. Incubation with 1μg/ml of doxycycline (Sigma-Aldrich) for 48 hours induced kAE1 expression (Lashhab, 2021).

Cell treatments and Immunoblot

Cells expressing kAE1 WT-HA or variants were grown on 10 cm dishes until 70% confluency and then treated with dox for 48 hours. For autophagy experiments, the cells were then either treated with 400 nM bafilomycin A1 (baf) for 4 hours to block autophagy or Hanks Balanced Salt Solution (HBSS, Gibco) for 2 hours to induce autophagy, or no treatment before lysis. Cells were lysed with RIPA lysis buffer (1% deoxycholate, 1mM EDTA, 0.15 M NaCl, 0.1% SDS, 10 mM TRIS/HCL (pH 7.5), 1% Triton X-100) with phosphatase inhibitors (cat. no. 04906837001; Roche PhosSTOP) and protease inhibitors (cat. no. 04693159001; Roche Complete Tablets, Mini EDTA-free), and stored at −20 °C with or without 2x Laemmli buffer. The aliquot without Laemmli buffer was used for a bicichonic acid (BCA) assay to determine protein concentration. 20 μg of the samples were run on 8, 10 or 12% SDS-PAGE gels at 200 V for 45 min and then transferred onto PVDF membranes at 100 V for 1.5 hours. The blots were blocked with 3% skim milk in tris buffered saline with tween (TBST) for 1 hour at room temperature. The primary and secondary antibodies used to study autophagy are summarized in Table **3.1.** Clarity Western chemiluminescent detection reagent (Bio-Rad) was used for detection and visualization was done using the ChemiDoc MP Imaging system (BioRad). ImageLab freeware (Bio-Rad) was used to quantify the relative band intensities and results analyzed using a one-way ANOVA with a Dunnett or Tukey's multiple comparison test. P-value of 0.05 or less was considered significant.

Table 3.1. Antibody conditions used in Western blot experiments. Hour (hr), and room temperature (RT).

Antibody	Species	Incubation Conditions	Solution	Ideal Dilution (Secondary in brackets (if not 1/10000))	Manufacture	Band size (kDa)
Actin-HRP conjugated	Mouse	1 hr RT	1% Milk + TBST	1/10000	BioLegend	43
LC3B	Rabbit	O/N 4°C	1% Milk + TBST	1/1000	Cell Signaling	14-16
HA (kAE1)	Rat	O/N 4°C	1% Milk + TBST	1/1000	Roche	96
P mTOR (Ser 2448)	Rabbit	O/N 4°C	1% Milk + TBST	1/1000 (1/2500)	Cell Signaling	289
mTOR	Rabbit	O/N 4°C	1% Milk + TBST	1/1000 (1/2500)	Cell Signaling	289
P 4E-BP1 (Ser65)	Rabbit	1 hr RT (better O/N 4°C)	1% Milk + TBST	1/750 (1/2500)	Cell Signaling	16-20
4E-BP1	Rabbit	1 hr RT (better O/N 4°C)	1% Milk + TBST	1/1000	Cell Signaling	16-20
p62	Mouse	O/N 4°C	1% Milk + TBST	1/5000	Abcam	62
p53	Mouse	O/N 4°C	1% Milk + TBST	1/5000	Cell Signalling	53
Cleaved caspase 3	Rabbit	O/N 4°C	1% Milk + TBST	1/1000	Cell Signalling	19

Magic Red Staining and Immunofluorescence

To assess lysosomal function using fluorescent Magic red substrate, mIMCD3 cells expressing kAE1 WT-HA or variants were grown on glass coverslips until 80% confluency and kAE1 expression was induced with dox for 48hrs. The cells were either treated with 400nM bafA1for 4 hours to block autophagy, HBSS (Gibco) without FBS for 2 hours to induce autophagy, or no treatment before they were subject to 1% Magic Red (ImmunoChemistry) in DMEM-F12 medium at 37 °C in the dark for 30-60 mins. The remainder of the treatments were done in darkness and at room temperature. The cells were fixed with 4% PFA for 15 mins followed by autofluorescence quenching with 100 mM glycine for 5 min. The cells were permeabilized with 0.1-0.2% Triton X-100 for 15 mins, blocked with 1% BSA for 30 min and incubated with mouse anti-HA primary antibodies (1/500 in 1% BSA) (Abcam) for 30 min and then Alexa Fluor 488 conjugated AffiniPure Donkey Anti-mouse IgG secondary antibodies (1/500 in 1% BSA) (Jackson Laboratories) for 30 min. Coverslips were then incubated in 4′,6-diamidino-2-phenylindole (DAPI) (1/500 in PBS) for 5 mins before mounting using Dako Mounting Medium (Agilent Technologies). Slides were imaged using the WaveFX confocal microscope (Quorum Technologies). The number of lysosomes in each cell was quantified manually and blindly by Jared Bouchard and Grace Essuman using ImageJ software. Cell boundaries were identified by the kAE1 stain, cells without kAE1 staining were not counted and the quantity of lysosomes present in mIMCD3 cells was analyzed in GraphPad Prism using a one-way ANOVA followed by Dunnet's multiple comparisons test. P-value of 0.05 or less was considered significant.

Live-cell Imaging eGFP- RFP-LC3 construct

RFP-eGFP-LC3 cDNA construct (kind gift from Dr. Goping, University of Alberta) was transiently transfected in mIMCD3 cells expressing kAE1 WT-HA or variants. In a 6-well plate, mIMCD3 cells expressing kAE1 WT or kAE1 mutants were grown on glass coverslips until 70% confluency. 1 µg of RFP-eGFP-LC3 cDNA and 3 µL of X-tremeGENE HP DNA transfection reagent (Roche) were diluted in 100 µL of optimum (Gibco) and added dropwise to the wells containing 1 ml serum free optimum (no antibiotics) and kept at 37 ºC. After 4 hours, 1 mL of complete medium with antibiotics was added to the wells and cells further incubated at 37ºC for 48 hours. Cells were then incubated with mouse anti-HA primary antibody (Abcam, 1/250) in complete medium for 20 mins at 37 ºC. After washing the cells twice with warm PBS, cells were incubated with donkey anti-mouse antibody coupled to Alexa649 (Jackson IR, 1/250) in complete medium for 20 mins at 37ºC in the dark. To stain the nucleus, Hoescht stain (ImmunoChemistry) diluted in warm PBS was added to the wells for 5 min and then coverslips were washed twice with warm PBS prior to live-cell imaging using a WaveFX confocal microscope (Quorum Technologies, 40X objective) powered by a Volocity software. Yellow puncta correspond to mature autophagosomes, and red puncta correspond to acid-lumen lysosomes. The far-red signal corresponds to the kAE1 staining. Puncta quantity and size are yet to be analyzed.

Mouse Kidney Sections

Mouse kidney homogenates from kAe1 R607H mice (murine equivalent to human R589H)(Mumtaz et al., 2017) were used to study autophagy *in-vivo*. Mouse kidney homogenates were prepared as previously described but with modifications (Mumtaz et al., 2017). After cardiac perfusion with PBS and heparin, and kidney decapsulation, mouse kidneys pieces were

homogenized every 15 min for 1 hour on ice in ice-cold RIPA lysis buffer, supplemented with the following protease inhibitors: Pepstatin, PMSF, Aprotinin and Leupeptin. The homogenates were then centrifuged at 14 000 rpm at 4^{o}C for 15 min. An aliquot of the supernatant was saved for BCA, the remainder was stored in Laemmli buffer at -20^{o}C until further use. 20-60 μg of samples were loaded on 8, 10 or 12% SDS-PAGE gels at 200 V for 45 min and proteins were transferred onto PVDF membranes at 100 V for 1.5 hours. The blots were blocked with 3% skim milk in TBST for 1 hour at room temperature prior to incubation with primary and corresponding secondary antibodies as summarized in Table **3.2.** Clarity Western chemiluminescent detection reagent (Bio-Rad) was used for detection and visualization was done using the ChemiDoc MP Imaging system (BioRad). ImageLab freeware (Bio-Rad) was used to quantify the relative band intensities and results analyzed using a one-way ANOVA with a Dunnett's multiple comparison test. P-value of 0.05 or less was considered significant.

Table 3.2. Antibody conditions used in RH mouse kidney homogenate western blot experiments. Hour (hr), and room temperature (RT).

Antibody	Species	Incubation Conditions	Solution	Ideal Dilution (Secondary in brackets (if not 1/10000))	Manufacture	Band size (kDa)
Actin-HRP conjugated	Mouse	1 hr RT	1% Milk + TBST	1/10000	BioLegend	43
LC3B	Rabbit	O/N 4°C	1% Milk + TBST	1/1000 (1/2500)	Cell Signaling	14-16
IVF-12 s (Ae1)	Mouse	O/N 4°C	1% Milk + TBST	1/2500	Developmental Studies Hybridoma Bank	96
P mTOR (Ser 2448)	Rabbit	O/N 4°C	1% Milk + TBST	1/1000 (1/2500)	Cell Signaling	289
mTOR	Rabbit	O/N 4°C	1% Milk + TBST	1/1000 (1/2500)	Cell Signaling	289
p4E-BP1 (Ser65)	Rabbit	1 hr RT (better O/N 4°C)	1% Milk + TBST	1/750 (1/2500)	Cell Signaling	16-20
4E-BP1	Rabbit	1 hr RT (better O/N 4°C)	1% Milk + TBST	1/1500 (1:2500)	Cell Signaling	16-20
p62	Mouse	O/N 4°C	1% Milk + TBST	1/10000	Abcam	62
p53	Mouse	O/N 4°C	1% Milk + TBST	1/5000	Cell Signalling	53
Cleaved caspase 3	Rabbit	O/N 4°C	1% Milk + TBST	1/1000 (1/2500)	Cell Signalling	19

Statistics

All calculations were done in GraphPad Prism version 9. Results were analyzed using a one-way ANOVA with a Dunnett multiple comparison test, unless stated otherwise. P-value of 0.05 or less was considered significant.

Results:

kAE1 R295H is less abundant, while S525F and R589H are abundantly expressed in mIMCD3.

Recessive R295H and dominant S525F (unpublished data from Dr. Rosa Vargas-Poussou; Bruce L, 1997, JCI), R589H (Jarolim et al., 1998) are dRTA-causing mutations. To study these mutations *in vitro,* mIMCD3 cells expressing kAE1 WT-HA, R295H-HA, S525F-HA and R589H-HA were generated prior to my arrival in the lab. To ensure that the cells express kAE1, immunoblots were performed to examine kAE1 abundance in the different cell lines. As shown in **Figure 3.1**, R295H kAE1 is less abundant than WT (9.2 ± 4.6% of WT, n = 6, ± SEM) whereas S525F and R589H kAE1 are significantly more abundant (233 ± 26% and 261 ± 61% respectively, n = 6, ± SEM). Given the low abundance of the kAE1 R295H mutant, which progressively worsened over the course of our experiments, a limited number of experiments were performed. In the next sections, an average of only 3 experiments were performed with this mutant, thus producing results of limited robustness.

To ensure that the autophagy-altering treatments are not affecting kAE1 expression, kAE1 abundance was studied post treatment with bafilomycin A1 (baf) or after starvation. As shown in Supplementary Figures, Appendix A **Figure 5.2**, neither treatment influenced kAE1 abundance in any of the cell lines. kAe1 expression was next examined in kAe1 R607H KI mice.

When kidney homogenates from WT or kAe1 R607H KI mice were compared, there was no significant difference between kAe1 abundance in Ae1 R607H KI ($Ae1^{R607H/R607H}$) and WT mice (113 ± 35% of WT, n = 5 ± SEM) (Figure 2.1C). However, Ae1 R607H heterozygous mice kidneys ($Ae1^{+/R607H}$) had a significantly higher abundance of Ae1 (205 ± 35% of WT. n = 9 ± SEM *$p<0.05$). No conclusions can be made because the mouse anti-IVF-12s antibody detects Ae1 found in red blood cells as well as kAe1, and differences in cardiac perfusion may explain these differences.

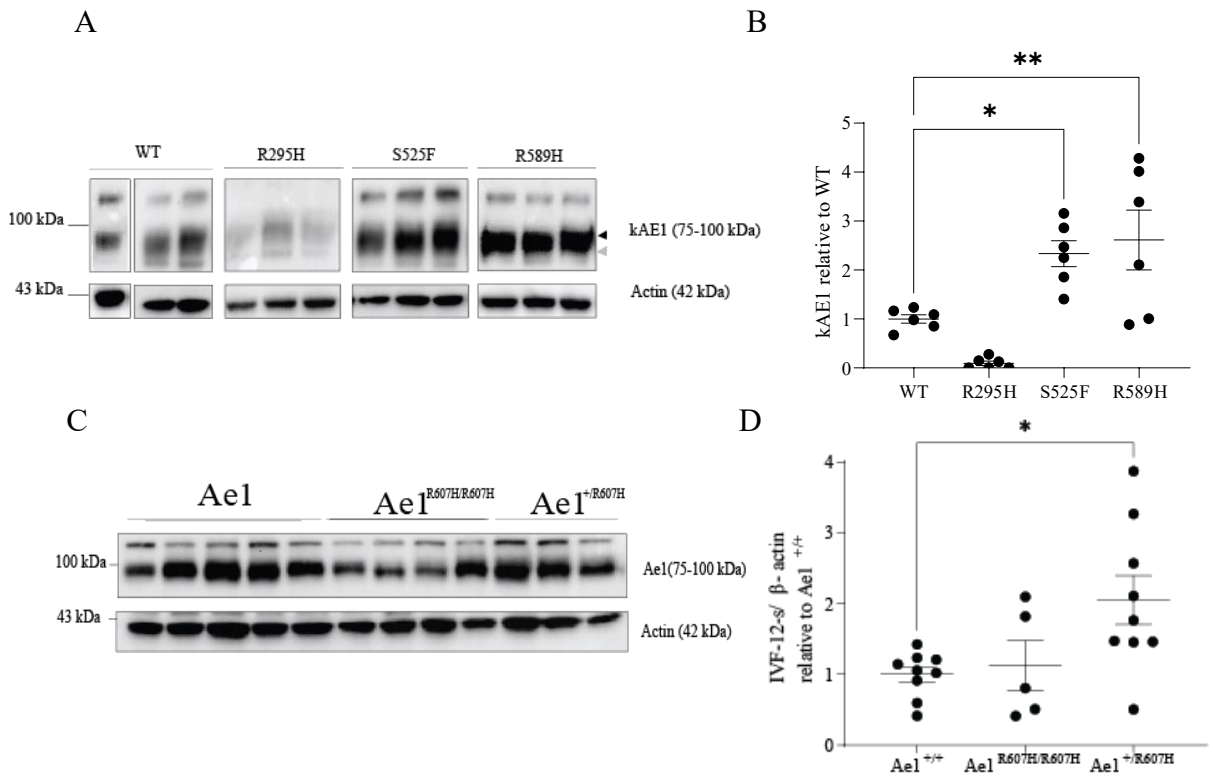

Figure 3.1. kAE1 abundance in mIMCD WT, R295H, S525F and R589H kAE1-HA cells and Ae1 abundance in $Ae1^{+/+}$, $Ae1R^{607H/R607H}$, and $Ae1^{+/R607H}$ mouse kidney lysates**. (A)** Immunoblot of mIMCD WT, R295H, S525F and R589H cells treated with doxycycline for 48hr prior to lysis with RIPA buffer. Rat anti-HA antibody was used to detect kAE1-HA, black and grey arrowheads represent kAE1 carrying complex and high mannose oligosaccharides, respectively. **(B)** Graphical representation of blot shown in A. Error bars correspond to mean ± SEM, n=6. *P<0.05,**P < 0.01, ****P < 0.0001 using one-way ANOVA with Dunnet's multiple comparison post hoc test. **(C)** Immunoblot of $Ae1^{+/+}$, $Ae1^{R607H/R607H}$, and $Ae1^{+/R607H}$ mouse kidney homogenates lysed with RIPA buffer. Mouse anti-IVF 12s antibody was used to detect Ae1, which detects Ae1 in both red blood cells and kidneys. **(D)** Graphical representation of blot shown in A. Error bars correspond to mean ± SEM, n= minimum 5. *P<0.05,**P < 0.01, ****P < 0.0001 using one-way ANOVA with Dunnett's multiple comparison post hoc test.

kAE1 mutants do not acidify the cytosol to the same extent as kAE1 WT expressing cells.

dRTA mutant cells do not acidify intracellularly to the same extent as WT cells and behave similarly to WT -DOX cells, cells that do not express kAE1. In **Figure 3.2,** WT -DOX cells have an initial cytosolic pH (pHi) of 7.35 ± 0.051 and WT +DOX cells have a significantly lower pHi of 7.09 ± 0.042 (n=14 ± SEM). The mutants are all alkaline compared to WT +DOX and are not significantly different from WT -DOX, R295H: 7.31 ± 0.055, S525F: 7.41 ± 0.063, R589H: 7.23 ± 0.12 (n=4-9 ± SEM). Recall that intracellular pH alters mTOR function and that it can have an effect on autophagy and cell death processes (Balgi et al., 2011; Kazyken et al., 2021)

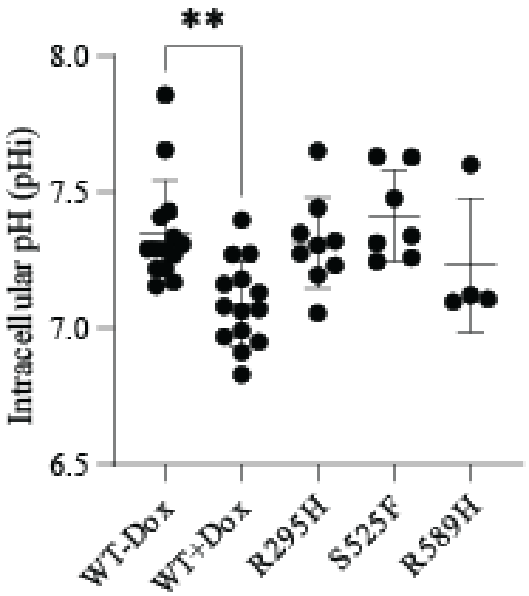

Figure 3.2. Initial cytosolic pH of kAE1 WT and dRTA mutant mIMCD cells. Initial cytosolic pH was measured for the 20 seconds before switching from a Cl^- containing to a Cl^- free Ringer's perfusion solution in mIMCD3 kAE1 WT, R295H, S525F or R589H cells in a functional assay using a Photon Technologies International (PTI) spectrophotometer(Lashhab et al., 2019). All cells except for WT-Dox were induced for 24 hours with doxycycline. Error bars correspond to means ± SEM, n=4-14, **P < 0.01 using one-way ANOVA with Dunett's multiple comparison post hoc test, compared with WT -DOX. Experiment done by Dr. Rawad Lashhab.

At basal state, S525F and R589H cells have a higher ratio of LC3BII compared to WT cells, and LC3B abundance is higher in Ae1 R607H KI mice kidneys.

Autophagy marker Light Chain 3 (LC3) exists in non-lipidated, cytosolic (LC3BI) and lipidated, autophagosome-bound (LC3BII) forms in cells ongoing the autophagy process(Kabeya et al., 2000). Quantifying LC3BI lipidation into LC3BII is a common method of studying autophagy by immunoblot. The role of LC3B in autophagy formation and maturation can either be quantified as the ratio of LC3BII divided by the intensities of both LC3BI and LC3BII, or as the total amount of the LC3B in the sample compared to a housekeeping protein. A decrease in total LC3B could indicate that there is less autophagy or that more LC3BII is being degraded in the autolysosome. **Figure 3.3a** shows an immunoblot of kAE1 WT, R295H, S525F and R589H cells blotted with rabbit anti-LC3B antibody which detects LC3BI and LC3BII. The ratio of LC3BII is significantly higher for the S525F and R589H mutant (114 ± 3% and 113 ± 2%, respectively, n = 9 ± SEM). R295H (n=3) LC3BII ratio is not significantly different from WT.

In vivo, the ratio of LC3BII was not significantly different between R607H WT and R607H KI mice (**Figure 5.3,** Appendix A). However, when looking at the overall level of LC3B in mouse kidneys, R607H KI mice had a significantly higher level of total LC3B (195 ± 29% of WT, n= 5 ± SEM). The R607H heterozygous mice also had a significantly higher level of total LC3B (144 ± 6% of WT, n= 9 ± SEM).

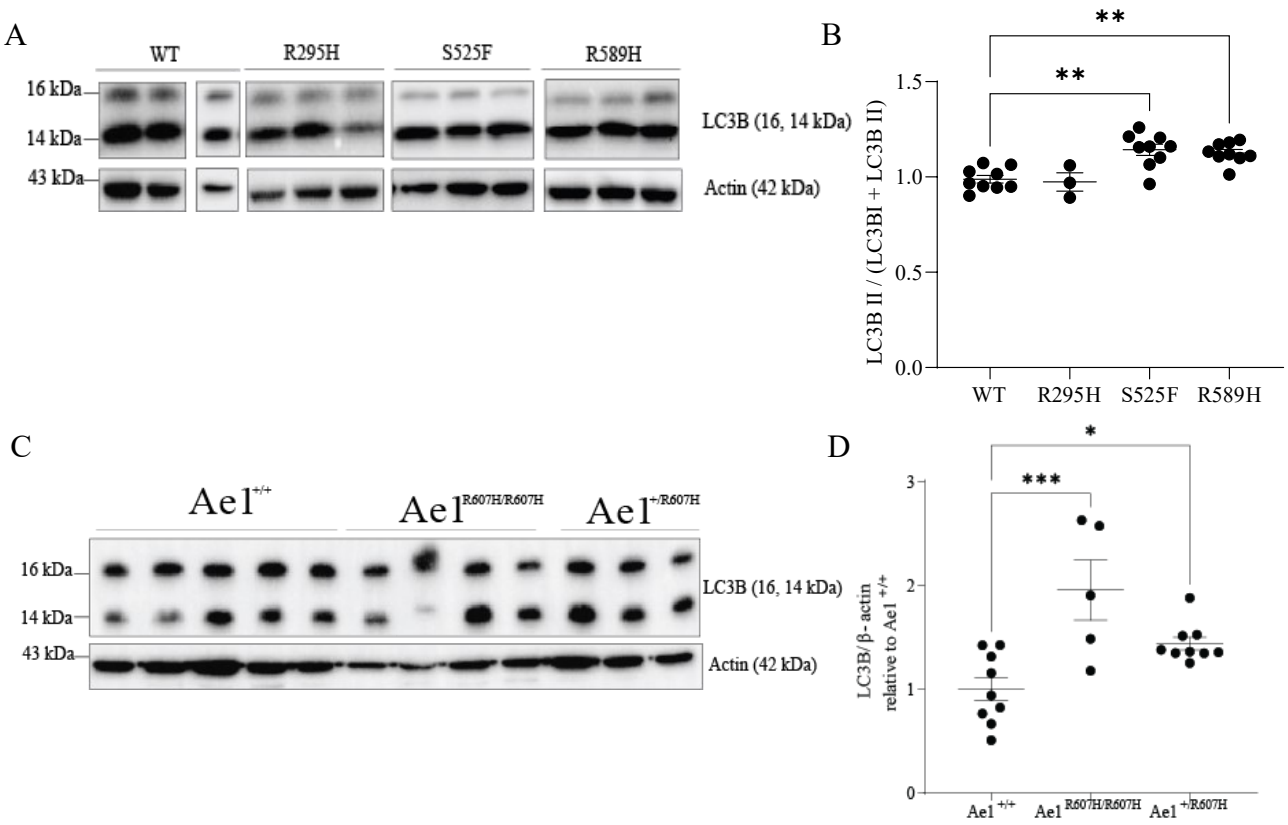

Figure 3.3. LC3B abundance in mIMCD WT, R295H, S525F and R589H kAE1-HA cells and in Ae1$^{+/+}$, Ae1R$^{607H/R607H}$, and Ae1$^{+/R607H}$ mouse kidney lysates. **(A)** Immunoblot of mIMCD WT, R295H, S525F and R589H cells treated with doxycycline for 48hr prior to lysis. Rabbit anti-LC3B antibody was used to detect LC3BI and LC3BII. **(B)** Graphical representation of blot shown in A. Values were calculated as a ratio of LC3BII band intensity divided by total LC3BI and II intensity normalized to WT values. Error bars correspond to mean ± SEM, n= minimum 3. *P<0.05, **P < 0.01, ****P < 0.0001 using one-way ANOVA with Dunett's multiple comparison post hoc test. **(C)** Immunoblot of Ae1$^{+/+}$, Ae1R$^{607H/R607H}$, and Ae1$^{+/R607H}$ mouse kidney homogenates. Rabbit anti-LC3B antibody was used to detect LC3BI and LC3BII. **(D)** Graphical representation of blot shown in C. Values were calculated by dividing the sum of the intensities of LC3BI and II by the intensity of the corresponding actin bands. Error bars correspond to mean ± SEM, n= minimum 5. *P<0.05, ****P < 0.0001 using one-way ANOVA with Dunett's multiple comparison post hoc test.

Both starvation and bafilomycin A1 reduce the LC3BII over total LC3B ratio in WT cells, but not in S525F or R295H. Only bafilomycin A1 decreased this ratio in R589H cells.

To unveil differences between WT and mutant cell lines, we challenged the cells by either inducing autophagy using starvation in HBSS medium for 2 hour prior to lysis, or blocking autophagy by inhibiting the lysosomal v-H^+-ATPase and autolysosome formation using bafilomycin A1 (BafA1) treatment (400 nM) for 4 hours prior to lysis(Kang & Avery, 2008; Yamamoto1 et al., 1998). We expected that bafA1 treatment would result in an autophagy block, in a decrease in the breakdown of LC3BII and hence lead to an accumulation in LC3BI abundance. This would result in an overall decreased ratio of LC3BII over total LC3B. Starving the cells was expected to trigger autophagy and lead to an accumulation of LC3BII without change in LC3BI, resulting in an increase of LC3BII over total LC3B ratio. As shown in **Figure 3.4 B**, in WT cells treated with BafA1, a decrease in the amount of LC3BII is observed (78 ± 3.8% from 99 ± 2% (control), n = 9 ± SEM). Surprisingly, a similar decrease is observed in starved cells (76 ± 4.2% from 99 ± 2% (control), n = 9 ± SEM). BafA1 had a similar effect in the R589H cells (104 ± 2.7 from 113 ± 1.8 (control), n = 9 ± SEM), but not starvation. Finally, no effect of bafA1 or starvation was observed in LC3B II over total LC3B ratio in R295H or S525F cells, suggesting an altered autophagy process in these cells.

A

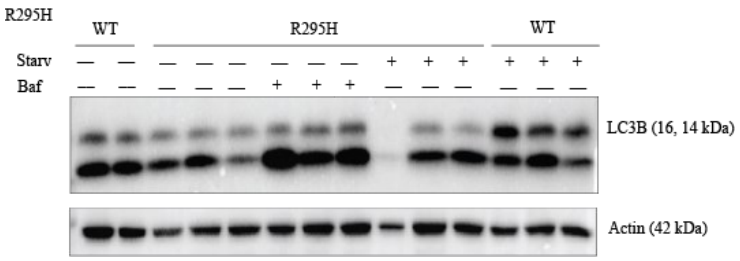
R295H
WT
R295H
WT
Starv
Baf
LC3B (16, 14 kDa)
Actin (42 kDa)

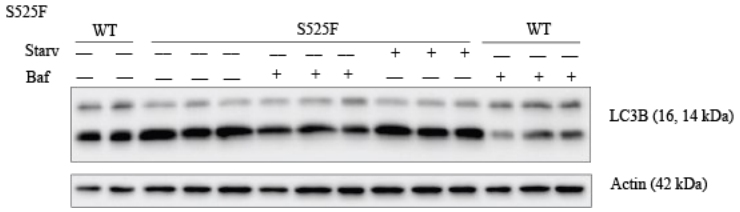
S525F
WT
S525F
WT
Starv
Baf
LC3B (16, 14 kDa)
Actin (42 kDa)

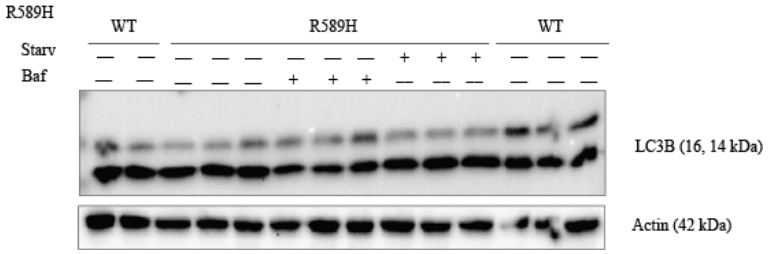
R589H
WT
R589H
WT
Starv
Baf
LC3B (16, 14 kDa)
Actin (42 kDa)

B

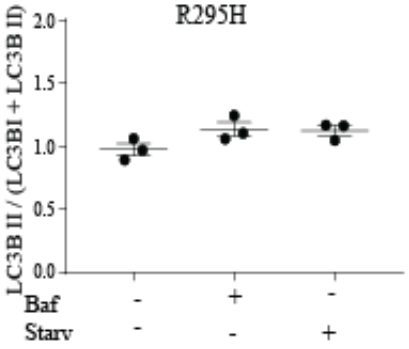
R295H
LC3B II / (LC3BI + LC3B II)
2.0
1.5
1.0
0.5
0.0
Baf
Starv

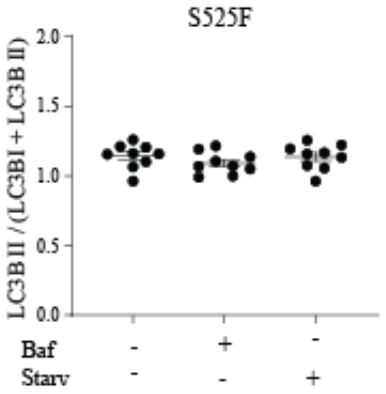
S525F
LC3B II / (LC3BI + LC3B II)
2.0
1.5
1.0
0.5
0.0
Baf
Starv

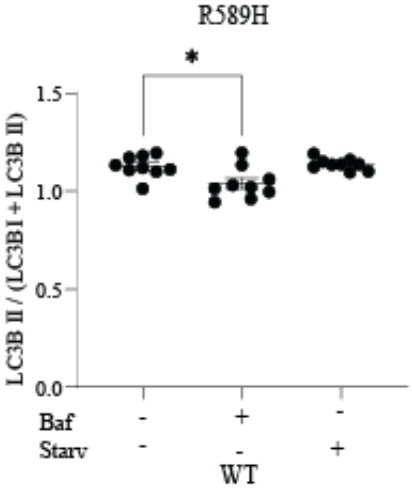
R589H
*
LC3B II / (LC3BI + LC3B II)
1.5
1.0
0.5
0.0
Baf
Starv

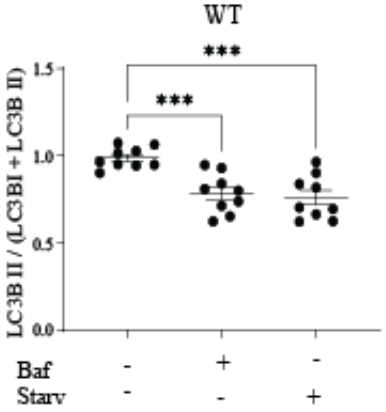
WT
***
***
LC3B II / (LC3BI + LC3B II)
1.5
1.0
0.5
0.0
Baf
Starv

Figure 3.4. LC3B abundance in mIMCD WT, R295H, S525F and R589H kAE1-HA cells under starved and bafilomycin A1 conditions. **(A)** Immunoblot of mIMCD WT, R295H, S525F and R589H cells treated with doxycycline for 48hr. Cells were treated with 400 nM Bafilomycin A1 (baf) for the last 4 hrs of the 48 hrs, or 2 hr incubation with HBSS (starv) or no treatment prior to lysis with RIPA buffer. Rabbit anti-LC3B antibody was used to detect LC3BI and LC3BII. **(B)** Graphical representation of blot shown in A. Values correspond to LC3BII band intensity divided by total LC3BI and II intensity normalized to the WT ratio. Error bars correspond to mean ± SEM, n= minimum 3. *P<0.05, ***P < 0.001 using one-way ANOVA with Dunett's multiple comparison post hoc test.

At basal state, p62 is equally abundant in WT and Ae1 R607H KI mice kidneys but p62 abundance is increased in kAE1 R295H expressing cells.

p62 is the bridge between ubiquitinated protein(Liu et al., 2016) and LC3BII and is a marker of autophagy. Since Mumtaz and colleagues found an accumulation of p62 in intercalated cells of Ae1 R607H KI mice kidney sections(Mumtaz et al., 2017), we examined the abundance of this marker in cells and mouse kidney homogenates. The R589H mutation is the human equivalent of R607H in mice but R589H cells did not have a significantly higher level of p62 abundance nor did the R607H mice kidneys (**Figure 3.5**). Cells expressing the S525F variant also did not have a higher abundance of p62. kAE1 R295H however, was the only variant that had a significantly higher level of p62 abundance (188 ± 4% of WT, n = 3 ± SEM).

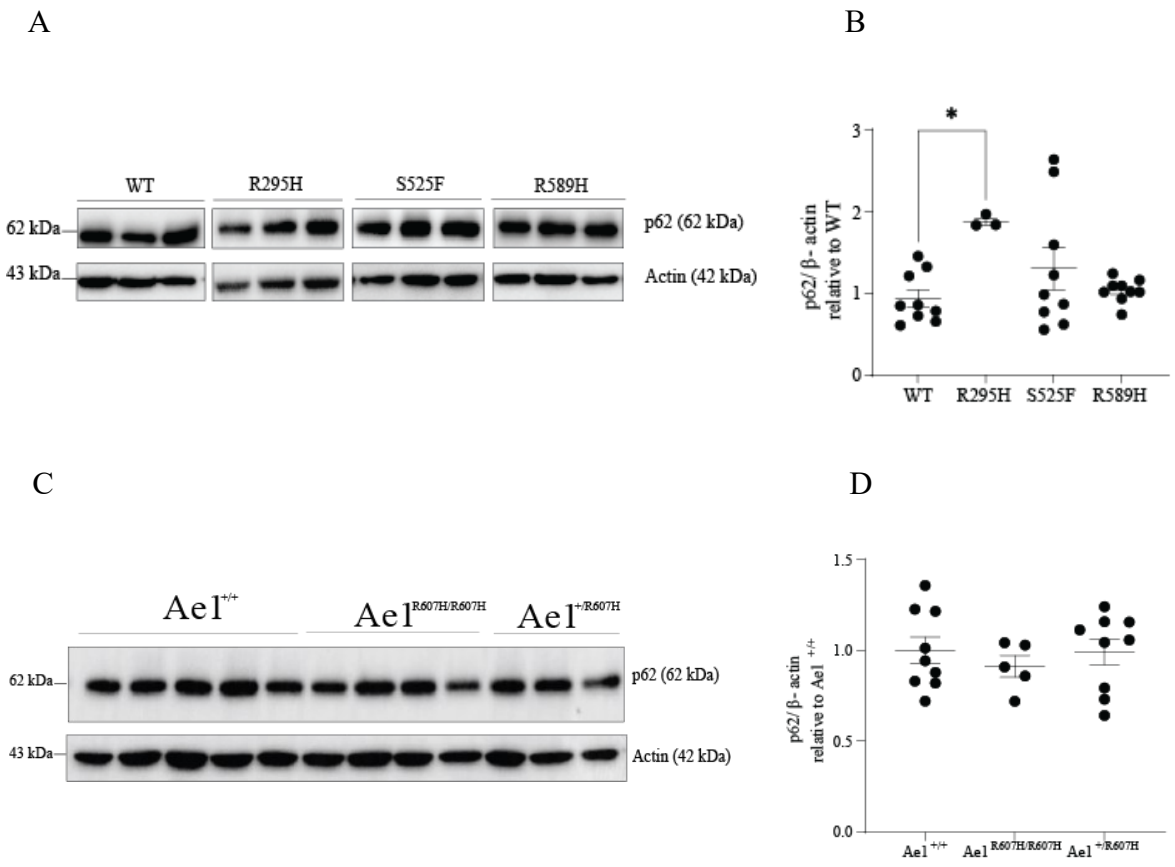

Figure 3.5. p62 abundance in mIMCD WT, R295H, S525F and R589H kAE1-HA cells and p62 abundance in $Ae1^{+/+}$, $Ae1R^{607H/R607H}$, and $Ae1^{+/R607H}$ mouse kidney lysates**. (A)** Immunoblot of mIMCD WT, R295H, S525F and R589H cells treated with doxycycline for 48hr prior to lysis. Mouse anti-p62 antibody was used to detect p62. **(B)** Graphical representation of blot shown in A. Error bars correspond to mean ± SEM, n= minimum 3. *P<0.05, using one-way ANOVA with Dunnet's multiple comparison post hoc test. **(C)** Immunoblot of $Ae1^{+/+}$, $Ae1^{R607H/R607H}$, and $Ae1^{+/R607H}$ mouse kidney lysates lysed with RIPA lysis buffer. Mouse anti-p62 antibody was used to detect p62. **(D)** Graphical representation of blot shown in A. Error bars correspond to mean ± SEM, n= minimum 5. No statistical difference was found using one-way ANOVA with Dunett's multiple comparison post hoc test.

p62 abundance is increased by bafilomycin A1 and starvation in kAE1 WT expressing mIMCD3 cells but not in mutant expressing cells.

We next reasoned that conditions that affect autophagy flux may unveil differences in p62 abundance between WT or mutant expressing cells. Starvation is reported to trigger autophagy(Mizushima et al., 2002; Takeshige et al., 1992; Tsukada & Ohsumi, 1993) while bafA1 inhibits lysosomal ATPase and autolysosome formation(Yamamoto1 et al., 1998) resulting in a block of autophagy flux. The accumulation of p62 in Ae1 R607H KI mouse kidney sections(Mumtaz et al., 2017) suggests that autophagy flux is blocked in mutant cells, resulting in accumulation of this marker in cells. Therefore, we hypothesized that at basal state, mutant cells display an equivalent abundance of p62 as in bafA1 treated conditions, and that starving will restore autophagy function if this is possible. As shown in **Figure 3.6**, starvation and bafA1 increase p62 levels only in WT kAE1 cells. The ratio of p62 increased to 193 ± 18% for bafA1 treatment and 178 ± 36% for starvation (Figure 2.6b, n=6 ± SEM).

A

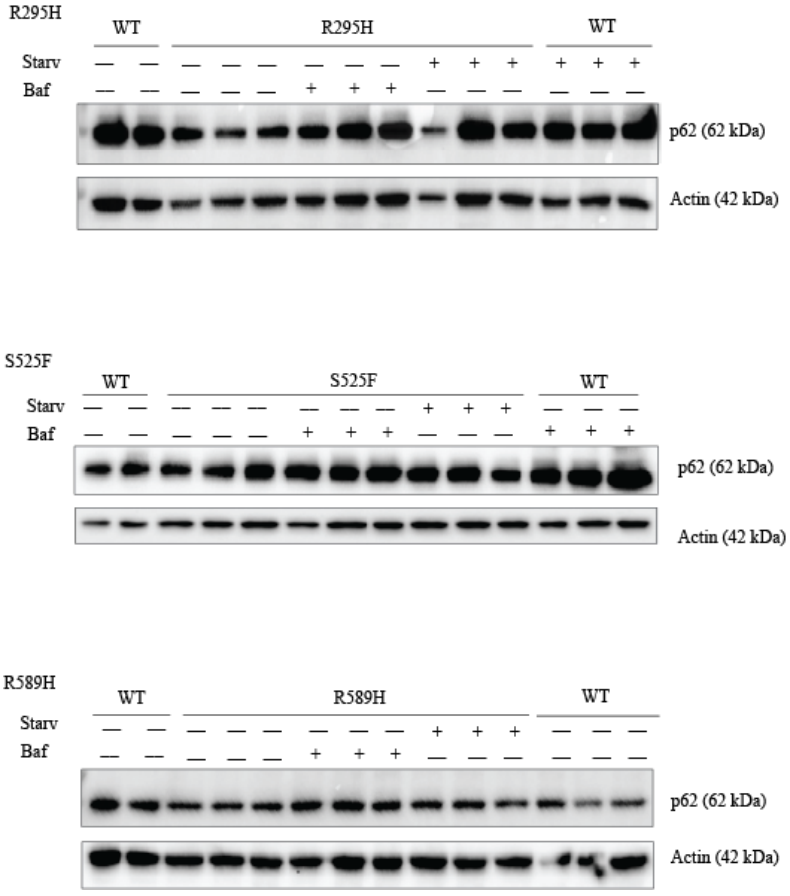
R295H
WT
R295H
WT
Starv
Baf
p62 (62 kDa)
Actin (42 kDa)
S525F
WT
S525F
WT
Starv
Baf
p62 (62 kDa)
Actin (42 kDa)
R589H
WT
R589H
WT
Starv
Baf
p62 (62 kDa)
Actin (42 kDa)

B

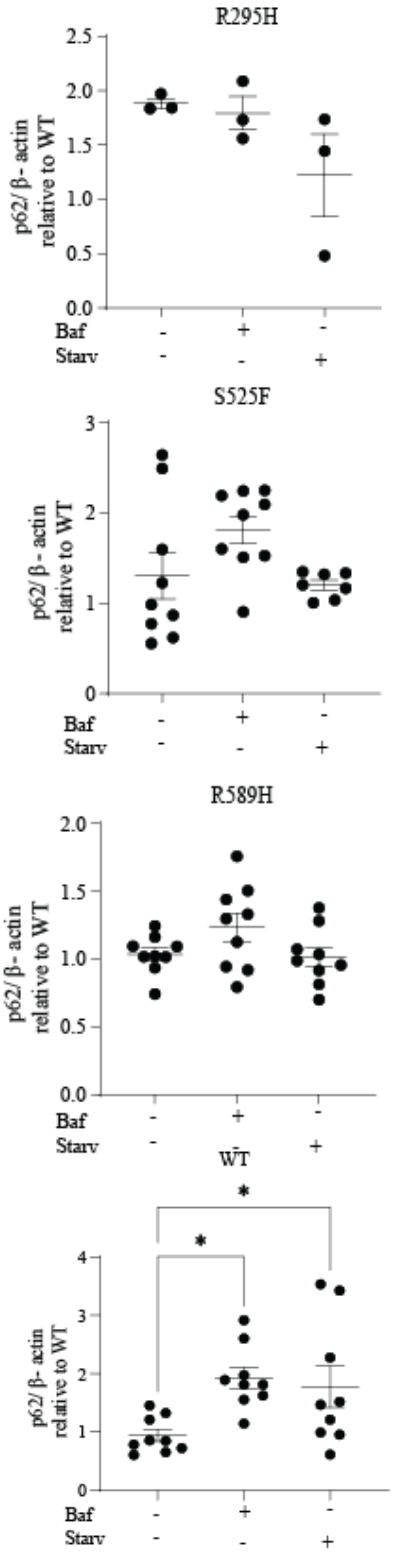
R295H
p62/ β- actin relative to WT
Baf
Starv
S525F
p62/ β- actin relative to WT
Baf
Starv
R589H
p62/ β- actin relative to WT
Baf
Starv
WT
p62/ β- actin relative to WT
Baf
Starv

Figure 3.6. p62 abundance in mIMCD WT, R295H, S525F and R589H kAE1-HA cells under starved or bafilomycin A1 conditions. **(A)** Immunoblot of mIMCD WT, R295H, S525F and R589H cells treated with doxycycline for 48hr. Cells were treated with 400 nM Bafilomycin A1 (baf) for the last 4hrs of the 48 hrs, or 2 hr incubation with HBSS (starv) or no treatment prior to lysis with RIPA buffer. Mouse anti-p62 antibody was used to detect p62. **(B)** Graphical representation of blot shown in A. Error bars correspond to mean ± SEM, n= minimum 3. *P<0.05, using one-way ANOVA with Dunett's multiple comparison post hoc test.

At basal state, cells expressing kAE1 R295H have a higher ratio of phosphorylated 4E-BP1 than WT cells, but the other mutant cells do not.

Phosphorylation of 4E-BP1 is a marker of decreased autophagy as the activation of mTOR results in the downstream phosphorylation of 4E-BP1(Gingras et al., 1998). R295H variant had a large significant increase in 4E-BP1 phosphorylation (989 ± 108% of WT n=3 ± SEM) (**Figure 3.7 B**). However, none of the other mutants displayed a significant difference in phosphorylated 4E-BP1 compared to WT cells. This result indicates that the autophagy activation is intact in WT, S525F and R589H mutant cells but is altered in kAE1 R295H expressing cells. We next examined the effect of starvation or ATPase blockage (bafA1 treatment) on phosphorylated 4E-BP1 abundance in WT or mutant expressing cells.

A B

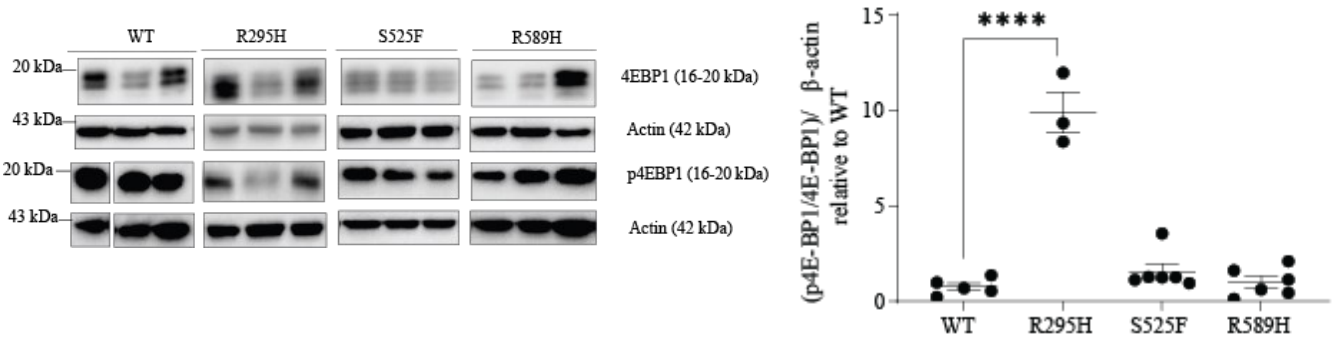

Figure 3.7. 4E-BP1 phosphorylation ratio in mIMCD WT, R295H, S525F and R589H kAE1-HA cells. **(A)** Immunoblot of mIMCD WT, R295H, S525F and R589H cells treated with doxycycline for 48 hr prior to lysis. Rabbit anti-4E-BP1 was used to detect 4E-BP1 and rabbit anti-phosphorylated 4E-BP1 was used to detect phosphorylated 4E-BP1. **(B)** Graphical representation of blot shown in A. Values obtained by taking p4E-BP1 band density normalized to β-actin and then dividing it by 4E-BP1 band density normalized to β-actin all relative to the average WT value. Error bars correspond to mean ± SEM, n=

Starvation suppresses phosphorylation of 4E-BP1 in all cell lines.

The effect of starvation and bafA1 was next examined. Since starvation increases autophagy(Mizushima et al., 2002; Takeshige et al., 1992; Tsukada & Ohsumi, 1993), we hypothesized that 4E-BP1 phosphorylation will decrease upon starvation in WT cells, but that this mechanism may be altered in mutant cells.

As shown on **Figure 3.8 A**, starvation decreased the amount of detectable phosphorylated 4E-BP1 to undetectable levels in all cell lines (**Figure 3.8A**) and the level of phosphorylated 4E-BP1 was significantly less in WT, S525F and R589H cells compared to its respective no treatment control, however this was not seen using for the R295H cell line **(Figure 3.7B).** The statistical analysis is not reliable for this result due to a low sample size (**Figure 3.7B).** Starvation also altered the migration profile of 4E-BP1 and shifts it downwards in all cell lines as seen in **Figure 3.8A**, likely corresponding to the disappearance of the heavier phosphorylated 4E-BP1 form of the protein. Starvation triggered autophagy in all cell lines, including R295H cells which had a higher ratio of phosphorylated 4E-BP1 compared to WT. BafA1 treatment had no effect on the level of 4E-BP1 phosphorylation in all cell lines (**Figure 3.8B**). However, when comparing the effect of bafA1 on the level of phosphorylated 4E-BP1 between the cell lines, the R295H variant had a significantly higher level of phosphorylation (13.34 ± 3.23 for R295H and 1.029 ± 0.33 for WT, n= minimum 3 ± SEM) (**Figure 3.8C**). Overall, these results indicate that autophagy activation via starvation is appropriate in all the mutant cells lines, despite an initially elevated phosphorylated 4E-BP1 in R295H cell line at basal state. The rabbit anti-phosphorylated 4E-BP1 antibody was unable to detect the protein in Ae1 R607H KI mice kidneys therefore this method of examining autophagy flux was not applicable *in vivo*.

A

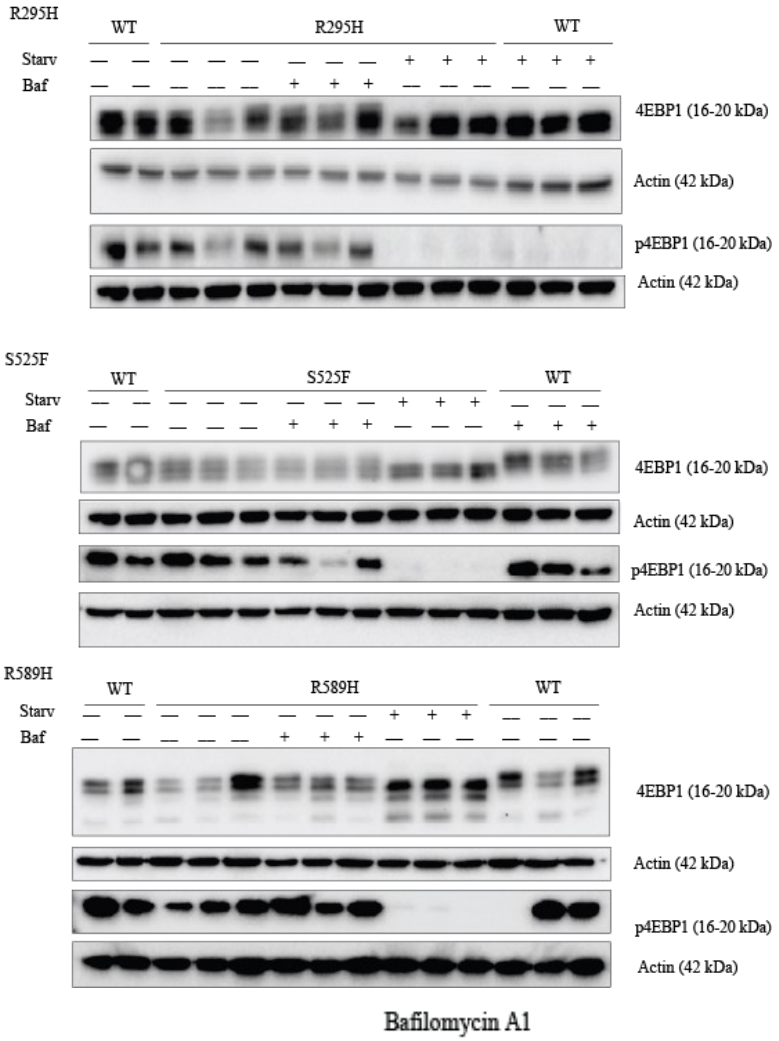
R295H
WT
R295H
WT
Starv
Baf
4EBP1 (16-20 kDa)
Actin (42 kDa)
p4EBP1 (16-20 kDa)
Actin (42 kDa)
S525F
WT
S525F
WT
Starv
Baf
4EBP1 (16-20 kDa)
Actin (42 kDa)
p4EBP1 (16-20 kDa)
Actin (42 kDa)
R589H
WT
R589H
WT
Starv
Baf
4EBP1 (16-20 kDa)
Actin (42 kDa)
p4EBP1 (16-20 kDa)
Actin (42 kDa)
Bafilomycin A1

B

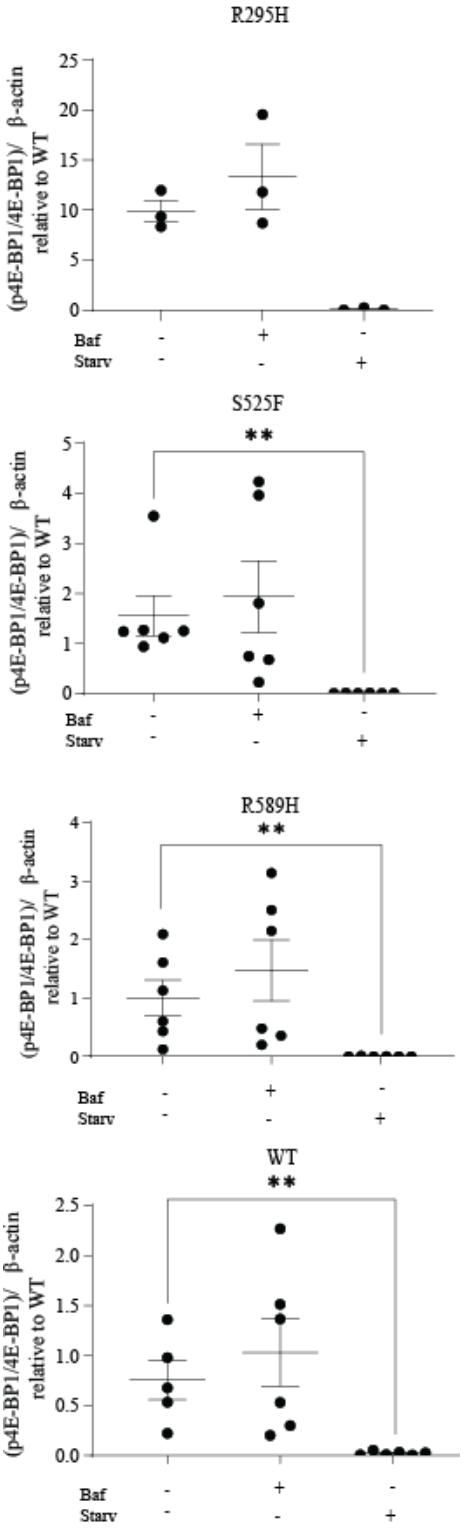
R295H
(p4E-BP1/4E-BP1)/ β-actin relative to WT
Baf
Starv
S525F
**
(p4E-BP1/4E-BP1)/ β-actin relative to WT
Baf
Starv
R589H
**
(p4E-BP1/4E-BP1)/ β-actin relative to WT
Baf
Starv
WT
**
(p4E-BP1/4E-BP1)/ β-actin relative to WT
Baf
Starv

C

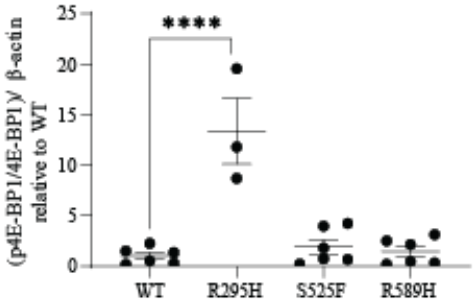
****
(p4E-BP1/4E-BP1)/ β-actin relative to WT
WT
R295H
S525F
R589H

Figure 3.8. Effect of starvation and bafilomycin A1 on 4E-BP1 phosphorylation ratio in mIMCD WT, R295H, S525F and R589H kAE1-HA cells. **(A)** Immunoblot of mIMCD WT, R295H, S525F and R589H cells treated with doxycycline for 48hr. Cells were treated with 400 nM Bafilomycin A1 (baf) for the last 4hrs of the 48 hrs, or 2 hr incubation with HBSS (starv) or no treatment prior to lysis with RIPA buffer. Rabbit anti-4E-BP1 was used to detect 4E-BP1 and rabbit anti-phosphorylated 4E-BP1 was used to detect phosphorylated 4E-BP1. **(B)** Graphical representation of blots shown in A. Values obtained by taking p4E-BP1 band density normalized to β-actin and then dividing it by 4E-BP1 band density normalized to β-actin all relative to the average WT value. Error bars correspond to mean ± SEM, n= minimum 3. **P < 0.01, ***P< 0.001, ****P < 0.0001 using one-way ANOVA with Kruskal-Wallis test. **(C)** Graphical representation of data from the bafilomycin A1 treated cell lines, data corresponds to blots shown in A. Error bars correspond to mean ± SEM, n= minimum 3. ****P < 0.0001 using one-way ANOVA with Kruskal-Wallis test.

At basal state, phosphorylated mTOR abundance is similar in all cell lines but is higher in the R295H expressing cells.

Phosphorylation of mTOR on Serine 2448 is a marker of decreased autophagy as mTOR activation results in phosphorylation of this residue(Rosner et al., 2010). Thus, an increase in S2448 phosphorylation indicates a decrease in autophagy. We first assessed S2448 mTOR phosphorylation at the basal state.

As shown in **Figure 3.9**, cells expressing the R295H variant had a large significant increase in mTOR phosphorylation (3.10 ± 0.32 for R295H n=3, and 0.82 ± 0.16 for WT n = 6 ± SEM). However, the other two mutant expressing cell lines were not significantly different from WT cells. One way to increase autophagy is to subject the cells to starvation and see the effect on phosphorylation. Since starvation increases autophagy, mTOR phosphorylation should decrease and if it does not then this could indicate that autophagy is not functioning normally. As such, all the cell lines were subject to starvation. On the other hand, bafA1 is supposed to block the lysosomal v-ATPase and result in a decrease of autophagy and an increase in the phosphorylation of mTOR. Unfortunately, these antibodies were not reliable for the R607H mouse kidney homogenates.

A B

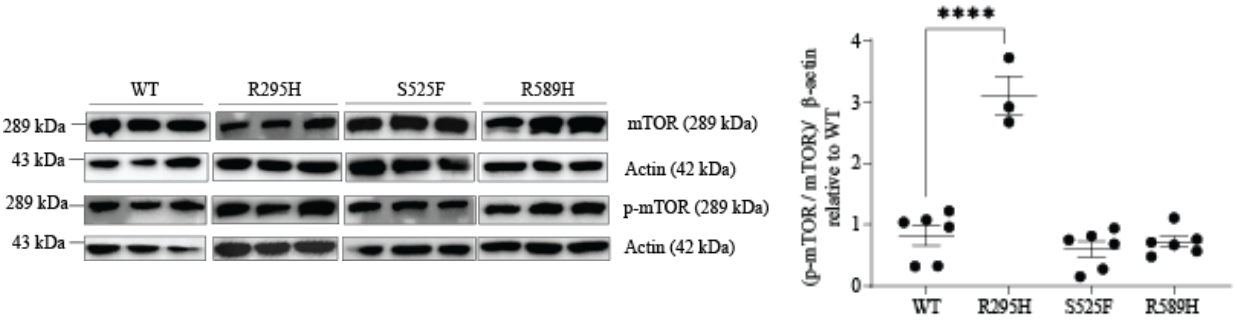

Figure 3.9. mTOR phosphorylation ratio in mIMCD WT, R295H, S525F and R589H kAE1-HA cells. **(A)** Immunoblot of mIMCD WT, R295H, S525F and R589H cells treated with doxcycycline for 48hr prior to lysis. Rabbit anti-mTOR was used to detect mTOR and rabbit anti-phosphorylated mTOR was used to detect phosphorylated mTOR (p-mTOR). **(B)** Graphical representation of blot shown in A. Values obtained by taking p-mTOR band density normalized to β-actin and then dividing it by mTOR band density normalized to β-actin all relative to the average WT value. Error bars correspond to mean ± SEM, n= minimum 3. ****P < 0.0001 using one-way ANOVA with Dunett's multiple comparison post hoc test.

Unlike in WT and S525F cells, starvation significantly suppresses mTOR phosphorylation in R295H and R589H cells.

Since starvation increases autophagy(Mizushima et al., 2002; Takeshige et al., 1992; Tsukada & Ohsumi, 1993), we hypothesized that mTOR phosphorylation will decrease upon starvation in WT cells and bafA1 treatment will increase mTOR phosphorylation, but that this mechanism may be altered in mutant cells. However, bafA1 treatment had no effect on mTOR phosphorylation in either WT or mutant cells as seen in **Figure 3.10 B**. Starvation on the other hand was expected to decrease mTOR phosphorylation. This was the case for R295H where the phosphorylation ratio decreased from 3.10 ± 0.32 to 0.94 ± 0.31 after 2 hour starvation (n=3 ± SEM), and R589H cells where the phosphorylation ratio decreased from 0.72 ± 0.09 to 0.35 ± 0.045 (n=6 ± SEM) after 2 hour starvation (**Figure 3.10b**).

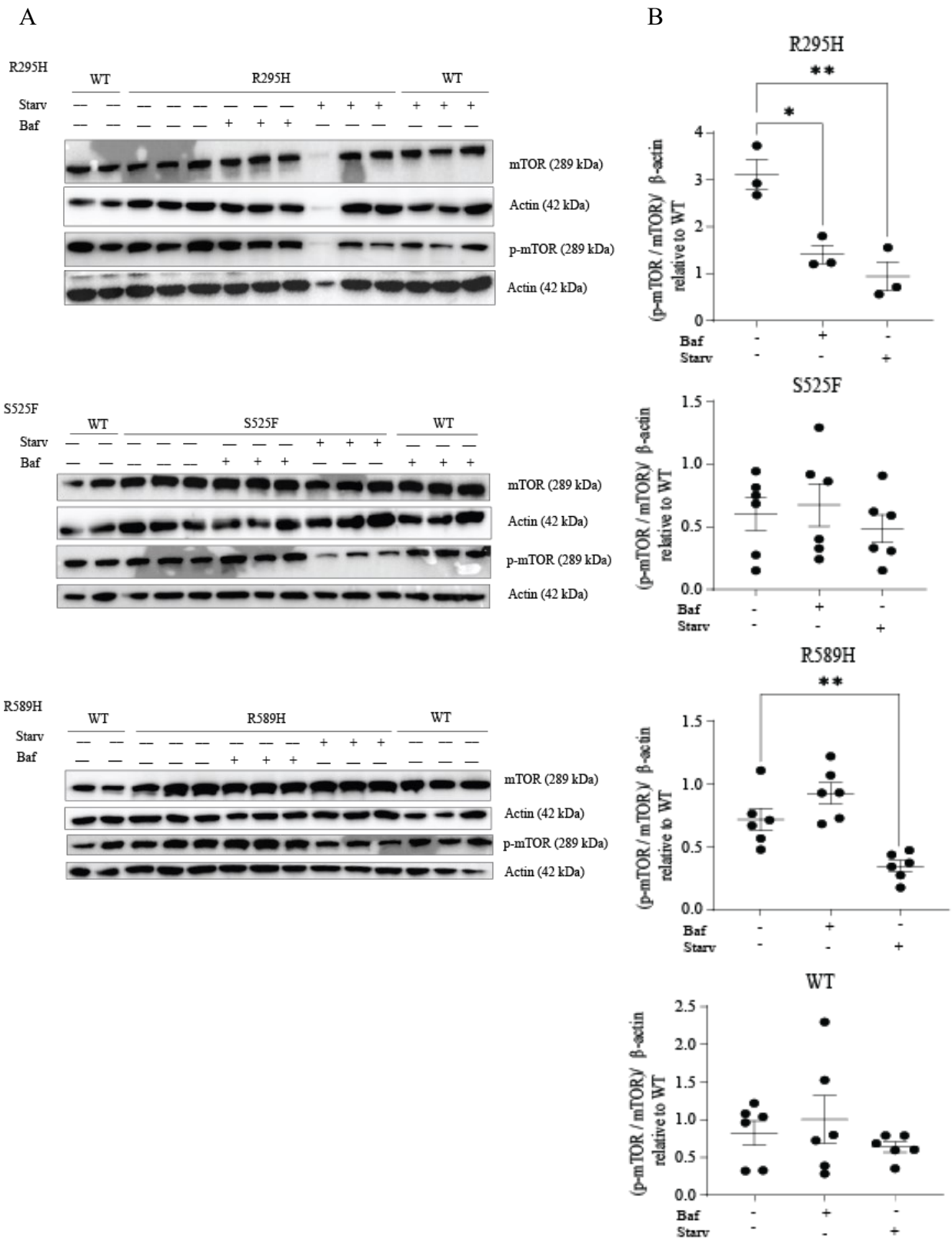
A
B
R295H
WT
R295H
WT
Starv
Baf
mTOR (289 kDa)
Actin (42 kDa)
p-mTOR (289 kDa)
Actin (42 kDa)
S525F
R589H
R295H
S525F
R589H
WT
(p-mTOR / mTOR)/ β-actin relative to WT
Baf
Starv

Figure 3.10. Effect of starvation and bafilomycin A1 on mTOR phosphorylation ratio in mIMCD WT, R295H, S525F and R589H kAE1-HA cells**. (A)** Immunoblot of mIMCD WT, R295H, S525F and R589H cells treated with doxycycline for 48hr. Cells were treated with 400 nM Bafilomycin A1 (baf) for the last 4 hrs of the 48 hrs, or 2 hr incubation with HBSS (baf) or no treatment prior to lysis with RIPA buffer. Rabbit anti-mTOR was used to detect mTOR and rabbit anti-phosphorylated mTOR (p-mTOR) was used to detect p-mTOR. **(B)** Graphical representation of blots shown in A. Values obtained by taking p-mTOR band density normalized to β-actin and then dividing it by mTOR band density normalized to β-actin all relative to the average WT value. Error bars correspond to mean ± SEM, n= minimum 3. *P<0.05,**P < 0.01 using one-way ANOVA with Dunnett's multiple comparison post hoc test.

S525F cells contain more functional lysosomes and R589H cells have bigger lysosomes than WT cells at the basal state.

To further assess autophagy flux in WT or mutant cell lines, we measured the ability of lysosomes to acidify using Magic red staining. Magic red substrate is cleaved by lysosomal cathepsins and the cresyl violet fluorophore becomes fluorescent upon excitation at 550-590 nm(Van Noorden et al., 1997). Thus, it was used to blindly quantify the number of and the size of functional lysosomes in the different cell lines. At steady state, the S525F cells have an increase in detectable lysosomes, with an average of 2.62 ± 0.30 lysosomes per cell (mean ± SEM, n=103 cells analyzed) compared to 0.79 ± 0.11 lysosomes per cell in WT (mean ± SEM, n=149 cells analyzed) **(Figure 3.11 B**). R295H and R589H cells are not different from WT. As per lysosome size, R89H cells have larger lysosomes compared to WT (3.57 ± 0.22 μm^2 for R589H and 2.94 ± 0.16 μm^2 for WT as shown in **Figure 3.11 C,** mean ± SEM, n= minimum 74**)**.

A

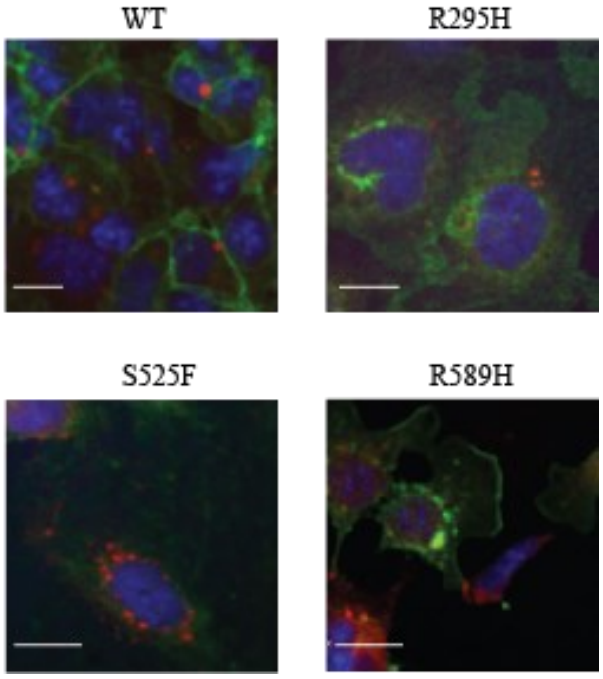
WT
R295H
S525F
R589H

B

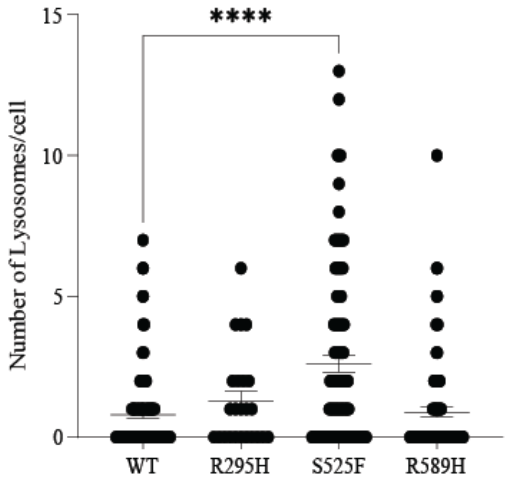
****
Number of Lysosomes/cell
15
10
5
0
WT
R295H
S525F
R589H

C

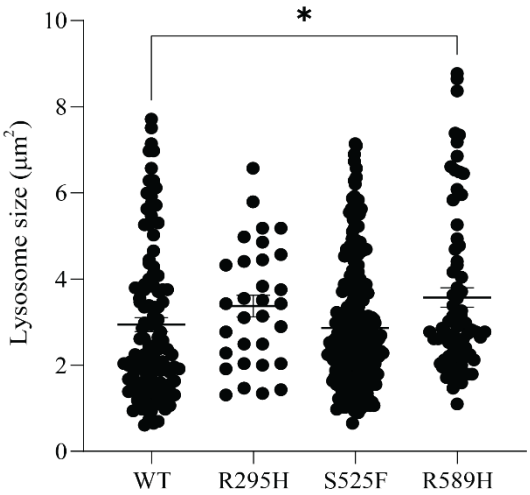
*
Lysosome size (μm²)
10
8
6
4
2
0
WT
R295H
S525F
R589H

Figure 3.11. Quantification of lysosome number and size in mIMCD WT, R295H, S525F and R589H kAE1-HA cells using Magic Red stain**. (A)** Immunofluorescence images of mIMCD WT, R295H, S525F and R589H kAE1-HA cells treated with Magic red substrate for 1hr at 37ºC under darkness and doxycycline for 48 hrs. Green staining corresponds to kAE1, red staining shows to lysosomes and blue corresponds to nuclei. Bar is 16 µm. **(B)** Graphical representation of lysosome number per cell. Error bars correspond to mean ± SEM, and 24-149 cells analyzed. *P<0.05, ****P < 0.0001 using one-way ANOVA with Dunnett's multiple comparison post hoc test. (C) Graphical representation of lysosome size in pixels. Error bars correspond to mean ± SEM, 24-149 cells analyzed. *P<0.05, using one-way ANOVA with Kruskal-Wallis test**.**

Starvation increases the number of lysosomes in R295H and S525F cells and decreases their size in R295H and R589H cells. Bafilomycin A1 decreases the size of lysosomes in S525F cells.

WT and kAE1 mutant cells were subjected to bafA1 and starvation before staining with magic red substrate. These treatments did not influence WT lysosomes, however there was an effect seen in the mutant cells. As seen in **Figure 3.12B** Starvation increased the number of lysosomes in R295H cells (3.57 ± 0.45 from 1.29 ± 0.34 lysosomes/cell, mean ± SEM. n = minimum 24). Starvation also decreased the size of lysosomes in R295H cells (3.37 ± 0.25 to 2.44 ± 0.06 μm^2, mean ± SEM. n = minimum 24). Starvation also increased the number of lysosomes in S525F cells (4.47 ± 0.49 from 2.62 ± 0.30 lysosomes/cell, mean ± SEM. n = minimum 79). Additionally, bafA1 decreased the size of lysosomes in S525F cells from 2.866 ± 0.09 μm^2 to 2.11 ± 0.08 μm^2 (mean ± SEM, n= minimum 121). Starvation resulted in a decrease in size of R589H lysosomes from 3.57 ± 0.22 μm^2 to 2.77 ± 0.12 μm^2.

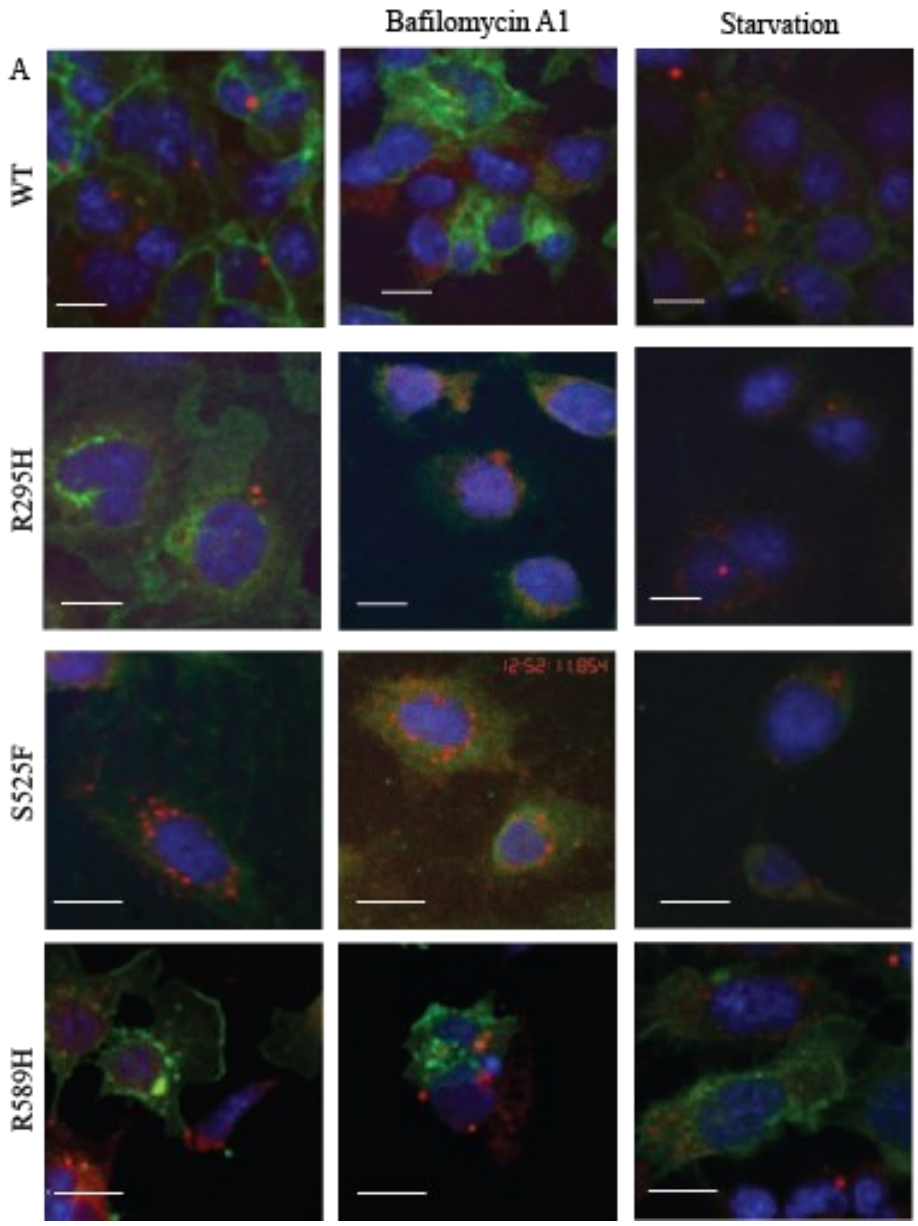
A
Bafilomycin A1
Starvation
WT
R295H
S525F
R589H

B

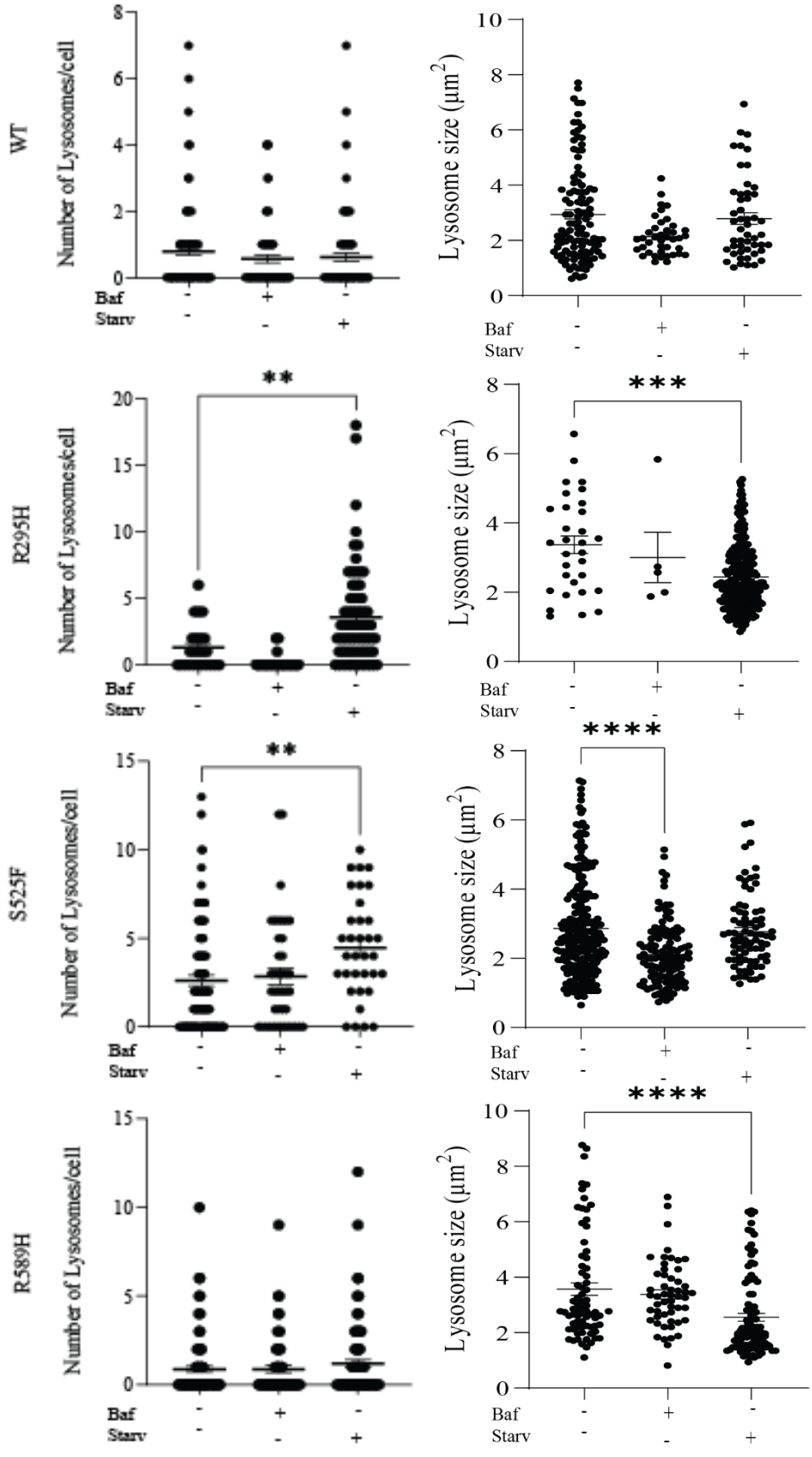
WT
R295H
S525F
R589H
Number of Lysosomes/cell
Lysosome size (µm²)
Baf
Starv
**
***
****

Figure 3.12. Quantifying lysosome number and size mIMCD WT, R295H, S525F and R589H kAE1-HA cells using Magic Red stain after bafilomycin A1 and starvation. **(A)** Immunofluorescence images captured on wave fx 1 of mIMCD WT, R295H, S525F and R589H kAE1-HA cells treated with dox for 48 hours and or 400 nm bafilomycin A1 (baf), starvation with HBSS (starv) for 2 hour or no treatment. The cells were incubated with magic red substrate for 1hr at 37^{o}C under darkness. green corresponds to kAE1 staining, red corresponds to lysosomes and blue corresponds to nuclei. White bar is 16 µm **(B)** Graphical representation of lysosome number per cell (left graphs) and graphical representation of lysosome size in μm^2 (right graphs). Error bars correspond to mean ± SEM, n= minimum 2 and 24-149 cells analyzed. *P<0.05,**P < 0.01, ****P < 0.0001 using one-way ANOVA with Dunett's multiple comparison post hoc test (left graphs). Error bars correspond to mean ± SEM, n= minimum 2 and 24-255 cells analyzed. *P<0.05,**P < 0.01, ****P < 0.0001 using one-way ANOVA with Kruskal-Wallis test (right graphs).

p53 levels are unaffected with the expression of dRTA mutant kAE1.

Another hypothesis we considered is cell death via apoptosis which may account for the loss of alpha intercalated cells. To study this hypothesis, I looked at p53 and cleaved caspase 3 *in vitro* and *in vivo.* As seen in **Figure 3.13,** There was no difference in the abundance of p53 in WT and mutant cell lines. There was also no difference between R607H KI and WT mouse kidneys.

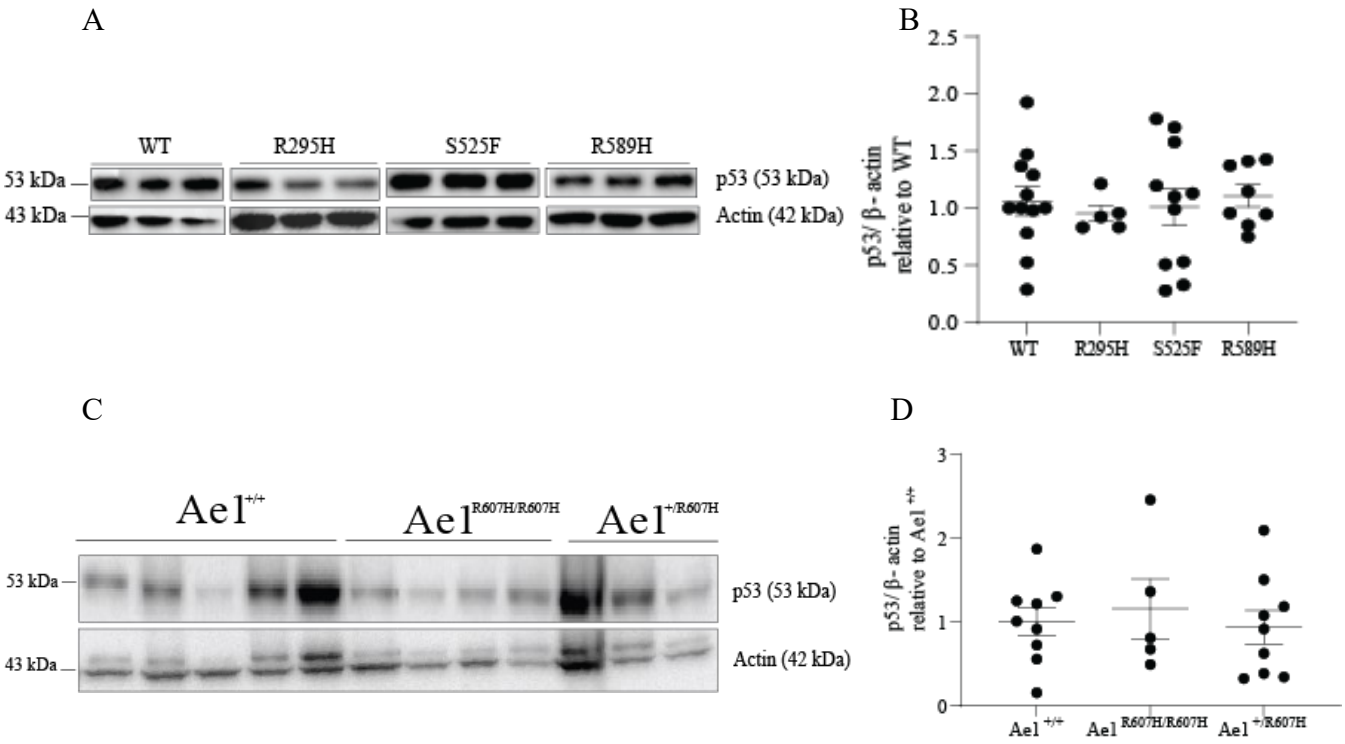

Figure 3.13. p53 abundance in mIMCD WT, R295H, S525F and R589H kAE1-HA cells and p53 abundance in Ae1+/+, Ae1R607H/R607H, and Ae1+/R607H mouse kidney lysates**. (A)** Immunoblot of mIMCD WT, R295H, S525F and R589H cells treated with dox for 48hr prior to lysis with RIPA lysis buffer. Mouse anti-p53 antibody was used to detect p53. **(B)** Graphical representation of blot shown in A. Error bars correspond to mean ± SEM, n= minimum 3. *P<0.05,**P < 0.01, ****P < 0.0001 using one-way ANOVA with Dunnet's multiple comparison post hoc test. **(C)** Immunoblot of $Ae1^{+/+}$, $Ae1^{R607H/R607H}$, and $Ae1^{+/R607H}$ mouse kidney lysates lysed with RIPA lysis buffer. Mouse anti-p53 antibody was used to detect p53. **(D)** Graphical representation of blot shown in A. Error bars correspond to mean ± SEM, n= minimum 5. *P<0.05,**P < 0.01, ****P < 0.0001 using one-way ANOVA with Dunett's multiple comparison post hoc test.

Cleaved caspase 3 is reduced in the S525F and R589H mutant expressing cells.
To further assess cell death, we examined the other apoptosis marker: cleaved caspase 3 abundance. As seen in **Figure 3.14,** levels of cleaved caspase 3 in the S525F mutant expressing cells decreased to 19.0 ± 5.0% of WT and to 52.2 ± 13.1% of WT in R589H mutant expressing cells. Recall that an increase in pH modulates mTOR activity and in particular, it was shown to have a positive effect on mTORC2 which inhibits apoptosis(Kazyken et al., 2021). However, pH increases autophagy which may possibly lead to uncontrolled autophagy and uncontrolled autophagic cell death. Unfortunately, the cleaved caspase 3 antibody did not work on mouse kidney samples.

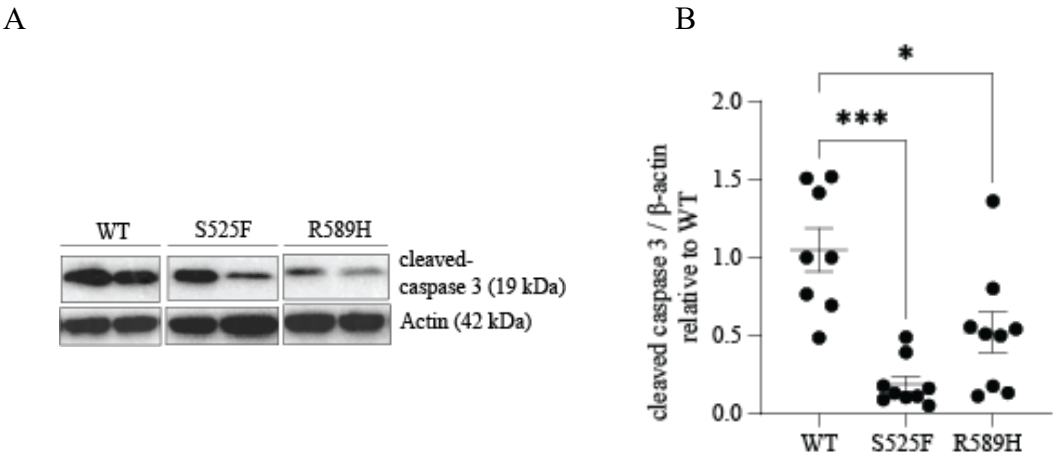

Figure 3.14. Cleaved caspase 3 abundance in mIMCD WT, S525F and R589H kAE1-HA. **(A)** Immunoblot of mIMCD WT, S525F and R589H cells treated with dox for 48hr prior to lysis with RIPA lysis buffer. Rabbit anti-cleaved caspase 3 antibody was used to detect cleaved caspase 3. **(B)** Graphical representation of blot shown in A. Error bars correspond to mean ± SEM, n= minimum 3. *P<0.05, ***P < 0.001 using one-way ANOVA with Dunnet's multiple comparison post hoc test.

Discussion

In this work, we showed that the autophagy process is altered in mIMCD3 cells expressing dominant and recessive kAE1 dRTA mutants. We provide evidence that expression of kAE1 mutants affect cytosolic pH, which could possibly be a cause for abnormal autophagy. We further show that in S525F and R589H mutant cells and homozygous Ae1 R607H kidneys, an increase in LC3BII ratio or abundance is observed. Cells expressing R295H dRTA mutant have more abundant phosphorylated 4E-BP1 and mTORC1 ratios than WT cells upon starvation. Finally, we show that S525F cells contain more functional lysosomes at steady state and that upon starvation, there is a further increase in lysosome numbers. R589H cells contain larger lysosomes at basal state, a characteristic that is reversed upon bafA1 treatment. Overall, our results support altered autophagy processes in cells expressing dRTA mutants, possibly caused by alkaline cytosolic pH.

In this work, we examined a variety of autophagy markers both *in vivo* and *in vitro*. In the Ae1 R607H dRTA mouse model, an accumulation of p62 and ubiquitin positive material in the remainder of A-ICs was reported(Mumtaz et al., 2017). Accumulation of p62 points to a block in autophagy and abnormal increases or decreases in autophagy result in autophagic cell death (Kang & Avery, 2008). It was hypothesized that the R607H variant may disrupt the normal trafficking of the H^+-ATPase and alter lysosome function, which results in defective autophagy and cell death (Mumtaz et al., 2017).

In this work, both *in vitro* and *in vivo* methods were used to study autophagy. mIMCD WT, R295H, S525F and R589H kAE1-HA cells were used to delineate autophagy in dRTA. kAE1 abundance in the cell lines varied: R295H had a lower abundance of kAE1 and S525F as well as R589H had a higher abundance of kAE1 compared to kAE1 WT. These differences may be due to differences in transection efficiency that could lead to a difference in abundance at the protein

level (Chong et al., 2021). Next, we looked at kAe1 abundance *in vivo* and there was no difference between $Ae1^{+/+}$, $Ae1^{R607H/R607H,}$ which contrast with previous publication(Mumtaz et al., 2017). Despite intra-cardiac perfusion, it is possible that some blood remained in the kidneys thus contaminating our quantification of kAe1 since our antibody cannot distinguish between eAe1 and kAe1 isoforms. R607H mice do have fewer alpha-intercalated cells and as a result have a lower abundance of kAe1 (Mumtaz et al., 2017). Next, we examined LC3B *in vitro* and *in vivo.*

Results from Chapter 3 are summarized in **Table 3.3.**

Overall, the functionally active R295H variant that results in autosomal recessive dRTA displays autophagy block. Interestingly, these cells have a decreased abundance of kAE1 and due to this reason, only three reliable experiments were performed for this mutant. These differences are maybe the result of infection efficiency, that may lead to a difference in abundance at the protein level (Chong et al., 2021). As such, initial experiments with evidence of kAE1 abundance are shown in **Figure 3.1**. To examine autophagy in the dRTA mutant cell lines, we assessed LC3B cleavage. We observed no difference in LC3BII/total LC3B ratio in this mutant. Additionally, neither BafA1 nor starvation affected the level of LC3BII. The lack of an effect of the treatments indicates that autophagy is altered in the mutant cell line as BafA1 should increase LC3BII (Yamamoto1 et al., 1998) and starvation should increase the conversion of LC3BI to LC3BII at short treatment times (of less than 1 hour) and decrease it for times beyond that (Mizushima & Yoshimori, 2007). Interestingly, this was the only mutant that had an increase in p62 abundance indicating autophagy suppression(Kuma et al., 2004). This mutant also had a significant increase in the phosphorylation of 4E-BP1 and mTOR phosphorylation compared to WT kAE1, indicating an autophagy block. The expected decreased phosphorylation of mTOR

and 4E-BP1 upon starvation was also observed. The expression of this mutant did not affect the size or number of lysosomes, however, when cells were starved, the number of lysosomes increased, also suggesting a blocked autophagy process. However, starvation decreased the size of the lysosomes. Taken together, the R295H mutant cells display a block in early autophagy which results in an accumulation of p62 and an increased phosphorylation of 4E-BP1 and mTOR. Because this mutant cannot acidify intracellularly to the same extent as its WT counterpart, it may have altered autophagy. These results, however, are based on a small sample size of 3 experiments and should be taken with caution.

We next examined the functionally defective S525F variant that also cannot acidify the cytosol to the same extent as WT. This mutant cell line also displays an autophagy block although it is different from the R295H variant. This mutant has a higher abundance of kAE1 compared to WT and this can be attributed to a better infection efficiency. These cells displayed an increased conversion of LC3BI to LC3BII which indicates an increase in autophagic flux or a block that prevents the fusion of the autophagosome with the lysosome, resulting in the accumulation of LC3BII. However, no increase in p62, phosphorylation of mTOR or 4E-BP1 was observed in contradiction with an early autophagy block. An increased number of lysosomes at steady state however was observed, which again favors an autophagy block as increased autophagy results in a decrease of lysosomes (Xu & Ren, 2015). Additionally, BafA1 did not affect any of the parameters for this variant except decreasing lysosome size which generally supports that either this mutant is already blocking late steps of autophagy at steady state or that blocking autophagy with BafA1 was not sufficient to decrease autophagy to a detectable level. On the other hand, inducing autophagy through starvation did decrease the level of 4E-BP1 phosphorylation, increased the lysosome number and had no other effect on the other parameters.

This means that these mutant cells are appropriately reacting to starvation, as a decrease in phosphorylated 4E-BP1 correlates with an increased autophagy(Gingras et al., 1998). I also examined apoptosis in this cell line and found a decrease in cleaved caspase 3 compared to WT, which could be linked to an alteration of cytosolic pH (Kazyken et al., 2021) but further studies will be needed to verify this as there was no change in p53 levels. Taken together, these results suggest that these cells may have a block of late steps of autophagic flux (lysosomal activity) based on the higher abundance of LC3BII and a higher number of lysosomes present in cells with kAE1 S525F.

Cells expressing the functionally active R589H variant, which also does not acidify the cytosol to the same extent as kAE1-WT, show an increase in autophagy which is not consistent with the findings Mumtaz and colleagues have reported in the equivalent mouse model. This variant cell line shows an increase in kAE1 abundance. Like the S525F variant, an increased conversion of LC3BI to LC3BII was observed at the steady state. This indicates a block in autophagy due to a failure to degrade LC3BII or an increase in autophagy as is the case of short-term starvation(Mizushima & Yoshimori, 2007), leading to an increase in LC3BII. The remainder of the parameters such as p62, p-4E-BP1, p-mTOR and lysosome number were not different in this variant cell line compared to WT. However, the size of the lysosomes were larger in this variant cell line, which points to an increased autophagy at steady state as autophagy activation leads to an increase in the size of lysosomes (Xu & Ren, 2015). An increase in LC3BII and an increase in the sizes of lysosomes together indicates an increase in autophagy(Xu & Ren, 2015). BafA1 treatment decreased LC3BII over total LC3B ratio in this variant which shows that it is possible to block autophagy in this variant. Additionally, starvation decreased the 4E-BP1 and mTOR phosphorylation which indicates that this variant is reacting to

autophagy activation as expected. Starvation also decreased the size of lysosomes in this variant. Similarly to the S525F expressing cell line, the R589H expressing cell line displays a decrease in cleaved caspase 3 levels compared to WT, which could be linked to an alteration of cytosolic pH (Kazyken et al., 2021). However, further studies will be needed as there was no change in p53 levels. Together, these results point to an appropriate regulation of autophagy flux but an abnormally activated autophagy at steady state in the R589H expressing cell line.

We next aimed to validate our findings *in vivo*. Whole kidney homogenates from the $Ae1^{R607H/R607H}$ mice showed an increase in total LC3B compared to WT mice, but no difference in the other parameters. Because the total amount of LC3B was increased in the KI mice, it is hard to delineate whether there is autophagy block or an increase in autophagy. Additionally, p62 levels were unchanged between $Ae1^{R607H/R607H}$ mice and $Ae1^{+/+}$ mice kidney homogenates. This is different to what Mumtaz and colleagues reported. They found an increase in p62 in the collecting ducts of the $Ae1^{R607H/R607H}$ mice by immunofluorescence in mouse kidney sections (Mumtaz et al., 2017). As I used immunoblots from kidney homogenates in my studies as opposed to isolated collecting ducts, it may have been difficult to detect changes in p62 since this protein is expressed ubiquitously, especially since these mice have fewer A-ICs. Additionally, no difference in AE1 abundance was observed between $Ae1^{+/+}$ or $Ae1^{R607H/R607H}$ whole kidneys, which could be attributed to the mouse anti-IVF-12s primary antibody detecting both kAe1 and red blood cell Ae1. Cardiac perfusion cannot guarantee that all the blood has been removed from the kidney (some also visibly contained more blood than others depending on perfusion efficiency), therefore this method has its limitations. Additionally, I used whole kidney lysates as opposed to isolated collecting ducts which could also explain this result. R6907H mice do have

fewer alpha-intercalated cells and as a result have a lower abundance of kAe1 (Mumtaz et al., 2017) but this was not apparent in the whole kidney lysate.

Our findings point towards defective autophagy mechanisms *in vivo* in transgenic mice and *in vitro* in mutant cells. They both indicate an autophagy block and an increase in autophagic flux for the kAE1-R589H variant which could result in the phenotypes that are seen in patients with dRTA. Physiological levels of autophagy are pro-survival, whereas insufficient or excessive levels of autophagy are pro-death. (Kang & Avery, 2008). Therefore, too much or too little of autophagy can lead to cell death as seen in dRTA mutant mice with reduced IC. It is important to understand what activating or inhibiting autophagy does and whether these methods could help restore normal functioning in the cells as well as the mice and eventually be translated to humans.

Table 3.3. Table summarizing results from Chapter 3. "-" Unaffected. "*" R295H variant had a small sample size of n=3.

	Parameter	BafA1treatment	Starvation	
WT	AE1	-	-	
	LC3BII	Decreased	Decreased	
	p62	Increased	Increased	
	p-4EBP1	-	Decreased	
	p-mTOR	-	-	
	Lysosome Number	-	-	
	Lysosome Size	-	-	
R295H*	Parameter	Steady State (vs WT)	BafA1treatment (vs steady state)	Starvation (vs steady state)
	AE1	-	-	-
	LC3BII	-	-	-
	p62	Increased	-	-
	p-4EBP1	Increased	-	-
	p-mTOR	Increased	Decreased	Decreased
	Lysosome Number	-	-	Increased
	Lysosome Size	-	-	Decreased
S525F	Parameter	Steady State (vs WT)	BafA1treatment (vs steady state)	Starvation (vs steady state)
	AE1	Increased	-	-
	LC3BII	Increased	-	-
	p62	-	-	-
	p-4EBP1	-	-	Decreased
	p-mTOR	-	-	-
	Lysosome Number	Increased	-	Increased
	Lysosome Size	-	Decreased	-
R589H	Parameter	Steady State (vs WT)	BafA1treatment (vs steady state)	Starvation (vs steady state)
	AE1	Increased	-	-
	LC3BII	Increased	Decreased	-
	p62	-	-	-
	p-4EBP1	-	-	Decreased
	p-mTOR	-	-	Decreased
	Lysosome Number	-	-	-
	Lysosome Size	Increased	-	Decreased
$Ae1^{R607H/R607H}$	Parameter	Steady State (vs $Ae1^{+/+}$)		
	AE1	-		
	Total LC3B	Increased		
	p62	-		

Chapter 4 General conclusion, limitations, and future directions

This Thesis was articulated around the study of 2 different membrane proteins causing two different inherited diseases.

In the first project (Chapter 2), in collaboration with New York's Pediatric Undiagnosed Diseases Program, we identified two novel mutations in the human high-affinity choline transporter 1 (CHT1) in a compound heterozygous patient with congenital myasthenic syndrome. I generated an *in vitro* cell model of both mutations using HEK cells. The CHT1 p.I294T was characterized by a lower CHT1 abundance with appropriate localization to the cell surface, a short half-life, and decreased activity that could be corrected if normalized for CHT1 concentration. On the other hand, CHT1 p.D349N displayed CHT1 overabundance with appropriate localization, had a similar half-life as CHT1 WT but was functionally inactive. The treatment regimen was altered for the patient to include acetylcholinesterase inhibitors which significantly improved the patient's quality of life.

There are several limitations to our work. First, I expressed EV, WT or mutant CHT1 in HEK 293 cells which are not the best cell model for muscles or nerves cells, however they do have properties of immature neuronal cell lines(Shaw et al., 2002). A very low level of endogenous CHT1 is present in HEK cells (Banerjee et al., 2019) which allowed us to study CHT1 mutations without the confounding effect of endogenous CHT1. However, there was some endogenous choline transport activity seen in EV (**Figure 2.3**) that was subtracted from the activity of the other variants.)

Additionally, immunofluorescence microscopy studies of the HEK cells were unreliable as it was difficult to visualize the localization of CHT1 in this cell line with reduced cytosolic volume and enlarged nuclei. Finally, there could have been a difference in transfection efficiencies between the mutants and WT CHT1 which could explain the difference in

abundance. However, the transport studies were corrected for protein concentration and CHT1 abundance. We could in the future use well established neuronal cells lines such as SH-SY5Y human neuroblastoma cells to study these mutations to better understand what is happening *in vivo.*

Because CHT1 I294T retained some activity at the lowest concentration (0.1 μM), we looked at the effect of small molecules on I294T CHT1 abundance we used chemical chaperones that rescue CFTR mutant proteins because CFTR is also a well-studied ion channel. Correctors VX 809 (Van Goor et al., 2011) and C3 (Peters et al., 1996; Van Goor et al., 2006) were used, as well as small molecules that activate CHT1 (MKC 231 (Takashina et al., 2008) and staurosporine (Choudhary et al., 2017)) and we assessed whether they would rescue p.I294T CHT1 mutant abundance and activity. None of these molecules increased the abundance of CHT1 I294T however staurosporine increased the ratio of glycosylated CHT1 but it was toxic to the cells so transport experiments were not possible at even 10 times less than the concentration published (Choudhary et al., 2017). It would be appropriate to screen for additional molecules that may influence CHT1 abundance and activity. Also, it would be interesting to assess the effect of MKC-231 on transport activity even though it did not increase CHT1 abundance.

Because the initial experiments revealed that the p.I294T CHT1 mutant possesses some residual activity, our collaborators prescribed pyridostigmine to the patient and observed significant improvement in their quality of life. This clinical observation validated our findings that abnormal CHT1 was the protein causing CMS in this patient.

Project 2 was extensive and allowed us to make a few interesting discoveries. Mumtaz and colleagues' findings of a potential role of autophagy and loss of intercalated cells in dRTA motivated us to delve into autophagy as a possible mechanism underlying the cell death observed

in dRTA mice with the R607H KI mutation. Their main findings were that these mice had fewer A-ICs, decreased apical relocation of the H^+-ATPase in the remainder of A-ICs, and accumulation of p62 and ubiquitin in intercalated cells (Mumtaz et al., 2017). These findings motivated us to study autophagy using mIMCD cells bearing WT, R295H, S525F and R589H kAE1 as an *in vitro* model of dRTA and R607H, the murine equivalent of human R589H dRTA mutant in the previously established $Ae1^{R607H/R607H}$ KI mice.

mIMCD cells originate from the collecting duct but lack endogenous kAE1 which make them a good model for studying dRTA. The choice of an appropriate cell model is important for deciphering cellular processes causing dRTA. For example, previous *in vitro* studies of dRTA used MDCK cells and these cells showed a mis trafficking of R589H kAE1. However, kAE1 R589H reached the plasma membrane when expressed in mIMCD cells. We also utilized a mouse model to study autophagy, which may provide more relevant knowledge at the level of the whole animal.

We observed differences in kAE1 abundance between the WT, R295H, S525F and R589H expressing cells. This can be attributed to differences in infection efficiency (Chong et al., 2021). Because mIMCD cells bearing kAE1 R295H had reduced kAE1 abundance, we only did a total of three separate experiments for this mutant. To circumvent this problem, we tried to prepare new cells carrying this mutant but were unsuccessful and therefore attempted cloning the few positive cells. The clones with the highest kAE1 expression, however, also lost kAE1 expression after a few passages, despite using an inducible expression system. The R295H mutant also had a lower kAE1 expression to begin with and this may be because the protein itself degrades prematurely or is unstable. It was shown to be functionally active when normalized to protein abundance. On the other hand, dRTA mutant S525F (functionally defective) and R589H

(functionally active) display significant kAE1 overabundance. Surprisingly, independent from their chloride/bicarbonate exchange activity, all the mutants were unable to acidify the cytosol to the same extent as kAE1 WT cells (**Figure 3.2)** and this maybe be the link between the autophagic defects that were observed. The reason for this abnormal cytosolic pH is unclear and may originate from an un-explained difference in intrinsic buffering capacity between WT and dRTA cell lines. More studies will be needed to fully understand this observation.

The $Ae1^{R607H/R607H}$ and the $Ae1^{+/+}$ mice kidneys had a similar level of Ae1 abundance even though these mice have been shown to have fewer A-ICs(Mumtaz et al., 2017). This is attributed to the fact that we used whole kidneys as opposed to isolated collecting ducts. In the future, it would be important to repeat these experiments using isolated collecting ducts. Additionally, we used the mouse anti-IVF-12s antibody which does not differentiate between red blood cell Ae1 and kAe1. Despite perfusion of the kidneys, the bands on the immunoblot in **Figure 3.1** are a summation of the Ae1 from the red blood cells retained in the kidney and kAe1 from the alpha intercalated cells. A specific antibody that detects mouse kAe1 would be ideal, although it does not exist. Studying isolated collecting ducts may minimize this issue.

We also looked at several autophagy markers in the mutants at steady state, under autophagy activation via starvation and autophagy block through bafA1. The R295H and S525F mutant cells displayed autophagy block, and R589H displayed autophagy activation. The $Ae1^{R607H/R607H}$ mice displayed an increase in total LC3B but it is not possible to conclude whether this was caused by autophagy activation or block. Although BafA1 usually increases LC3BII levels(Yamamoto1 et al., 1998), it was not apparent for the WT kAE1 cells for an unclear reason. Starvation has a dual effect: short term starvation of less than 1hr typically increases LC3BII, and long term decreases it (Mizushima & Yoshimori, 2007). This is an issue because it affects

the way the results are interpreted and thus multiple methods of studying autophagy must be used.

P62 levels are increased in the presence of bafA1 and decrease after starvation. Phosphorylation of 4E-BP1 at serine 65 and mTOR at serine 2448 indicate autophagy block and thus after bafA1, they should increase and decrease after starvation. However, these parameters are dynamic, and their levels may not truly represent what is happening at the time of the experiment. To take our analysis further, we looked at the size and number of lysosomes in the cell models using Magic red staining, however, this method also showed high variability. This variability could originate from the manual but blinded method of counting lysosome number and size. One way to combat these limitations is to complete our analysis by assessing autophagy flux in real time via live cell imaging using the eGFP-RFP-LC3B construct and using it to quantify the number of autophagosomes and autolysosomes (Kaizuka et al., 2016). The acidic pH of the lysosomes quenches the GFP fluorescence without affecting RFP fluorescence, thus allowing counting of red versus yellow puncta. Nonacidic autophagosomes will appear as yellow puncta. Although I attempted this experiment several times, more troubleshooting is necessary, and this is a work in progress by other graduate students in our lab.

In summary, our work shows abnormalities in autophagy in dRTA in both *in vitro* and *in vivo*. It is important to understand the underlying cell death mechanisms in dRTA as it leads to chronic kidney disease which is detrimental to health and wellbeing.

In this thesis, I provided two examples of bench to bedside research, with the first project having made a difference in the well-being of a patient. Finally, many rare diseases still require basic research to understand the underlying molecular mechanisms causing the defect(s) and find

individualized treatment plans for each case. In the future, patients would benefit from a systematized approach to understanding such rare diseases.

Bibliography

Al-Awqati, Q. (1996). Plasticity in epithelial polarity of renal intercalated cells: targeting of the H(+)-ATPase and band 3. *The American Journal of Physiology*, *270*(6 Pt 1). https://doi.org/10.1152/AJPCELL.1996.270.6.C1571

Alper, S. L., Natale, J., Gluck, S., Lodish, H. F., & Brown, D. (1989). Subtypes of intercalated cells in rat kidney collecting duct defined by antibodies against erythroid band 3 and renal vacuolar H+-ATPase. *Proceedings of the National Academy of Sciences of the United States of America*, *86*(14), 5429–5433. https://doi.org/10.1073/PNAS.86.14.5429

Andrews, P. M., & Porter, K. R. (1974). A scanning electron microscopic study of the nephron. *American Journal of Anatomy*, *140*(1), 81–115. https://doi.org/10.1002/AJA.1001400107

Apparsundaram, S., Ferguson, S. M., George, A. L., & Blakely, R. D. (2000). Molecular Cloning of a Human, Hemicholinium-3-Sensitive Choline Transporter. *Biochemical and Biophysical Research Communications*, *276*(3), 862–867. https://doi.org/10.1006/bbrc.2000.3561

Arakawa, T., Kobayashi-Yurugi, T., Alguel, Y., Iwanari, H., Hatae, H., Iwata, M., Abe, Y., Hino, T., Ikeda-Suno, C., Kuma, H., Kang, D., Murata, T., Hamakubo, T., Cameron, A. D., Kobayashi, T., Hamasaki, N., & Iwata, S. (2015). Crystal structure of the anion exchanger domain of human erythrocyte band 3. *Science*, *350*(6261), 680–684. https://doi.org/10.1126/science.aaa4335

Balgi, A. D., Diering, G. H., Donohue, E., Lam, K. K. Y., Fonseca, B. D., Zimmerman, C., Numata, M., & Roberge, M. (2011). Regulation of mTORC1 Signaling by pH. *PLOS ONE*, *6*(6), e21549. https://doi.org/10.1371/JOURNAL.PONE.0021549

Banerjee, M., Arutyunov, D., Brandwein, D., Janetzki-Flatt, C., Kolski, H., Hume, S., Leonard, N. J., Watt, J., Lacson, A., Baradi, M., Leslie, E. M., Cordat, E., & Caluseriu, O. (2019). The novel p.Ser263Phe mutation in the human high-affinity choline transporter 1 (CHT1/SLC5A7) causes a lethal form of fetal akinesia syndrome. *Human Mutation*, *40*(10). https://doi.org/10.1002/humu.23828

Banerjee, M., Marensi, V., Conseil, G., Le, X. C., Cole, S. P. C., & Leslie, E. M. (2016). Polymorphic variants of MRP4/ABCC4 differentially modulate the transport of methylated arsenic metabolites and physiological organic anions. *Biochemical Pharmacology*, *120*, 72–82. https://doi.org/10.1016/J.BCP.2016.09.016

Barwick, K. E. S., Wright, J., Al-Turki, S., McEntagart, M. M., Nair, A., Chioza, B., Al-Memar, A., Modarres, H., Reilly, M. M., Dick, K. J., Ruggiero, A. M., Blakely, R. D., Hurles, M. E., & Crosby, A. H. (2012). Defective presynaptic choline transport underlies hereditary motor neuropathy. *American Journal of Human Genetics*, *91*(6), 1103–1107. https://doi.org/10.1016/J.AJHG.2012.09.019

Bauché, S., O'Regan, S., Azuma, Y., Laffargue, F., McMacken, G., Sternberg, D., Brochier, G., Buon, C., Bouzidi, N., Topf, A., Lacène, E., Remerand, G., Beaufrere, A.-M. M., Pebrel-Richard, C., Thevenon, J., El Chehadeh-Djebbar, S., Faivre, L., Duffourd, Y., Ricci, F., … Nicole, S. (2016). Impaired Presynaptic High-Affinity Choline Transporter Causes a Congenital Myasthenic Syndrome with Episodic Apnea. In *American Journal of Human Genetics* (Vol. 99, Issue 3). https://doi.org/10.1016/j.ajhg.2016.06.033

Bazalakova, M. H., & Blakely, R. D. (2006). The high-affinity choline transporter: a critical protein for sustaining cholinergic signaling as revealed in studies of genetically altered mice. *Handbook of Experimental Pharmacology*, *175*(175), 525–544. https://doi.org/10.1007/3-540-29784-7_21

Black, S. A. G., Ribeiro, F. M., Ferguson, S. S. G., & Rylett, R. J. (2010). Rapid, transient effects of the protein kinase C activator phorbol 12-myristate 13-acetate on activity and trafficking of the rat high-affinity choline transporter. *Neuroscience*, *167*(3), 765–773. https://doi.org/10.1016/j.neuroscience.2010.02.026

Brosius, F. C., Alper, S. L., Garcia, A. M., & Lodish, H. F. (1989). The major kidney band 3 gene transcript predicts an amino-terminal truncated band 3 polypeptide. *Journal of Biological Chemistry*, *264*(14), 7784–7787. https://doi.org/10.1016/S0021-9258(18)83108-8

Cabantchik, Z. I., & Rothstein, A. (1974). Membrane Proteins Related to Anion Permeability of Human Red Blood Cells I. Localization of Disulfonic Stilbene Binding Sites in Proteins Involved in Permeation. In *J. Membrane Biol* (Vol. 15).

Chertow, G., Luyckx, V., Marsden, P., Skorecki, K., Taal, M., & Yu, A. (2019). *Brenner and Rector's The Kidney, 2-Volume Set - 11th Edition*. https://www.elsevier.com/books/brenner-and-rectors-the-kidney-2-volume-set/yu/978-0-323-53265-5

Chong, Z. X., Yeap, S. K., & Ho, W. Y. (2021). Transfection types, methods and strategies: A technical review. *PeerJ*, *9*. https://doi.org/10.7717/PEERJ.11165/SUPP-1

Choudhary, P., Armstrong, E. J., Jorgensen, C. C., Piotrowski, M., Barthmes, M., Torella, R., Johnston, S. E., Maruyama, Y., Janiszewski, J. S., Storer, R. I., Skerratt, S. E., & Benn, C. L. (2017). Discovery of Compounds that Positively Modulate the High Affinity Choline Transporter. *Frontiers in Molecular Neuroscience*, *10*, 40. https://doi.org/10.3389/fnmol.2017.00040

Cooke, L. J., & Rylett, R. J. (1997). Inhibitors of serine/threonine phosphatases increase membrane-bound choline acetyltransferase activity and enhance acetylcholine synthesis. *Brain Research*, *751*(2), 232–238.

Cordat, E., Kittanakom, S., Yenchitsomanus, P. T., Li, J., Du, K., Lukacs, G. L., & Reithmeier, R. A. F. (2006). Dominant and recessive distal renal tubular acidosis mutations of kidney anion exchanger 1 induce distinct trafficking defects in MDCK cells. *Traffic (Copenhagen, Denmark)*, *7*(2), 117–128. https://doi.org/10.1111/J.1600-0854.2005.00366.X

Costantini, F., & Kopan, R. (2010). Patterning a complex organ: branching morphogenesis and nephron segmentation in kidney development. *Developmental Cell*, *18*(5), 698. https://doi.org/10.1016/J.DEVCEL.2010.04.008

de Araujo, M. E. G., Liebscher, G., Hess, M. W., & Huber, L. A. (2020). Lysosomal size matters. *Traffic*, *21*(1), 60–75. https://doi.org/10.1111/TRA.12714/

Dressler, G. (2006). The Cellular Basis of Kidney Development . *Article in Annual Review of Cell and Developmental Biology*. https://doi.org/10.1146/annurev.cellbio.22.010305.104340

Eknoyan, G. (1989). The Origins of Nephrology – Galen, the Founding Father of Experimental Renal Physiology. *American Journal of Nephrology*, *9*(1), 66–82. https://doi.org/10.1159/000167939

Engel, A. G. (2017). Congenital Myasthenic Syndromes in 2018. *Current Neurology and Neuroscience Reports*, *18*(8). https://doi.org/10.1007/S11910-018-0852-4

Engel, A. G. (2018). Congenital Myasthenic Syndromes in 2018. *Current Neurology and Neuroscience Reports*, *18*(8). https://doi.org/10.1007/S11910-018-0852-4

Engel, A. G., Shen, X. M., Selcen, D., & Sine, S. M. (2015). Congenital myasthenic syndromes: Pathogenesis, diagnosis, and treatment. *The Lancet Neurology*, *14*(4), 420–434. https://doi.org/10.1016/S1474-4422(14)70201-7

English, B. A., Appalsamy, M., Diedrich, A., Ruggiero, A. M., Lund, D., Wright, J., Keller, N.

R., Louderback, K. M., Robertson, D., & Blakely, R. D. (2010). Tachycardia, reduced vagal capacity, and age-dependent ventricular dysfunction arising from diminished expression of the presynaptic choline transporter. *American Journal of Physiology - Heart and Circulatory Physiology*, *299*(3). https://doi.org/10.1152/AJPHEART.00170.2010

English, B. A., Hahn, M. K., Gizer, I. R., Mazei-Robison, M., Steele, A., Kurnik, D. M., Stein, M. A., Waldman, I. D., & Blakely, R. D. (2009). Choline transporter gene variation is associated with attention-deficit hyperactivity disorder. *Journal of Neurodevelopmental Disorders*, *1*(4), 252. https://doi.org/10.1007/S11689-009-9033-8

Ferguson, S. M., Bazalakova, M., Savchenko, V., Tapia, J. C., Wright, J., & Blakely, R. D. (2004a). Lethal impairment of cholinergic neurotransmission in hemicholinium-3-sensitive choline transporter knockout mice. *Proceedings of the National Academy of Sciences*, *101*(23), 8762–8767. https://doi.org/10.1073/pnas.0401667101

Ferguson, S. M., Bazalakova, M., Savchenko, V., Tapia, J. C., Wright, J., & Blakely, R. D. (2004b). Lethal impairment of cholinergic neurotransmission in hemicholinium-3-sensitive choline transporter knockout mice. *Proceedings of the National Academy of Sciences of the United States of America*, *101*(23), 8762–8767. https://doi.org/10.1073/PNAS.0401667101

Ferguson, S. M., Savchenko, V., Apparsundaram, S., Zwick, M., Wright, J., Heilman, C. J., Yi, H., Levey, A. I., & Blakely, R. D. (2003). Vesicular Localization and Activity-Dependent Trafficking of Presynaptic Choline Transporters. *The Journal of Neuroscience*, *23*(30), 9697 LP – 9709. https://doi.org/10.1523/JNEUROSCI.23-30-09697.2003

Finberg, K. E., Wagner, G. A., Bailey, M. A., Păunescu, T. G., Breton, S., Brown, D., Giebisch, G., Geibel, J. P., & Lifton, R. P. (2005). The B1-subunit of the H+ ATPase is required for maximal urinary acidification. *Proceedings of the National Academy of Sciences of the United States of America*, *102*(38), 13616–13621. https://doi.org/10.1073/pnas.0506769102

Gao, X. B., Eladari, D., Leviel, F., Tew, B. Y., Miró-Julià, C., Cheema, F., Miller, L., Nelson, R., Păunescu, T. G., McKee, M., Brown, D., & Al-Awqati, Q. (2010). Deletion of hensin/DMBT1 blocks conversion of β- To α-intercalated cells and induces distal renal tubular acidosis. *Proceedings of the National Academy of Sciences of the United States of America*, *107*(50), 21872–21877. https://doi.org/10.1073/PNAS.1010364107/-/DCSUPPLEMENTAL

Gates, J., Ferguson, S. M., Blakely, R. D., & Apparsundaram, S. (2004). Regulation of Choline Transporter Surface Expression and Phosphorylation by Protein Kinase C and Protein Phosphatase 1/2A. *Journal of Pharmacology and Experimental Therapeutics*, *310*(2), 536–545. https://doi.org/10.1124/jpet.104.066795

Gillies, A. R., & Lieber, R. L. (2011). Structure and function of the skeletal muscle extracellular matrix. In *Muscle and Nerve* (Vol. 44, Issue 3, pp. 318–331). https://doi.org/10.1002/mus.22094

Gingras, A. C., Kennedy, S. G., O'Leary, M. A., Sonenberg, N., & Hay, N. (1998). 4E-BP1, a repressor of mRNA translation, is phosphorylated and inactivated by the Akt(PKB) signaling pathway. *Genes and Development*, *12*(4), 502–513. https://doi.org/10.1101/gad.12.4.502

Haga, T. (2014). Molecular properties of the high-affinity choline transporter CHT1. In *Journal of Biochemistry* (Vol. 156, Issue 4, pp. 181–194). https://doi.org/10.1093/jb/mvu047

Haga, T., & Noda, H. (1973). Choline uptake systems of rat brain synaptosomes. *Biochimica et Biophysica Acta (BBA) - Biomembranes*, *291*(2), 564–575. https://doi.org/10.1016/0005-2736(73)90508-7

Hartleben, B., Gödel, M., Meyer-Schwesinger, C., Liu, S., Ulrich, T., Köbler, S., Wiech, T., Grahammer, F., Arnold, S. J., Lindenmeyer, M. T., Cohen, C. D., Pavenstädt, H., Kerjaschki, D., Mizushima, N., Shaw, A. S., Walz, G., & Huber, T. B. (2010). Autophagy influences glomerular disease susceptibility and maintains podocyte homeostasis in aging mice. *The Journal of Clinical Investigation*, *120*(4), 1084–1096. https://doi.org/10.1172/JCI39492

Issa, A. M., Gauthier, S., & Collier, B. (1996). Effects of the phosphatase inhibitors calyculin A and okadaic acid on acetylcholine synthesis and content of rat hippocampal formation. *Journal of Neurochemistry*, *66*(5), 1924–1932.

Jarolim, P., Shayakul, C., Prabakaran, D., Jiang, L., Stuart-Tilley, A., Rubin, H. L., Simova, S., Zavadil, J., Herrin, J. T., Brouillette, J., Somers, M. J. G., Seemanova, E., Brugnara, C., Guay-Woodford, L. M., & Alper, S. L. (1998). Autosomal dominant distal renal tubular acidosis is associated in three families with heterozygosity for the R589H mutation in the AE1 (band 3) Cl-/HCO3- exchanger. *The Journal of Biological Chemistry*, *273*(11), 6380–6388. https://doi.org/10.1074/JBC.273.11.6380

Jumper, J., Evans, R., Pritzel, A., Green, T., Figurnov, M., Ronneberger, O., Tunyasuvunakool, K., Bates, R., Žídek, A., Potapenko, A., Bridgland, A., Meyer, C., Kohl, S. A. A., Ballard, A. J., Cowie, A., Romera-Paredes, B., Nikolov, S., Jain, R., Adler, J., … Hassabis, D. (2021). Highly accurate protein structure prediction with AlphaFold. *Nature 2021 596:7873*, *596*(7873), 583–589. https://doi.org/10.1038/s41586-021-03819-2

Kabeya, Y., Mizushima, N., Ueno, T., Yamamoto, A., Kirisako, T., Noda, T., Kominami, E., Ohsumi, Y., & Yoshimori, T. (2000). LC3, a mammalian homologue of yeast Apg8p, is localized in autophagosome membranes after processing. *The EMBO Journal*, *19*(21), 5720. https://doi.org/10.1093/EMBOJ/19.21.5720

Kaizuka, T., Morishita, H., Hama, Y., Tsukamoto, S., Matsui, T., Toyota, Y., Kodama, A., Ishihara, T., Mizushima, T., & Mizushima, N. (2016). An Autophagic Flux Probe that Releases an Internal Control. *Molecular Cell*, *64*(4), 835–849. https://doi.org/10.1016/J.MOLCEL.2016.09.037

Kang, C., & Avery, L. (2008). To be or not to be, the level of autophagy is the question: Dual roles of autophagy in the survival response to starvation. *Autophagy*, *4*(1), 82. https://doi.org/10.4161/AUTO.5154

Karczewski, K. J., Francioli, L. C., Tiao, G., Cummings, B. B., Alföldi, J., Wang, Q., Collins, R. L., Laricchia, K. M., Ganna, A., Birnbaum, D. P., Gauthier, L. D., Brand, H., Solomonson, M., Watts, N. A., Rhodes, D., Singer-Berk, M., England, E. M., Seaby, E. G., Kosmicki, J. A., … MacArthur, D. G. (2020). The mutational constraint spectrum quantified from variation in 141,456 humans. *Nature 2020 581:7809*, *581*(7809), 434–443. https://doi.org/10.1038/s41586-020-2308-7

Karet, F. E., Gainza, F. J., Györy, A. Z., Unwin, R. J., Wrong, O., Tanner, M. J. A., Nayir, A., Alpay, H., Santos, F., Hulton, S. A., Bakkaloglu, A., Ozen, S., Cunningham, M. J., Di Pietro, A., Walker, W. G., & Lifton, R. P. (1998a). Mutations in the chloride-bicarbonate exchanger gene AE1 cause autosomal dominant but not autosomal recessive distal renal tubular acidosis. *Proceedings of the National Academy of Sciences*, *95*(11), 6337–6342. https://doi.org/10.1073/PNAS.95.11.6337

Karet, F. E., Gainza, F. J., Györy, A. Z., Unwin, R. J., Wrong, O., Tanner, M. J. A., Nayir, A., Alpay, H., Santos, F., Hulton, S. A., Bakkaloglu, A., Ozen, S., Cunningham, M. J., Di Pietro, A., Walker, W. G., & Lifton, R. P. (1998b). Mutations in the chloride-bicarbonate

exchanger gene AE1 cause autosomal dominant but not autosomal recessive distal renal tubular acidosis. *Proceedings of the National Academy of Sciences*, *95*(11), 6337–6342. https://doi.org/10.1073/PNAS.95.11.6337

Kazyken, D., Lentz, S. I., & Fingar, D. C. (2021). Alkaline intracellular pH (pHi) activates AMPK-mTORC2 signaling to promote cell survival during growth factor limitation. *Journal of Biological Chemistry*, *297*, 101100. https://doi.org/10.1016/j.jbc.2021.101100

Kuhar, M. J., Sethy, V. H., Roth, R. H., & Aghajanian, G. K. (1973). CHOLINE: SELECTIVE ACCUMULATION BY CENTRAL CHOLINERGIC NEURONS. *Journal of Neurochemistry*, *20*(2), 581–593. https://doi.org/10.1111/J.1471-4159.1973.TB12157.X

Kuma, A., Hatano, M., Matsui, M., Yamamoto, A., Nakaya, H., Yoshimori, T., Ohsumi, Y., Tokuhisa, T., & Mizushima, N. (2004). The role of autophagy during the early neonatal starvation period. *Nature 2004 432:7020*, *432*(7020), 1032–1036. https://doi.org/10.1038/nature03029

Lashhab, R. (2021). *Characterizing The Role of The Chloride/Bicarbonate Exchanger AE1 in Modulating Tight Junction Properties in Renal Collecting Duct Cells*. https://doi.org/10.7939/R3-S7B0-ET70

Lashhab, R., Rumley, A. C., Arutyunov, D., Rizvi, M., You, C., Dimke, H., Touret, N., Zimmermann, R., Jung, M., Chen, X. Z., Alexander, T., & Cordat, E. (2019). The kidney anion exchanger 1 affects tight junction properties via claudin-4. *Scientific Reports*, *9*(1). https://doi.org/10.1038/S41598-019-39430-9

Li, H., & Durbin, R. (2009). Fast and accurate short read alignment with Burrows-Wheeler transform. *Bioinformatics (Oxford, England)*, *25*(14), 1754–1760. https://doi.org/10.1093/BIOINFORMATICS/BTP324

Lin, M. J., & Yu, B. P. (2018). Upregulation of the high-affinity choline transporter in colon relieves stress-induced hyperalgesia. *Journal of Pain Research*, *11*, 1971. https://doi.org/10.2147/JPR.S164186

Lin, T. A., Wu, V. C. C., & Wang, C. Y. (2019). Autophagy in chronic kidney diseases. In *Cells* (Vol. 8, Issue 1). https://doi.org/10.3390/cells8010061

Liu, W. J., Ye, L., Huang, W. F., Guo, L. J., Xu, Z. G., Wu, H. L., Yang, C., & Liu, H. F. (2016). p62 links the autophagy pathway and the ubiqutin-proteasome system upon ubiquitinated protein degradation. In *Cellular and Molecular Biology Letters* (Vol. 21, Issue 1). https://doi.org/10.1186/s11658-016-0031-z

Lockman, P. R., & Allen, D. D. (2002). The transport of choline. *Drug Development and Industrial Pharmacy*, *28*(7), 749–771. https://doi.org/10.1081/DDC-120005622

Luo, D., Chen, L., & Yu, B. (2017). Inhibition of the high affinity choline transporter enhances hyperalgesia in a rat model of chronic pancreatitis. *Biochemical and Biophysical Research Communications*, *488*(1), 204–210. https://doi.org/10.1016/J.BBRC.2017.05.036

Madsen, K. M., Verlander, J. W., & Tisher, C. C. (1988). Relationship between structure and function in distal tubule and collecting duct. *Journal of Electron Microscopy Technique*, *9*(2), 187–208. https://doi.org/10.1002/JEMT.1060090206

Matthies, D. S., Fleming, P. A., Wilkes, D. M., & Blakely, R. D. (2006). The Caenorhabditis elegans Choline Transporter CHO-1 Sustains Acetylcholine Synthesis and Motor Function in an Activity-Dependent Manner. *Journal of Neuroscience*, *26*(23), 6200–6212. https://doi.org/10.1523/JNEUROSCI.5036-05.2006

Medicine, J. (2017). *Autophagy | Macroautophagy & Importance in Health - YouTube*. https://www.youtube.com/watch?v=UmSVKzHc5yA

Mizushima, N., & Komatsu, M. (2011). Autophagy: Renovation of cells and tissues. *Cell*, *147*(4), 728–741. https://doi.org/10.1016/J.CELL.2011.10.026

Mizushima, N., Ohsumi, Y., & Yoshimori, T. (2002). Autophagosome Formation in Mammalian Cells. *CELL STRUCTURE AND FUNCTION*, *27*, 421–429.

Mizushima, N., & Yoshimori, T. (2007). How to Interpret LC3 Immunoblotting. *Autophagy*, *542*(6). https://doi.org/10.4161/auto.4600

Mort, J. S., & Buttle, D. J. (1997). Cathepsin B. *The International Journal of Biochemistry & Cell Biology*, *29*(5), 715–720. https://doi.org/10.1016/S1357-2725(96)00152-5

Mumtaz, R., Trepiccione, F., Hennings, J. C., Huebner, A. K., Serbin, B., Picard, N., Ullah, A. K. M. S., Păunescu, T. G., Capen, D. E., Lashhab, R. M., Mouro-Chanteloup, I., Alper, S. L., Wagner, C. A., Cordat, E., Brown, D., Eladari, D., & Hübner, C. A. (2017). Intercalated Cell Depletion and Vacuolar H⁺-ATPase Mistargeting in an Ae1 R607H Knockin Model. *Journal of the American Society of Nephrology*, *28*(5), 1507 LP – 1520. https://doi.org/10.1681/ASN.2016020169

Neumann, S. A., Linder, K. J., Muldoon, M. F., Sutton-Tyrrell, K., Kline, C., Shrader, C. J., Lawrence, E. C., Ferrell, R. E., & Manuck, S. B. (2012). Polymorphic variation in choline transporter gene (CHT1) is associated with early, subclinical measures of carotid atherosclerosis in humans. *The International Journal of Cardiovascular Imaging*, *28*(2), 243. https://doi.org/10.1007/S10554-011-9831-4

Nicholson, J. K. (1982). The microanatomy of the distal tubules, collecting tubules and collecting ducts of the starling kidney. *Journal of Anatomy*, *134*(Pt 1), 11. /pmc/articles/PMC1167933/?report=abstract

Nishimune, H., & Shigemoto, K. (2018). Practical Anatomy of the Neuromuscular Junction in Health and Disease. *Neurologic Clinics*, *36*(2), 231–240. https://doi.org/10.1016/J.NCL.2018.01.009

Norgett, E. E., Golder, Z. J., Lorente-Cánovas, B., Ingham, N., Steel, K. P., & Frankl, F. E. K. (2012a). Atp6v0a4 knockout mouse is a model of distal renal tubular acidosis with hearing loss, with additional extrarenal phenotype. *Proceedings of the National Academy of Sciences of the United States of America*, *109*(34), 13775–13780. https://doi.org/10.1073/PNAS.1204257109/SUPPL_FILE/PNAS.201204257SI.PDF

Norgett, E. E., Golder, Z. J., Lorente-Cánovas, B., Ingham, N., Steel, K. P., & Frankl, F. E. K. (2012b). Atp6v0a4 knockout mouse is a model of distal renal tubular acidosis with hearing loss, with additional extrarenal phenotype. *Proceedings of the National Academy of Sciences of the United States of America*, *109*(34), 13775–13780. https://doi.org/10.1073/PNAS.1204257109/SUPPL_FILE/PNAS.201204257SI.PDF

Ojiakor, O. A., & Rylett, R. J. (2020). Modulation of sodium-coupled choline transporter CHT function in health and disease. *Neurochemistry International*, *140*, 104810. https://doi.org/10.1016/J.NEUINT.2020.104810

Okuda, T., & Haga, T. (2003). High-affinity choline transporter. *Neurochemical Research*, *28*(3–4), 483–488. https://doi.org/10.1023/A:1022809003997

Okuda, T., Haga, T., Kanai, Y., Endou, H., Ishihara, T., & Katsura, I. (2000). Identification and characterization of the high-affinity choline transporter. *Nature Neuroscience*, *3*(2), 120–125. https://doi.org/10.1038/72059

Okuda, T., Osawa, C., Yamada, H., Hayashi, K., Nishikawa, S., Ushio, T., Kubo, Y., Satou, M., Ogawa, H., & Haga, T. (2012). Transmembrane topology and oligomeric structure of the high-affinity choline transporter. *Journal of Biological Chemistry*, *287*(51), 42826–42834.

https://doi.org/10.1074/JBC.M112.405027
Ordonez, N. G., & Spargo, B. H. (1976). The morphologic relationship of light and dark cells of the collecting tubule in potassium depleted rats. *American Journal of Pathology*, *84*(2), 317–326.
Pardal-Fernández, J. M., Carrascosa-Romero, M. C., Álvarez, S., Medina-Monzón, M. C., Caamaño, M. B., & de Cabo, C. (2018). A new severe mutation in the SLC5A7 gene related to congenital myasthenic syndrome type 20. *Neuromuscular Disorders*, *28*(10), 881–884. https://doi.org/10.1016/J.NMD.2018.06.020
Patton, B. L. (2003). Basal lamina and the organization of neuromuscular synapses. *Journal of Neurocytology 2003 32:5*, *32*(5), 883–903. https://doi.org/10.1023/B:NEUR.0000020630.74955.19
Pause, A., Belsham, G. J., Gingras, A. C., Donzé, O., Lin, T. A., Lawrence, J. C., & Sonenberg, N. (1994). Insulin-dependent stimulation of protein synthesis by phosphorylation of a regulator of 5'-cap function. *Nature*, *371*(6500), 762–767. https://doi.org/10.1038/371762A0
Payette, D. J., Xie, J., & Guo, Q. (2007). Reduction in CHT1-mediated choline uptake in primary neurons from presenilin-1 M146V mutant knock-in mice. *Brain Research*, *1135*(1), 12. https://doi.org/10.1016/J.BRAINRES.2006.12.005
Pearce, D., Soundararajan, R., Trimpert, C., Kashlan, O. B., Deen, P. M. T., & Kohan, D. E. (2015). Collecting Duct Principal Cell Transport Processes and Their Regulation. *Clinical Journal of the American Society of Nephrology : CJASN*, *10*(1), 135. https://doi.org/10.2215/CJN.05760513
Peters, L. L., Shivdasani, R. A., Liu, S. C., Hanspal, M., John, K. M., Gonzalez, J. M., Brugnara, C., Gwynn, B., Mohandas, N., Alper, S. L., Orkin, S. H., & Lux, S. E. (1996). Anion exchanger 1 (band 3) is required to prevent erythrocyte membrane surface loss but not to form the membrane skeleton. *Cell*, *86*(6), 917–927.
Pollak, M. R., Quaggin, S. E., Hoenig, M. P., & Dworkin, L. D. (2014). Renal Physiology The Glomerulus: The Sphere of Influence The Glomerulus. *Clin J Am Soc Nephrol*, *9*, 1461–1469. https://doi.org/10.2215/CJN.09400913
Purkerson, J. M., Tsuruoka, S., Suter, D. Z., Nakamori, A., & Schwartz, G. J. (2010). Adaptation to metabolic acidosis and its recovery are associated with changes in anion exchanger distribution and expression in the cortical collecting duct. *Kidney International*, *78*(10), 993. https://doi.org/10.1038/KI.2010.195
Reithmeier, R. A. F., Casey, J. R., Kalli, A. C., Sansom, M. S. P., Alguel, Y., & Iwata, S. (2016). Band 3, the human red cell chloride/bicarbonate anion exchanger (AE1, SLC4A1), in a structural context. *Biochimica et Biophysica Acta (BBA) - Biomembranes*, *1858*(7), 1507–1532. https://doi.org/10.1016/J.BBAMEM.2016.03.030
Rentzsch, P., Witten, D., Cooper, G. M., Shendure, J., & Kircher, M. (2019). CADD: predicting the deleteriousness of variants throughout the human genome. *Nucleic Acids Research*, *47*(D1), D886–D894. https://doi.org/10.1093/NAR/GKY1016
Reshkin, S. J., Bellizzi, A., Caldeira, S., Albarani, V., Malanchi, I., Poignee, M., Alunni-Fabbroni, M., Casavola, V., & Tommasino, M. (2000). Na /H exchanger-dependent intracellular alkalinization is an early event in malignant transformation and plays an essential role in the development of subsequent transformation-associated phenotypes. *FASEB J*, *14*, 2185–2197.
Ribeiro, F. M., Black, S. A. G., Prado, V. F., Rylett, R. J., Ferguson, S. S. G., & Prado, M. A. M.

(2006). The “ins” and “outs” of the high-affinity choline transporter CHT1. *Journal of Neurochemistry*, *97*(1), 1–12. https://doi.org/10.1111/j.1471-4159.2006.03695.x

Richards, S., Aziz, N., Bale, S., Bick, D., Das, S., Gastier-Foster, J., Grody, W. W., Hegde, M., Lyon, E., Spector, E., Voelkerding, K., & Rehm, H. L. (2015). Standards and guidelines for the interpretation of sequence variants: a joint consensus recommendation of the American College of Medical Genetics and Genomics and the Association for Molecular Pathology. *Genetics in Medicine 2015 17:5*, *17*(5), 405–423. https://doi.org/10.1038/gim.2015.30

Rieg, T., Vallon, V., Sausbier, M., Sausbier, U., Kaissling, B., Ruth, P., & Osswald, H. (2007). The role of the BK channel in potassium homeostasis and flow-induced renal potassium excretion. *Kidney International*, *72*(5), 566–573. https://doi.org/10.1038/SJ.KI.5002369

Rodríguez Cruz, P. M., Hughes, I., Manzur, A., Munot, P., Ramdas, S., Wright, R., Breen, C., Pitt, M., Pagnamenta, A. T., Taylor, J. C., Palace, J., & Beeson, D. (2021). Presynaptic congenital myasthenic syndrome due to three novel mutations in SLC5A7 encoding the sodium-dependant high-affinity choline transporter. *Neuromuscular Disorders*, *31*(1), 21–28. https://doi.org/10.1016/J.NMD.2020.10.006

Rosner, M., Siegel, N., Valli, A., Fuchs, C., & Hengstschläger, M. (2010). MTOR phosphorylated at S2448 binds to raptor and rictor. *Amino Acids*, *38*(1), 223–228. https://doi.org/10.1007/s00726-008-0230-7

Roy, A., Al-Bataineh, M. M., & Pastor-Soler, N. M. (2015). Renal Physiology Collecting Duct Intercalated Cell Function and Regulation. *Clin J Am Soc Nephrol*, *10*, 305–324. https://doi.org/10.2215/CJN.08880914

Rylett, R. J., & Schmidt, B. M. (1993). Regulation of the synthesis of acetylcholine. *Progress in Brain Research*, *98*(C), 161–166. https://doi.org/10.1016/S0079-6123(08)62394-8

Sabolić, I., Brown, D., Gluck, S. L., & Alper, S. L. (1997). Regulation of AE1 anion exchanger and H(+)-ATPase in rat cortex by acute metabolic acidosis and alkalosis. *Kidney International*, *51*(1), 125–137. https://doi.org/10.1038/KI.1997.16

Salter, C. G., Beijer, D., Hardy, H., Barwick, K. E. S., Bower, M., Mademan, I., De Jonghe, P., Deconinck, T., Russell, M. A., McEntagart, M. M., Chioza, B. A., Blakely, R. D., Chilton, J. K., De Bleecker, J., Baets, J., Baple, E. L., Walk, D., & Crosby, A. H. (2018). Truncating SLC5A7 mutations underlie a spectrum of dominant hereditary motor neuropathies. *Neurology: Genetics*, *4*(2), 222. https://doi.org/10.1212/NXG.0000000000000222

Sanes, J. R. (2003). The Basement Membrane/Basal Lamina of Skeletal Muscle. *Journal of Biological Chemistry*, *278*(15), 12601–12604. https://doi.org/10.1074/JBC.R200027200

Scremin, O. U., & Jenden, D. J. (1991). Time-Dependent changes in cerebral choline and acetylcholine induced by transient global ischemia in rats. *Stroke*, *22*(5), 643–647. https://doi.org/10.1161/01.STR.22.5.643

Shaw, G., Morse, S., Ararat, M., & Graham, F. L. (2002). Preferential transformation of human neuronal cells by human adenoviruses and the origin of HEK 293 cells. *The FASEB Journal*. https://doi.org/10.1096/fj.01-0995fje

Stehberger, P. A., Shmukler, B. E., Stuart-Tilley, A. K., Peters, L. L., Alper, S. L., & Wagner, C. A. (2007). Distal renal tubular acidosis in mice lacking the AE1 (band3) Cl-/HCO3-exchanger (slc4a1). *Journal of the American Society of Nephrology : JASN*, *18*(5), 1408–1418. https://doi.org/10.1681/ASN.2006101072

Stover, E. H., Akil, I., Al-Sabban, E. A., Baguley, D. M., Bianca, S., Bakkaloglu, A., Bircan, Z., Chauveau, D., Clermont, M. J., Guala, A., Hulton, S. A., Borthwick, K. J., Kroes, H., Li Volti, G., Mir, S., Mocan, H., Nayir, A., Ozen, S., Rodriguez Soriano, J., … Axon, P. R.

(2002a). Novel ATP6V1B1 and ATP6V0A4 mutations in autosomal recessive distal renal tubular acidosis with new evidence for hearing loss. *Journal of Medical Genetics*, *39*(11), 796–803. https://doi.org/10.1136/JMG.39.11.796

Stover, E. H., Akil, I., Al-Sabban, E. A., Baguley, D. M., Bianca, S., Bakkaloglu, A., Bircan, Z., Chauveau, D., Clermont, M. J., Guala, A., Hulton, S. A., Borthwick, K. J., Kroes, H., Li Volti, G., Mir, S., Mocan, H., Nayir, A., Ozen, S., Rodriguez Soriano, J., … Axon, P. R. (2002b). Novel ATP6V1B1 and ATP6V0A4 mutations in autosomal recessive distal renal tubular acidosis with new evidence for hearing loss. *Journal of Medical Genetics*, *39*(11), 796–803. https://doi.org/10.1136/JMG.39.11.796

Takashina, K., Bessho, T., Mori, R., Kawai, K., Eguchi, J., & Saito, K. I. (2008). MKC-231, a choline uptake enhancer: (3) Mode of action of MKC-231 in the enhancement of high-affinity choline uptake. *Journal of Neural Transmission*, *115*(7), 1037–1046. https://doi.org/10.1007/S00702-008-0049-0/TABLES/3

Takeshige, K., Baba, M., Tsuboi, S., Noda, T., & Ohsumi, Y. (1992). Autophagy in yeast demonstrated with proteinase-deficient mutants and conditions for its induction. *Journal of Cell Biology*, *119*(2), 301–312. https://doi.org/10.1083/jcb.119.2.301

Tan, N. B., Stapleton, R., Stark, Z., Delatycki, M. B., Yeung, A., Hunter, M. F., Amor, D. J., Brown, N. J., Stutterd, C. A., McGillivray, G., Yap, P., Regan, M., Chong, B., Fanjul Fernandez, M., Marum, J., Phelan, D., Pais, L. S., White, S. M., Lunke, S., & Tan, T. Y. (2020). Evaluating systematic reanalysis of clinical genomic data in rare disease from single center experience and literature review. *Molecular Genetics & Genomic Medicine*, *8*(11), e1508. https://doi.org/10.1002/MGG3.1508

Tsukada, M., & Ohsumi, Y. (1993). Isolation and characterization of autophagy-defective mutants of Saccharomyces cerevisiae. *FEBS Letters*, *333*(1–2), 169–174. https://doi.org/10.1016/0014-5793(93)80398-E

Van der Auwera, G. A., Carneiro, M. O., Hartl, C., Poplin, R., del Angel, G., Levy-Moonshine, A., Jordan, T., Shakir, K., Roazen, D., Thibault, J., Banks, E., Garimella, K. V., Altshuler, D., Gabriel, S., & DePristo, M. A. (2013). From FastQ data to high confidence variant calls: the Genome Analysis Toolkit best practices pipeline. *Current Protocols in Bioinformatics*, *43*(1110). https://doi.org/10.1002/0471250953.BI1110S43

Van Goor, F., Hadida, S., Grootenhuis, P. D., Burton, B., Stack, J. H., Straley, K. S., Decker, C. J., Miller, M., McCartney, J., Olson, E. R., Wine, J. J., Frizzell, R. A., Ashlock, M., & Negulescu, P. A. (2011). Correction of the F508del-CFTR protein processing defect in vitro by the investigational drug VX-809. *Proc Natl Acad Sci U S A*, *108*(46), 18843–18848. https://doi.org/10.1073/pnas.1105787108

Van Goor, F., Straley, K. S., Cao, D., González, J., Hadida, S., Hazlewood, A., Joubran, J., Knapp, T., Makings, L. R., Miller, M., Neuberger, T., Olson, E., Panchenko, V., Rader, J., Singh, A., Stack, J. H., Tung, R., Grootenhuis, P. D. J., & Negulescu, P. (2006). Rescue of ΔF508-CFTR trafficking and gating in human cystic fibrosis airway primary cultures by small molecules. *American Journal of Physiology-Lung Cellular and Molecular Physiology*, *290*(6), L1117–L1130. https://doi.org/10.1152/ajplung.00169.2005

Van Noorden, C. J. F., Boonacker, E., Bissell, E. R., Meijer, A. J., Van Marle, J., & Smith, R. E. (1997). Ala-Pro-cresyl violet, a synthetic fluorogenic substrate for the analysis of kinetic parameters of dipeptidyl peptidase IV (CD26) in individual living rat hepatocytes. *Analytical Biochemistry*, *252*(1), 71–77. https://doi.org/10.1006/ABIO.1997.2312

Varadi, M., Anyango, S., Deshpande, M., Nair, S., Natassia, C., Yordanova, G., Yuan, D., Stroe,

O., Wood, G., Laydon, A., Zídek, A., Green, T., Tunyasuvunakool, K., Petersen, S., Jumper, J., Clancy, E., Green, R., Vora, A., Lutfi, M., … Velankar, S. (2022). AlphaFold Protein Structure Database: massively expanding the structural coverage of protein-sequence space with high-accuracy models. *Nucleic Acids Research*, *50*(D1), D439–D444. https://doi.org/10.1093/NAR/GKAB1061

Walker MB (1934) - The James Lind Library The James Lind Library. (n.d.).

Wang, H., Salter, C. G., Refai, O., Hardy, H., Barwick, K. E. S., Akpulat, U., Kvarnung, M., Chioza, B. A., Harlalka, G., Taylan, F., Sejersen, T., Wright, J., Zimmerman, H. H., Karakaya, M., Stüve, B., Weis, J., Schara, U., Russell, M. A., Abdul-Rahman, O. A., … Crosby, A. H. (2017). Choline transporter mutations in severe congenital myasthenic syndrome disrupt transporter localization. *Brain : A Journal of Neurology*, *140*(11), 2838–2850. https://doi.org/10.1093/BRAIN/AWX249

White, K. A., Grillo-Hill, B. K., & Barber, D. L. (2017). Cancer cell behaviors mediated by dysregulated pH dynamics at a glance. *Journal of Cell Science*, *130*(4), 663. https://doi.org/10.1242/JCS.195297

Wrong, O., Bruce, L. J., Unwin, R. J., Toye, A. M., & Tanner, M. J. A. (2002). Band 3 mutations, distal renal tubular acidosis, and Southeast Asian ovalocytosis. *Kidney International*, *62*(1), 10–19. https://doi.org/10.1046/J.1523-1755.2002.00417.X

Xu, H., & Ren, D. (2015). Lysosomal physiology. *Annual Review of Physiology*, *77*, 57–80. https://doi.org/10.1146/annurev-physiol-021014-071649

Yamamoto1, A., Tagawa1, Y., Yoshimori2, T., Moriyama3, Y., Masaki1, R., & Tashiro1, Y. (1998). Bafilomycin Ai Prevents Maturation of Autophagic Vacuoles by Inhibiting Fusion between Autophagosomesand Lysosomesin Rat HepatomaCell Line, H-4-II-E Cells. In *CELL STRUCTURE AND FUNCTION* (Vol. 23).

Yaxley, J., & Pirrone, C. (2016a). Review of the Diagnostic Evaluation of Renal Tubular Acidosis. *The Ochsner Journal*, *16*(4), 525. /pmc/articles/PMC5158160/

Yaxley, J., & Pirrone, C. (2016b). Review of the Diagnostic Evaluation of Renal Tubular Acidosis. *The Ochsner Journal*, *16*(4), 525.

Yenchitsomanus, P.-T., Kittanakom, S., Rungroj, N., Cordat, E., & Reithmeier, R. A. F. (2005). Molecular mechanisms of autosomal dominant and recessive distal renal tubular acidosis caused by SLC4A1 (AE1) mutations. In *OPEN ACCESS Journal of Molecular and Genetic Medicine* (Vol. 1, Issue 2).

Yu, L., Chen, Y., & Tooze, S. A. (2018). Autophagy pathway: Cellular and molecular mechanisms. *Autophagy*, *14*(2), 207. https://doi.org/10.1080/15548627.2017.1378838

Zweyer, M. (2014). *Radiological Imaging of the Kidney*. https://link.springer.com/content/pdf/10.1007/978-3-642-54047-9.pdf

Appendix A

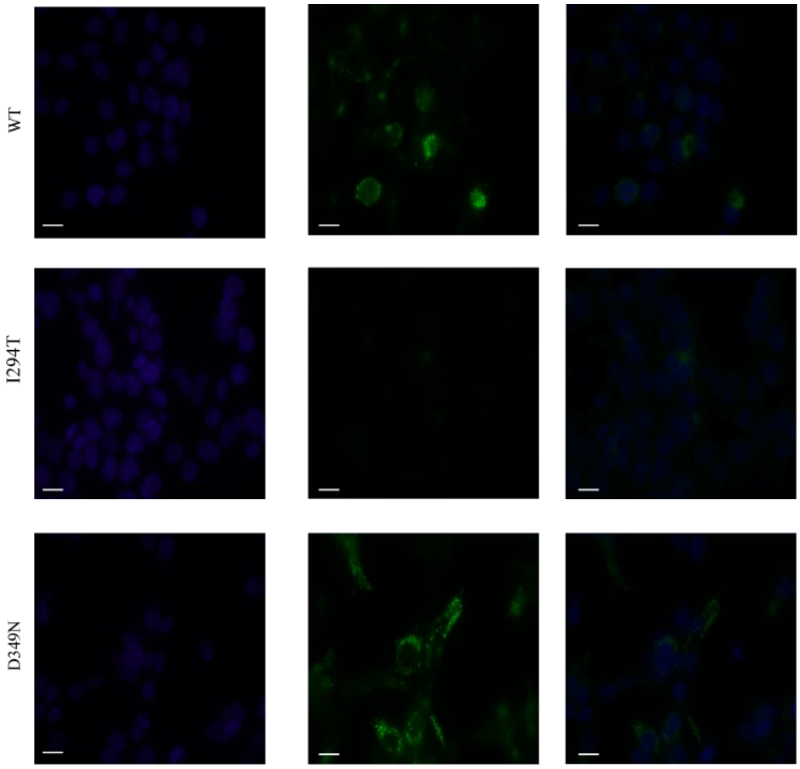

Figure 5.1. Fluorescence Images of HEK 293 stably expressing CHT1 WT, p.I294T and p.D349N. Image acquisition was done with an Olympus IX81 microscope equipped with a Nipkow spinning disk optimized by Quorum Technologies (Guelph, ON, Canada) and a 63X oil objective. Rb anti-CHT1 was used to detect CHT1 (green), DAPI was used to stain nuclei (blue) and the merged image is on the right. Scale bars correspond to 14 µm.

A

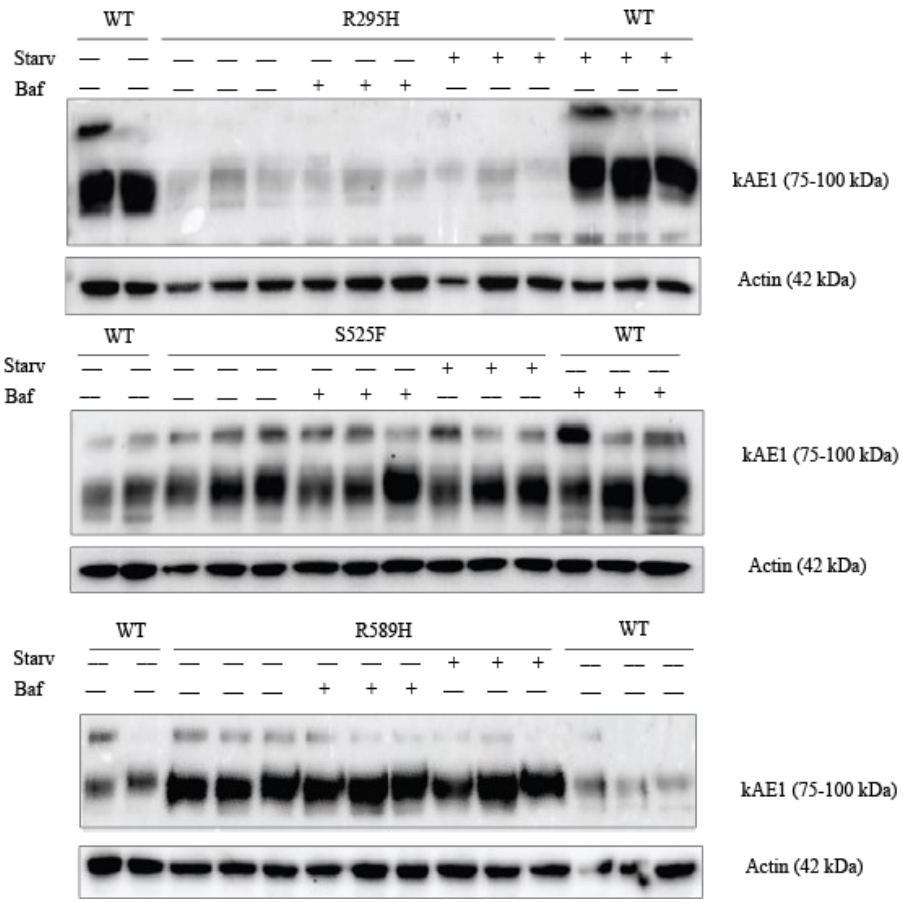
WT
R295H
WT
Starv
Baf
kAE1 (75-100 kDa)
Actin (42 kDa)
WT
S525F
WT
Starv
Baf
kAE1 (75-100 kDa)
Actin (42 kDa)
WT
R589H
WT
Starv
Baf
kAE1 (75-100 kDa)
Actin (42 kDa)

B

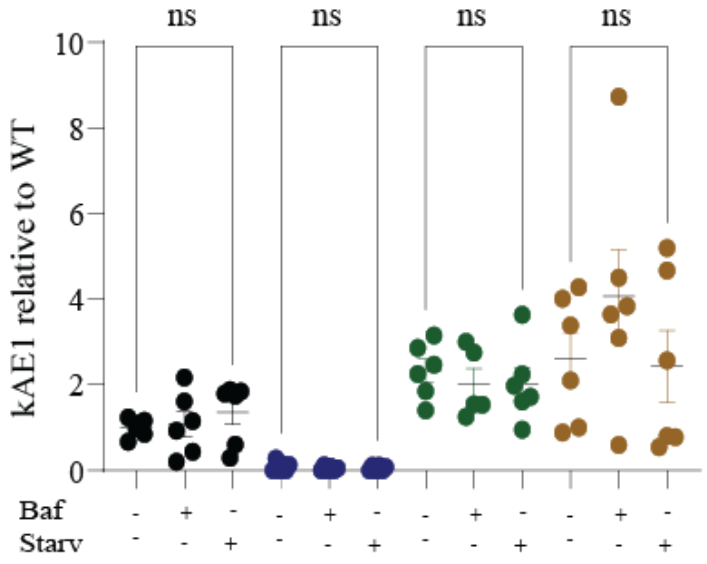
ns
ns
ns
ns
kAE1 relative to WT
10
8
6
4
2
0
Baf
Starv

Figure 5.1. Effect of starvation and bafilomycin A1 on kAE1 abundance in mIMCD WT, R295H, S525F and R589H kAE1-HA cells. **(A)** Immunoblot of mIMCD WT, R295H, S525F and R589H cells treated with doxycycline for 48hr. Cells were treated with 400 nM Bafilomycin A1 for the last 4hrs of the 48 hrs, or 2 hr incubation with HBSS or no treatment prior to lysis with RIPA buffer. Rat anti-HA was used to detect kAE1. **(B)** Graphical representation of blots shown in A. Error bars correspond to mean ± SEM, n= minimum 3. The treatments did not influence kAE1 expression in any of the cell lines.

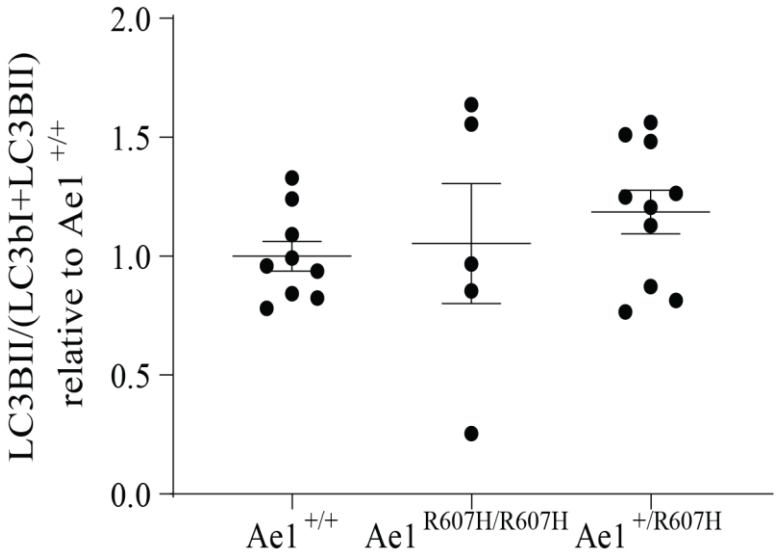

Figure 5.3. Total LC3B in $Ae1^{+/+}$, $Ae1^{R607H/R607H}$, and $Ae1^{+/R607H}$ kidney homegenates. Graphical representation of blot shown in **Figure 3.3 A**. Values were calculated by dividing the sum of the intensities of LC3BI and II by the intensity of the corresponding actin bands. Error bars correspond to mean ± SEM, n= minimum 5. *P<0.05, ****P < 0.0001 using one-way ANOVA with Dunett's multiple comparison post hoc test. Total LC3B is not different between $Ae1^{+/+}$, $Ae1^{R607H/R607H}$, and $Ae1^{+/R607H}$.